JANUARY 2007 VOLUME 78 NUMBER 1

REVIEW OF SCIENTIFIC INSTRUMENTS

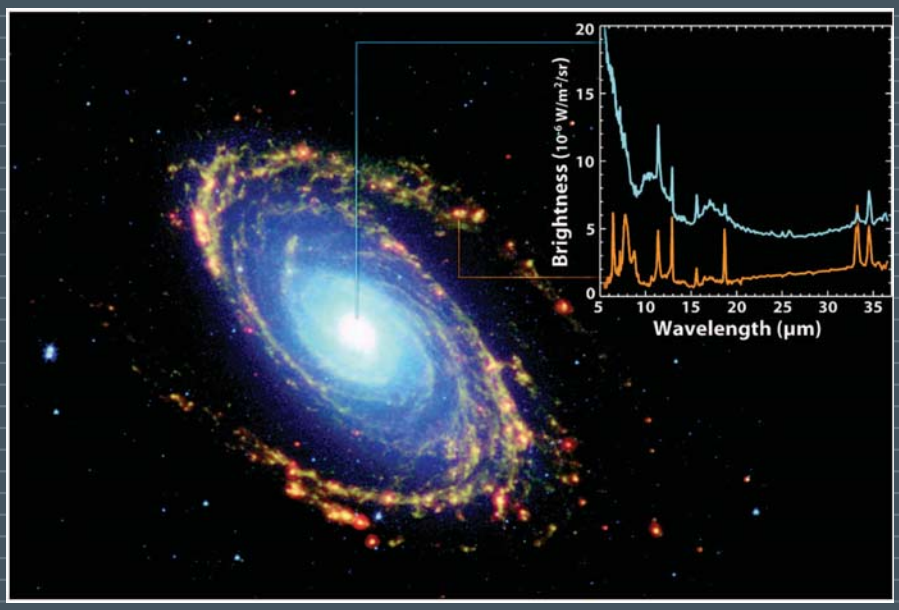

INVITED ARTICLE: The NASA Spitzer Space Telescope
by Gehrz et al.

0034-6748(200701)78:1;1-8

AMERICAN INSTITUTE OF PHYSICS

REVIEW ARTICLE

The NASA Spitzer Space Telescope

R. D. Gehrz[a)]
Department of Astronomy, School of Physics and Astronomy, 116 Church Street, S.E., University of Minnesota, Minneapolis, Minnesota 55455

T. L. Roellig[b)]
NASA Ames Research Center, MS 245-6, Moffett Field, California 94035-1000

M. W. Werner[c)]
Jet Propulsion Laboratory, California Institute of Technology, MS 264-767, 4800 Oak Grove Drive, Pasadena, California 91109

G. G. Fazio[d)]
Harvard-Smithsonian Center for Astrophysics, 60 Garden Street, Cambridge, Massachusetts 02138

J. R. Houck[e)]
Astronomy Department, Cornell University, Ithaca, New York 14853-6801

F. J. Low[f)]
Steward Observatory, University of Arizona, 933 North Cherry Avenue, Tucson, Arizona 85721

G. H. Rieke[g)]
Steward Observatory, University of Arizona, 933 North Cherry Avenue, Tucson, Arizona 85721

B. T. Soifer[h)] and D. A. Levine[i)]
Spitzer Science Center, MC 220-6, California Institute of Technology, 1200 East California Boulevard, Pasadena, California 91125

E. A. Romana[j)]
Jet Propulsion Laboratory, California Institute of Technology, MS 264-767, 4800 Oak Grove Drive, Pasadena, California 91109

(Received 2 June 2006; accepted 17 September 2006; published online 30 January 2007)

The National Aeronautics and Space Administration's Spitzer Space Telescope (formerly the Space Infrared Telescope Facility) is the fourth and final facility in the Great Observatories Program, joining Hubble Space Telescope (1990), the Compton Gamma-Ray Observatory (1991–2000), and the Chandra X-Ray Observatory (1999). Spitzer, with a sensitivity that is almost three orders of magnitude greater than that of any previous ground-based and space-based infrared observatory, is expected to revolutionize our understanding of the creation of the universe, the formation and evolution of primitive galaxies, the origin of stars and planets, and the chemical evolution of the universe. This review presents a brief overview of the scientific objectives and history of infrared astronomy. We discuss Spitzer's expected role in infrared astronomy for the new millennium. We describe pertinent details of the design, construction, launch, in-orbit checkout, and operations of the observatory and summarize some science highlights from the first two and a half years of Spitzer operations. More information about Spitzer can be found at http://spitzer.caltech.edu/. © *2007 American Institute of Physics.* [DOI: 10.1063/1.2431313]

I. INTRODUCTION

The National Aeronautics and Space Administration's (NASA's) Spitzer Space Telescope (Spitzer),[1,2] launched into an Earth-trailing orbit (Fig. 1) on 2003 August 25.23 UT, is an infrared observatory being used to study the creation of the universe, the formation and evolution of primitive galaxies, the genesis of stars and planets, and the chemical evolution of the universe. Spitzer's 85 cm cryogenically cooled beryllium Ritchey-Chretien telescope operates at temperatures as low as 5.5 K. The Cryogenic Telescope Assembly (CTA) houses the cryogenic telescope (CT), the liquid helium Dewar, and the science instruments (SIs). Spitzer's three cryogenically cooled SIs enable imaging and spectroscopy in the 3–180 μm wavelength range with their large-format detector arrays. Their observations are more sensitive than those obtained on any previous infrared mission.

[a)]Electronic mail: gehrz@astro.umn.edu
[b)]Electronic mail: thomas.l.roellig@nasa.gov
[c)]Electronic mail: mwerner@sirtfweb.jpl.nasa.gov
[d)]Electronic mail: gfazio@cfa.harvard.edu
[e)]Electronic mail: houck@astrosun.tn.cornell.edu
[f)]Electronic mail: flow@as.arizona.edu
[g)]Electronic mail: grieke@as.arizona.edu
[h)]Electronic mail: bts@irastro.caltech.edu
[j)]Present address: 615 Solway Street, Glendale, California 91206; retired; electronic mail: erom@earthlink.net

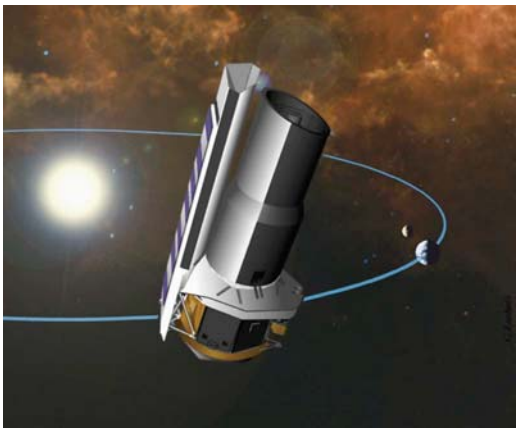

FIG. 1. A basic external view of Spitzer in its Earth-trailing solar orbit. The telescope cools by radiating to space and by the change in enthalpy of evaporating liquid helium while hiding from the Sun behind its solar panel and flying away from the thermal emission of the Earth. Courtesy of NASA/JPL-Caltech.

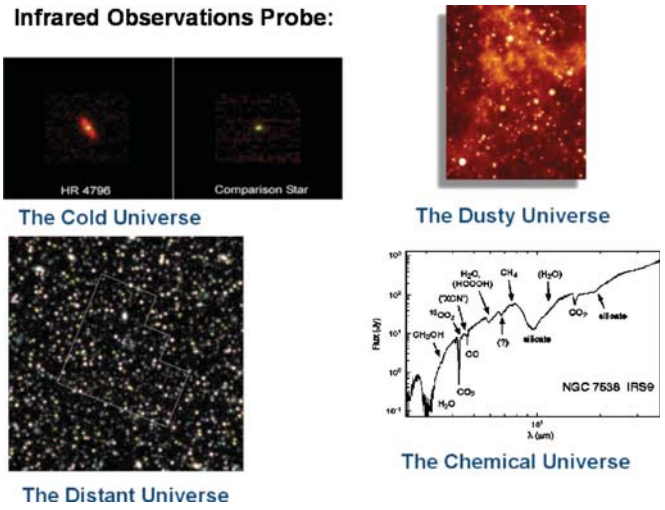

FIG. 3. The observational objectives of infrared astronomy: Studies of the cold, dusty, distant, and chemical universes are described in detail in Sec. I A. Courtesy of NASA/JPL-Caltech.

A. Infrared astronomy overview

Although modern astrophysics uses observations across the electromagnetic spectrum in pursuit of its scientific objectives, each spectral band provides unique perspectives on the universe. Infrared astronomy is defined by the temperature range of objects that emit most strongly at wavelengths of 1–1000 μm (see Fig. 2). Infrared observations permit the following types of studies (Fig. 3).

(1) *The cold universe*. Infrared observations are uniquely sensitive to objects at temperatures between ~3000 and ~3 K. This spans the range between the coolest stars and the coldest interstellar matter. Circumstellar and interstellar matter, planets and solar system dust and debris, and substellar objects or brown dwarfs are best, and in some cases, uniquely studied in the infrared.

(2) *The dusty universe*. Interstellar dust is composed of submicrometer-sized mineral, organic, and icy particles. Dust and dust clouds are ubiquitous throughout the universe and are frequently thick enough to obscure embedded or background objects at visible and ultraviolet wavelengths. However, dust clouds that are totally opaque at visible wavelengths can be quite transparent to the longer infrared wavelengths. Thus the center of our Milky Way galaxy, hidden in the visible behind the dusty material lying in the galactic plane, was discovered and studied in detail in the infrared. Additionally, dust in all astrophysical environments efficiently absorbs optical and ultraviolet radiations, reradiating the energy in the infrared. As a result, at the present epoch the energy density of infrared radiation in the universe is as large as that of optical and ultraviolet radiations,[3] and there are known objects that radiate 98% or more of their total power in the infrared due to this reradiation process.

(3) *The distant universe*. The expansion of the universe shifts radiation towards the infrared by a factor $1+z$, where z is the redshift of the target in question. Now, redshifts greater than five are very commonly explored; galaxies at this redshift are seen as they were when the universe was less than 1.2 Gyr old, as opposed to its current age of ~13.7 Gyr in standard cosmological models, so the light we see has been traveling for ~12.5 Gyr. For this redshift, radiation that left the galaxy in the ultraviolet is seen at infrared wavelengths; therefore, infrared observations provide a natural means of studying distant objects and probing the early evolution of the universe.

(4) *The chemical universe*. The infrared contains diagnostic spectral features of atoms, ions, molecules, and solid materials sampling a very wide range of astrophysical environments. These range from fine-structure lines of species as highly ionized as Ne^{+5} to absorption bands of CO and CO_2 ices that arise only in the coldest interstellar clouds.

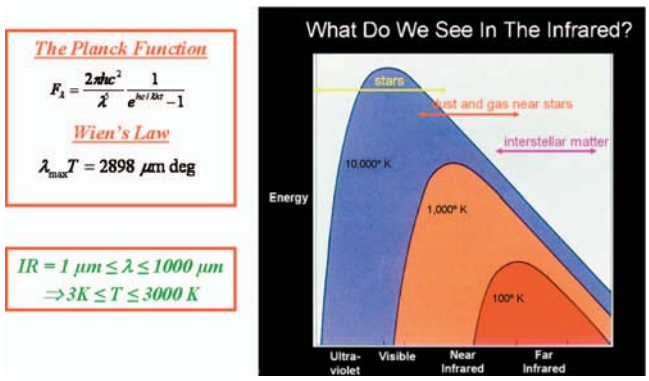

FIG. 2. (Color) The Planck function and infrared astronomy: The energy distribution F_λ as a function of wavelength λ of a blackbody of temperature T is given by the Planck distribution, the peak of which is given by Wien's law. Infrared astronomy, generally defined as covering wavelengths between 1 and 1000 μm, enables studies of cool stars, circumstellar gas and dust, and interstellar matter.

These and other features of the infrared for astronomical exploration have given rise to vigorous programs of ground-based infrared astronomy using both general purpose telescopes such as the 5 m Hale telescope at Palomar Mountain

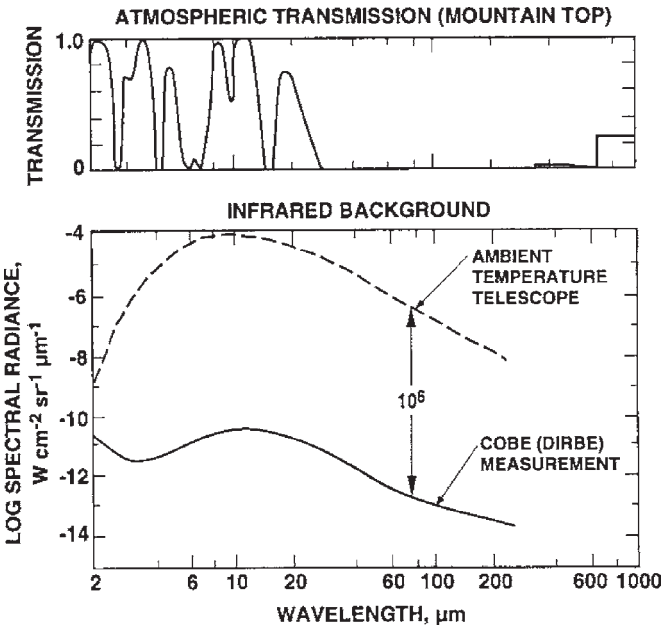

FIG. 4. The rationale for going into space to do infrared astronomy: The upper panel shows the transmission of the atmosphere from Mauna Kea, Hawaii (13 796 ft above sea level). Most of the infrared wavelengths are still blocked by residual water vapor, ozone, and carbon dioxide. The latter two still block infrared light at balloon altitudes. The lower panel shows the reduction in background heat obtained by cooling the telescope to 5.5 K where thermal emission from the zodiacal cloud and galactic dust clouds dominate. Courtesy of NASA/JPL-Caltech.

and infrared-optimized telescopes such as those at the Gemini observatories in Hawaii and Chile. However, achieving the true potential of the infrared requires the use of facilities in space.

B. Spitzer science objectives

As is evident from Fig. 4, the impetus for conducting infrared astronomy from space comes from the dual need to (1) observe wavelengths that are blocked by the atmosphere, and (2) cool the telescope to lower the ambient background by a factor of 10^6, thereby raising the nominal sensitivity by a factor of 10^3, since the shot noise is proportional to the square root of the background power. The Spitzer mission design was driven by the infrared requirements of four major scientific programs in The Bahcall Report.[4] These are (1) studies of protoplanetary and planetary debris disks, (2) surveys to discover brown dwarfs and super planets, (3) elucidation of the properties of ultraluminous infrared galaxies and active galactic nuclei (AGNs), and (4) surveys to detect objects representative of the earliest epochs of the formation of the universe. The resulting system has very powerful capabilities in many other scientific areas and has great potential for the discovery of new phenomena in the universe. Thus, Spitzer is an observatory for the entire scientific community.

II. PROJECT HISTORY

Werner[5] and Rieke[6] have described the history of the Spitzer Space Telescope in detail. The facility was first proposed in 1969 as a space-shuttle-attached payload with a 1-m class cryogenic telescope, eventually called the Shuttle Infrared Telescope Facility (SIRTF). It was thought that there could be frequent flight opportunities for missions lasting up to a month, with a first launch in 1979, and at a cost of about $120M. Subsequently, the success of the Infrared Astronomical Satellite (IRAS) as a free-flying observatory, scrutiny of the potential science returns of a shuttle-attached SIRTF mission, concern about the contamination levels of the space shuttle environment, and the high cost of shuttle launches all dictated that SIRTF become free-flying. At this point, "SIRTF" became an acronym for "Space Infrared Telescope Facility." It assumed various forms, using first a Space-Shuttle-accessible low-Earth orbit (LEO), and then a Titan launch into a high-Earth orbit (HEO), ballooning in the process to become a 5700 kg payload carrying 3800 L of liquid

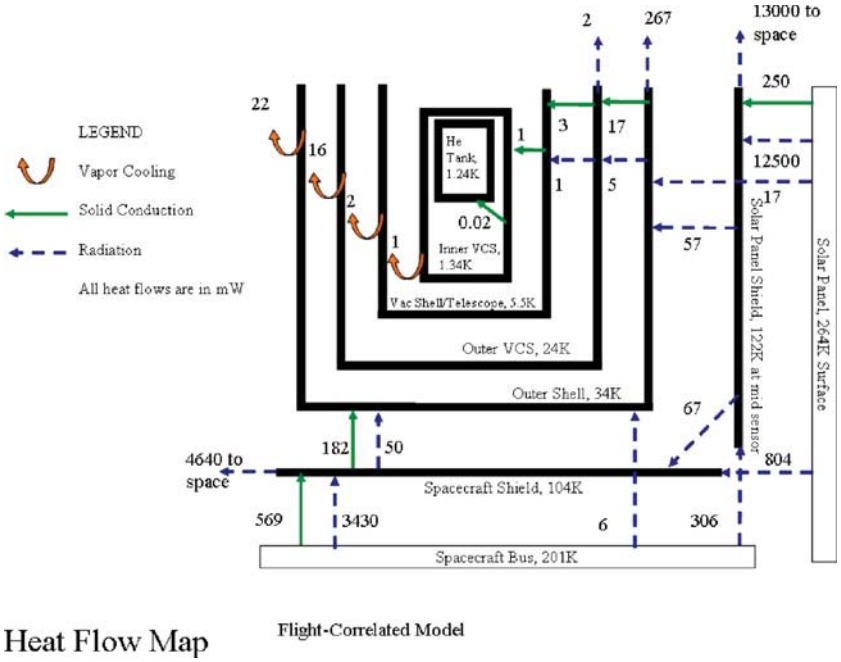

FIG. 5. Ball Aerospace thermal model. Heat input is solely from insolation on the solar panel. Cooling of the cryogenic telescope assembly is accomplished by radiation and vapor cooling. Heat is transferred through the system along the paths indicated by the arrows by radiation (dashed blue arrows), conduction (solid green arrows), and vapor cooling (broad orange arrows). The equilibrium temperatures for the various observatory components are given for the case when the cryogenic telescope is operating at 5.5 K. The model assumes a focal-plane heat dissipation of 4 mW and an insolation of 5.3 kW. Courtesy of Ball Aerospace/JPL-Caltech.

Heat Flow Map Flight-Correlated Model

helium and costing over $2B. Rapid cost growth in a number of approved missions combined with a weakening economy and a number of space flight failures caused the Congress to cancel this mission in 1991. SIRTF was revived through the strong commitment of NASA, combined with the idea of Jet Propulsion Laboratory (JPL) Mission Engineer Kwok to launch it into a 1 AU orbit around the Sun, trailing the Earth, to allow the use of a smaller rocket and to obtain a benign thermal environment for the observatory. A mission concept taking advantage of these ideas was still not cheap enough given the declining funding for space science in the early 1990s. Eventually, the Spitzer project succeeded by adopting five key concepts to constrain the design of the mission and control its cost.

(1) The observatory would fly in an Earth-trailing orbit.
(2) The telescope would be launched warm and cooled down on orbit.
(3) All instruments would be designed according to a "bolt and go" concept where in-orbit adjustments were not allowed.
(4) As many moving parts as possible would be eliminated.
(5) Only one SI could operate at any time.

A. Gaining control of costs: Launching warm into a solar orbit

Influenced by the precepts of "faster-better-cheaper," NASA management had also challenged the SIRTF Science Working Group (SWG) and the JPL engineering team to fit the mission within a number of additional requirements: (a) no cost growth and a rapid development cycle, (b) a 2.5 year minimum lifetime, (c) an 85 cm diameter telescope, and (d) launch on a Delta-2 rocket. Meeting this combination of requirements would have been impossible with earlier mission concepts. However, SWG member Low suggested that the payload could be reconfigured so the telescope would cool by radiation to space after it was launched, taking full advantage of Kwok's proposal for an Earth-trailing orbit to get far away from the heat of the Earth. This configuration, eventually implemented by Finley *et al.*,[7] resulted in a substantial reduction of mass and size at launch, critical for use of the Delta rocket. The implementation was based on novel ways to reject waste heat from the Sun, to maximize the radiative cooling to outer space, and most important, to harvest the cooling power of the supercool helium vapor as it vented to space. Kwok's orbit was based on the realization that the least energy required to get far from the Earth would be to give the observatory the minimum escape velocity from the Earth, so it would be boosted gently into a Solar, Earth-trailing orbit (Fig. 1). Although separation from the Earth/Moon system would occur quickly, their gravity would slow the spacecraft so it would thereafter remain close enough to send the data back efficiently to the deep space network (DSN). Observing conditions are nearly perfect in this special orbit, with the only exception being vulnerability to occasional solar storms. The idea of cooling after launch in an environment far from the Earth, which we term the "warm-launch" concept, provided a paradigm for lower-cost infrared

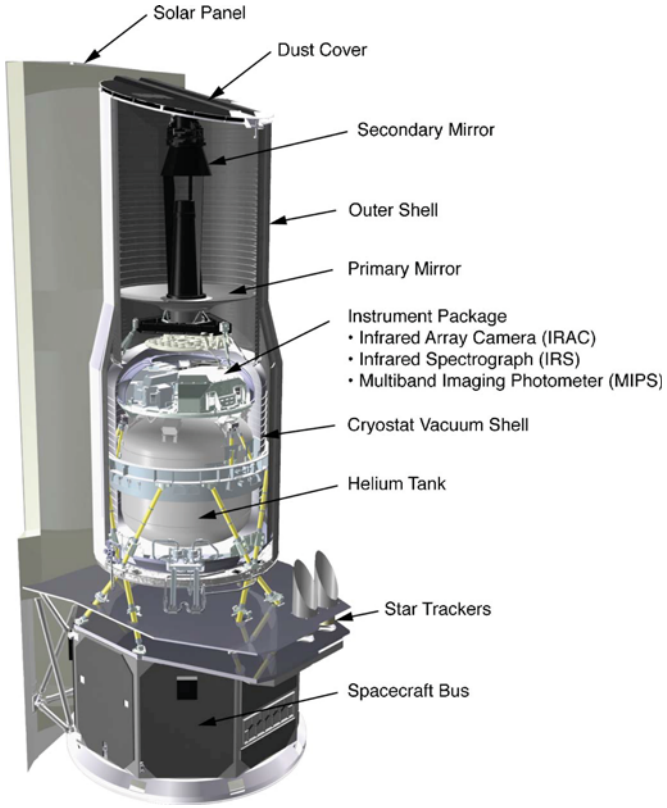

FIG. 6. Cutaway view of the cryogenic telescope assembly showing the details of its mounting to the spacecraft bus (SCB) and internal details of the structure. Kinematic, conductive isolation from the SCB is accomplished using gamma-alumina bipod struts (yellow). The titanium bipod flexures that attach the cryogenic telescope bulkhead to the cryostat and the primary mirror to the bulkhead are clearly visible in this view, as is the attachment point of the metering tower adapter ring to the bulkhead. Courtesy of Ball Aerospace.

missions that has now been widely adopted. There are a number of important design features that determine how the Spitzer cooling system works. The most important of these are as follows.

(1) The telescope is made of beryllium and cools more than 20 times faster than a glass telescope.
(2) Vapor cooling by the enthalpy of a superfluid helium cryostat yields a significant amount of cooling power. Since the densities of gaseous and liquid helium near the liquid boiling point are very similar, the latent heat of vaporization is relatively low. However, this yields a large change in enthalpy with temperature as the helium gas warms and expands. Thus, as helium vapor goes through heat exchangers and finally flows out of the vent into space at about 34 K, it will have provided the telescope considerably more cooling energy than the original vaporization of the same mass of liquid helium.
(3) The design of the solar shield assembly is critical because kilowatts of power are incident on the Sunward side of the shield. Through careful design and construction, the incident solar power impinging on the observatory is either reflected or reradiated so that the inward heat flow is reduced by a factor of 10,000 before it reaches the outer shell (OS) (Fig. 5).
(4) The OS functions as a light-tight enclosure. The back

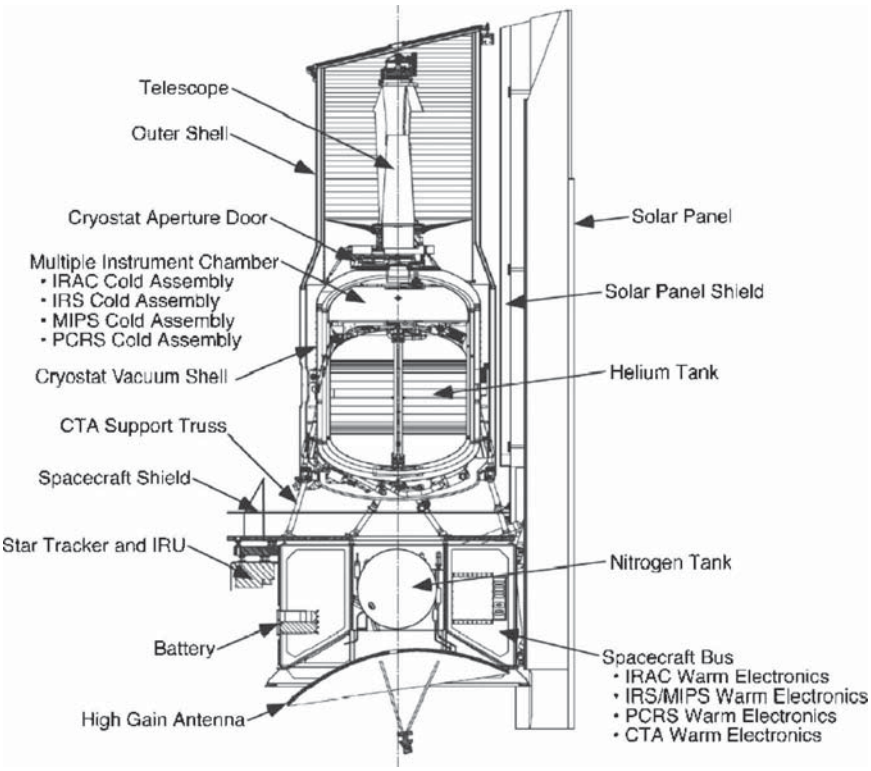

FIG. 7. Side elevation of the launch configuration of Spitzer observatory, which measures approximately 4.5 m in height and 2.1 m in diameter. The facility was launched on 2003 August 25.23 UT, the dust cover was ejected on 2003 August 30.11 UT, and the cryostat aperture door was retracted on 2003 August 31.06 UT. Reproduced by permission of Werner *et al.* (Ref. 2).

side functions as a nearly perfect blackbody radiator to space. The front side is a reflector that rejects photons efficiently.

(5) The OS also serves as a highly conductive vapor-cooled shield that is equipped with a well designed heat exchanger. Inside the OS, two additional vapor-cooled low-emissivity shields further intercept most of the remaining heat flowing inward. The helium vapor exits the vent tube at about 34 K and the vent tube itself is designed so that the escaping vapor imparts very low torques to the observatory. Each assembly cooled by vapor exchange is strongly thermally connected to the heat exchangers through direct mechanical coupling. The heat exchangers are matched to the predicted thermal loads. The vent-tube design utilizes thin-wall stainless steel tubing to connect heat exchanger assemblies to minimize conduction losses along the vent line. The vent line within the heat exchangers is high-thermal-conductivity aluminum tubing.

(6) The telescope structure is attached to the outer shell of the cryostat pressure vessel that contains the three SIs, the pointing calibration and reference sensor (PCRS)[8] described below, and the 360 L helium tank. In space, the sealed and suspended structures have a different thermal function than they did on the ground and during cooldown. An automated aperture door mechanism (ADM) is opened on orbit in the vacuum of space after the observatory has outgassed so light can reach the instruments (Fig. 6).

(7) Heaters maintain the instruments and the various detectors therein at their own operating temperatures. Only one instrument is powered up at any time. Normally the cold instrument power dissipation is less than 4 mW. A separate heater in the helium tank (called the "makeup heater") can be activated to boil off helium at a faster rate, thereby increasing the vapor cooling power and lowering the telescope temperature for far-infrared observations. The nominal helium bath temperature is 1.2 K.

(8) The observatory's cold lifetime, which is discussed in Sec. VI A, is determined by the initial mass of the helium bath on orbit and the power dissipation of the SIs and the makeup heater.

The above innovations reduced the complexity of the

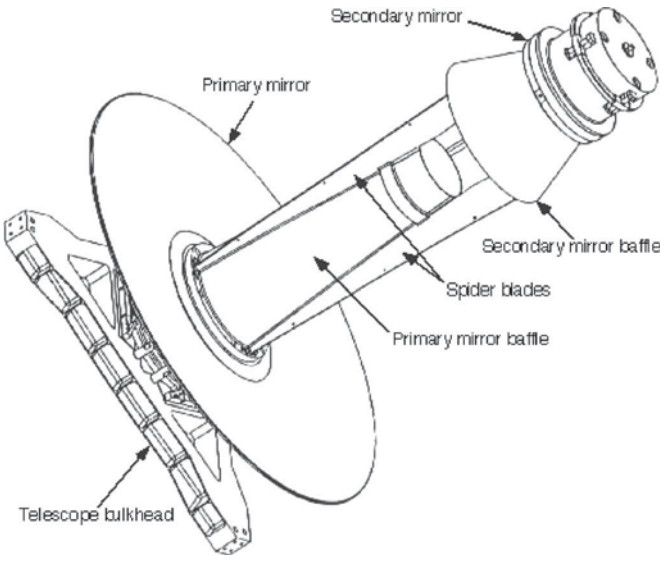

FIG. 8. Assembly drawing of the cryogenic telescope. The bulkhead and all of the telescope components except for the three titanium bipod flexures that mount the primary mirror to the bulkhead are made of hot isostatically pressed beryllium. Courtesy of NASA/JPL-Caltech.

facility, increased the reliability of the instruments, and lowered the observatory mass to 850 kg and the helium load to 360 L with an even longer mission lifetime than the original configuration would have had. In recognition of the improvement that these innovations had on the Spitzer mission, Aviation Week and Space Technology cited the Spitzer team with a 2003 "Space Laurel Award" for "redesigning Spitzer [… as a warm-launched, radiatively cooled telescope (our paraphrasing)…], which saved $800M…."[9] Overall, during this development history, significant gains were accomplished by eliminating the Earth as a source of thermal background, allowing for a spacecraft orientation that would provide for a significant amount of cooling of the CTA by radiation to outer space, eliminating the thermal stresses associated with the day-night effects of circulating in LEO, and flying away from the effects of the Earth's radiation belts.

B. Cost control and reliability

Costs were further contained by eliminating all but the most essential moving parts. Advances in the development of large-format infrared detector arrays allowed for the replacement of motor-driven filter wheels with dichroics and modules that fed a larger number of arrays. The SI development teams and other SWG members were selected by NASA in June of 1984. The contractor teams were selected in 1996 and the facility launched in August of 2003. Upon successful completion of its in-orbit checkout (IOC) and a period of early-release scientific observations, SIRTF was renamed "Spitzer" in honor of the late Dr. Lyman Spitzer Jr. (1914–1997), a Princeton University professor.[10] In 1946, Spitzer was the first to propose placing a large telescope in space to eliminate the effects of atmospheric "seeing" that blurs images produced by ground-based telescopes.

III. FLIGHT COMPONENTS

Figure 1 shows a basic external view of Spitzer in its Earth-trailing solar orbit described in Sec. VII A and VII B. Figures 6–8 show the observatory subsystems: the CTA, the spacecraft bus (SCB), and the solar panel and solar panel group. The CTA (Fig. 6) contains four subassemblies: the CT (Fig. 8), the superfluid helium cryostat, the multiple instrument chamber (MIC) (Fig. 9) housing the SIs, and the thermal control OS. The SCB contains the subsystems required for housekeeping and control engineering: telecommunications, reaction control, pointing control, command and data handling (C&DH), and power.

The Spitzer SCB was built by Lockheed Martin Missiles and Space (LMMS). The CTA was built by Ball Aerospace Technologies Corporation (BATC). Integration and testing of the completed observatory took place at LMMS. The two components are thermally isolated from each other with a system of low-thermal-conductivity struts and shields. The overall layout of the flight configuration is shown in Fig. 7, while summary information about the complete flight system is given in Table I and Fig. 10. More detailed descriptions of the two components are given below.

FIG. 9. (Color) The Spitzer family portrait: the science instruments mounted on the multiple instrument chamber baseplate at Ball Aerospace during cryogenic telescope assembly integration and testing. Clockwise from from the lower right are IRAC (in black), MIPS, IRS long-low, IRS long-high, IRS short-low, and IRS short-high. Courtesy of NASA/JPL-Caltech.

A. Spacecraft bus

The Spitzer SCB handles the observatory's power generation, pointing and momentum control, data processing and storage, and telecommunications functions. It also contains the warm electronics portions of the three scientific instruments. The spacecraft avionics are fully redundant, as are the components of the pointing control system (PCS) and reaction control system (RCS) discussed below. As of this writing, the prime systems are still in use, so the redundancy has been preserved. A side elevation of Spitzer in its launch configuration is shown in Fig. 7.[2]

TABLE I. Top-level observatory parameters.

Parameter	Value
Total observatory mass at launch	861 kg
Dimensions (height × diameter)	4.5×21 m^2
Average operating power	375 W
Solar array generating capacity at launch	500 W
Nitrogen reaction control gas at launch	15.59 kg
Estimated reaction control gas lifetime	17 years
Mass memory capacity	2 Gbytes
Telescope primary diameter	0.85 m
Telescope operating temperature[a]	5.6–13 K
Superfluid helium at launch	337 L
Estimated nominal cryogenic lifetime	5.6–6.0 years
As-commanded pointing accuracy (1σ radial)	$<0.5''$
Pointing stability (1σ, 600 s)	$\leqslant 0.03''$
Maximum tracking rate	$1.0''$/s
Time to slew over ~90°	~8 min
Data transmission rate (high-gain antenna up to 0.58 AU from the Earth)	2.2 megabytes s^{-1}
Command communication rate	2 kilobytes/s

[a]Depending on instrument in use.

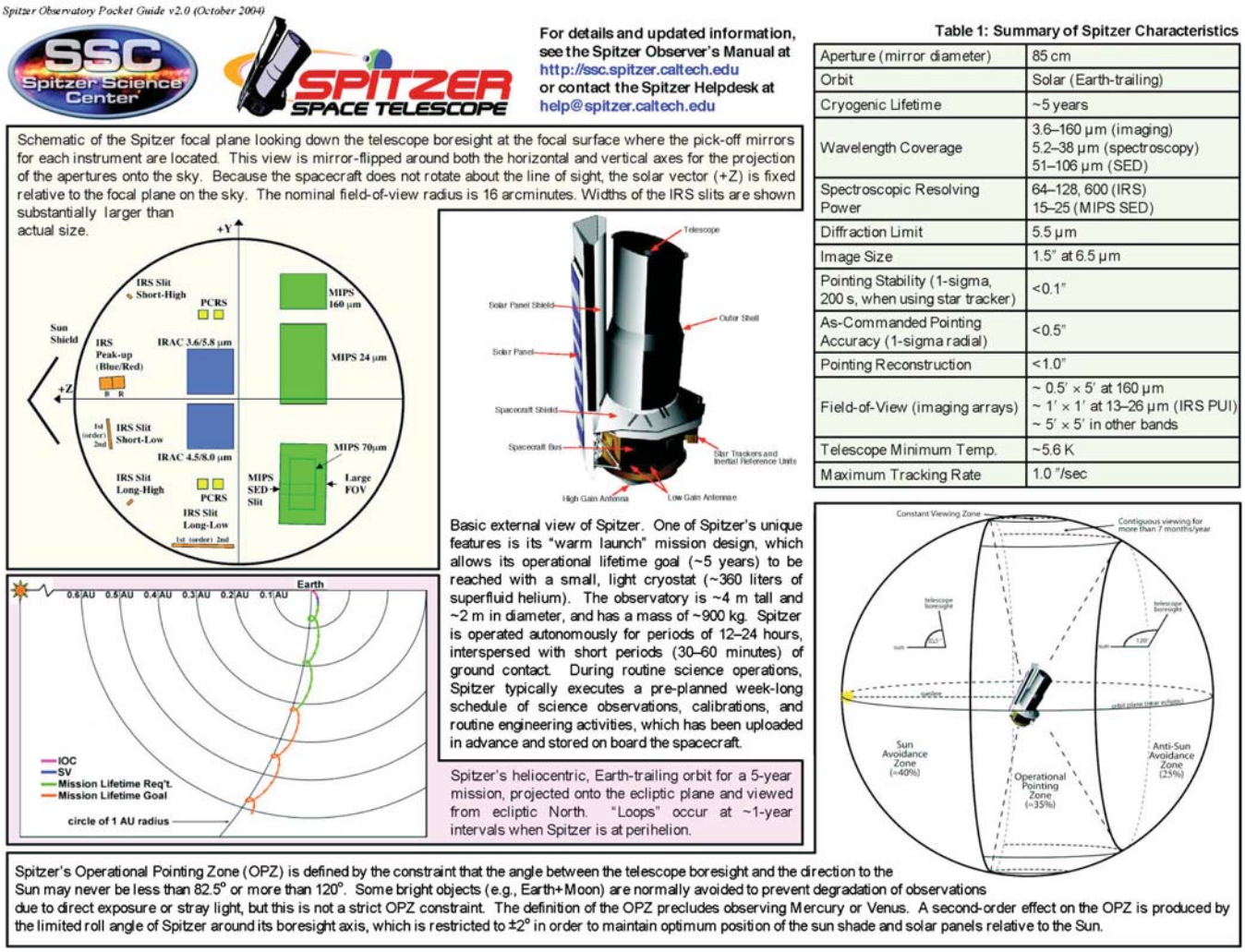

FIG. 10. The Spitzer Pocket Guide, which gives details about the basic Spitzer facility parameters, orbit and operational viewing zone, and focal plane orientation, can be downloaded by interested observers from the Spitzer internet website at http://ssc.spitzer.caltech.edu/documents/Spitzer_PocketGuide.pdf

1. Structure and configuration

The Spitzer warm SCB structure is octagonally shaped, constructed of graphite composite and aluminum honeycomb material, and mounted to the cold CTA with low-thermal-conductivity gamma-alumina struts. Aluminized Mylar thermal blankets and aluminum/graphite epoxy honeycomb radiation shields dramatically reduce the radiative thermal load onto the CTA from the warm SCB. A similar system of thermal shields attenuates the thermal radiation from the solar array, which is cantilevered from the SCB structure.

2. Pointing and reaction control system

Spitzer's pointing and tracking is accomplished using the PCS, which consists of reaction wheels, gyroscopes, star trackers, and the pointing calibration and reference sensor PCRS[8,19] focal plane star sensor. A nitrogen gas RCS is used to dump accumulated angular momentum that builds up over time as a result of solar wind and radiation pressure and the helium vapor venting torques.

In the PCS, the four reaction wheels mounted in a pyramid arrangement provide redundancy against a single wheel failure. The PCS has dual gyroscope packages and star trackers, and the PCRS has two redundant sides. Due to their relatively high operating temperature requirements, the star trackers and gyroscopes were mounted to the SCB instead of to the CTA structure. Light baffles cut in a sugar-scoop shape eliminate radiation from the warm star tracker optics and electronics onto the much colder CTA OS. These baffles are especially important because the star trackers are mounted facing the black painted side of the OS. The star trackers typically observe 40 stars down to ninth magnitude within their field of view and compare the observed field with an internal catalog of 87 000 Tycho stars[12] to determine Spitzer's absolute orientation in space.

The PCRS employs visible-wavelength Si p-i-n diode array detectors and is used for two functions.[8,13] Since the star trackers are not mounted directly to the telescope OS, any temperature variations in the metering path can translate into changes in the bore-sight alignment between the telescope and star tracker axes. The alignment between the gyros and star trackers does not vary because the gyro packages are mounted right next to the star trackers. The PCRS is used twice a day to track and calibrate the alignment drifts in the telescope and star tracker gyro axes. In addition, the PCRS can be used to fine-tune the pointing based on a small offset slew from a known standard star, which allows very accurate

positioning of the infrared spectrograph (IRS) instrument slits. The IRS has its own peak-up camera that can also be used in a similar way at infrared wavelengths.

Two wide-angle Sun sensors are mounted on the top and bottom of the Sun shield. These sensors are used in the observatory fault protection system to ensure that the Sun-avoidance angles are not violated and that direct sunlight never impinges on the cold surfaces of the CTA.

Changes in Spitzer's pointing orientation are made with the reaction wheels operating in a closed control loop with the gyroscopes and star trackers. A Kalman filter weights the gyro and star tracker feedback so that the gyros are primarily in control during a slew. The star tracker holds the pointing in a fixed inertial direction after completion of the slew. The pointing accuracy after completion of a slew is accurate to better than $0.5''$ (1σ rms radial) after a slew of any length, and is accurate to better than $0.4''$ for relative offsets of up to $30'$. Once the slew is complete, the pointing jitter is less than $0.03''$ (1σ radial) rms over a time period of 600 s.

Because the spacecraft is well outside the Earth's magnetic field, magnetic torquer bars cannot be used. Instead, any accumulated angular momentum is removed through the ambient-temperature pressurized gas RCS, which utilizes nitrogen so that the gas plume will not affect the infrared environment and the sensitive CTA thermal control surfaces. Aside from the tank holding the pressurized nitrogen, this system is completely redundant. Based on the present rate of use, the nitrogen gas is expected to last until at least 2014 before exhaustion.

3. Thermal control system

The nature of the Spitzer mission places a few unusual requirements on other spacecraft subsystems as well. For example, the thermal subsystem includes several features that minimize the thermal-mechanical drift between the cold telescope and warm star tracker lines of sight, including a gas-filled conductive heat pipe embedded in the top panel of the SCB to minimize temperature gradients between the SCB and the CTA struts. The Spitzer orbital thermal environment is relatively benign, with the Sun always shining on one side of the observatory and without the eclipses seen in low-inclination LEO. Within the SCB, heaters keep the electronic assemblies within their operating temperature ranges.

4. Telecommunications system and ground downlinks

The Spitzer observatory communicates with NASA's DSN over *X* band, transmitting at 8413.641 975 MHz and receiving at 7161.156 636 MHz. A Motorola New-Millennium-design small deep-space transponder feeds a pair of solid-state radio frequency (rf) amplifiers with a total power output of 29 W into a parabolic high-gain antenna. This system can provide downlink communication at up to 2.2 Mbytes/s, depending on the size of the DSN receiving dishes that are available and the distance of the spacecraft from the Earth. A pair of low-gain antennas provides nearly omnidirectional telecommunications capability for safe-mode recovery at much lower data rates. The Spitzer telecommunications system is fully redundant, with the exception of the parabolic high-gain antenna, with the rf power routed by a set of waveguide switches. The onboard Spitzer data storage allows periods between communication downlinks of one-half to two days, depending on the instrument in use. In between downlinks, the science and engineering data are stored in the onboard C&DH subsystem. The Spitzer mass memory can store more than 48 h of observations by the highest data rate instrument, the multiband imaging photometer for Spitzer (MIPS), which provides some resilience against a missed pass. The DSN stations at Goldstone, Madrid, and Canberra are the standard receiving locations, with either the 34 or 70 m dishes used for contacting the spacecraft. A typical downlink lasts less than 1 h.

5. Command and data handling

The onboard C&DH system is responsible for receiving and interpreting commands, executing stored command sequences, collecting engineering and science data, compressing data, and formatting telemetry packets. It is also responsible for fault detection and protection, as discussed in Sec. III A. The main hardware components consist of 13 electronics cards housed in a single housing: two RAD6000 single-board computers, two solid-state mass memory cards with a storage capability of 8 Gbits each, two payload and PCS interface cards, two fast uplink/downlink cards, two fast input/output cards; one shared C&DH module interface card, and two ac/dc converter power cards. The RAD6000 flight processor operates at 20 MHz and has 128 Mbytes of dynamic random access memory on its board. The pairs of boards mean that the C&DH system is mostly two-string redundant, although the mass memory cards are shared by both strings, as is the C&DH module interface card, which contains important configuration information needed in the case of a C&DH side swap. The Spitzer flight software is written in the C language and contains approximately 125 000 lines of code. The C&DH flight processors use the VxWorks real-time operating system, which provides the ability to handle multiple virtual software machines and also handles the various timing requirements and adjudicates among any software priority conflicts.

6. Fault protection and safe mode

Because of its distance from the Earth and infrequent telemetry contacts, Spitzer is designed to operate autonomously. Updating and maintaining pointing system parameters such as gyro scale factors or the alignment of the warm and cold frames is carried out autonomously, although the (now infrequent) engineering measurements that provide the data are scheduled in conjunction with the science measurements. The autonomous operations put particular demands on the fault protection system because the spacecraft has to guarantee the health and safety of the observatory. When onboard sensors command the observatory into safe mode, it autonomously orients itself with the solar array perpendicular to the Sun line and rotates slowly around this line with a period of 2 h. This maintains the thermal integrity of the observatory. The two low-gain antennas are mounted 180° apart on the circumference of the spacecraft, ±90° from the solar panel. This geometry assures that the beam of each of the low-gain antennas will sweep across the Earth for about

30 min during the 2 h rotation period. The low-gain antennas transmit a stream of engineering data at a reduced data rate of 44 bytes/s which provides adequate information to permit the operations teams to diagnose the fault that triggered the safe-mode entry and respond accordingly. Spitzer has experienced only a handful of safe-mode events, and the rapid recovery from each of these events validates this overall strategy.

B. Cryogenic telescope assembly

1. Warm-launch CTA and the cryogenic system

Spitzer's unique "warm-launch" mission design enables its operational lifetime goal of five years to be attained with a small, light cryostat that carries only 360 L of superfluid helium. In the warm launch concept, the telescope is attached externally to the heavy Dewar vacuum vessel (see Figs. 6 and 7), allowing for a substantially smaller, lower-weight payload than would be the case for a telescope launched cold. The hermetically sealed ADM, located on the vacuum vessel surface, was opened only after launch, allowing the light from the telescope to travel directly to the science instruments. During integration and testing, the ADM was kept closed, even in the thermal vacuum test chamber, to prevent contaminants from condensing on the cold optical surfaces of the SIs due to the test chamber's extreme temperature gradients. To mitigate parasitic heat loads during prelaunch testing and ground hold, the ADM window was coated with a thin layer of gold to reflect radiation beyond about 5.3 μm. As a result, only the infrared array camera (IRAC) channels 1–3 and the IRS short-low modes could be used for CTA image performance evaluation during the BRUTUS Test (see Sec. III B 3 for a description of the BRUTUS test).

Virtually all of the solar heat received by the observatory is rejected to space through high-thermal-emissivity black surfaces using a special black paint carefully developed and qualified by BATC. A thermally conductive heat shield behind the spacecraft power-generation solar panel intercepts heat and radiates it to space through sky-facing black surface radiators. Between the hot solar panel and the Sun shield are multiple layers of low-emissivity thermally reflective multilayer insulation (MLI). The thermally conducting OS that encloses the Dewar. SIs, and the telescope is coated with high-emissivity black paint in the antisolar direction and has a low-emissivity heat-reflecting, bare metal finish in the Sunshield and SCB directions. The hot solar panel is attached to the SCB. It does not contact the CTA, eliminating this heat conduction path. The CTA is attached to SCB by means of low-thermal-conductivity gamma-alumina struts. A spacecraft heat shield attached to the struts between the bottom of the OS and the top of the SCB prevents radiation from the warm SCB from reaching the CTA OS. In flight, the CTA OS is running even cooler than the goal temperature of 37 K.

Inside the OS, the outer vapor cooled shield encloses the cryostat and telescope. The telescope and its inner barrel baffle are attached directly to the superfluid helium cryostat's outer vacuum shell. In orbit, the superfluid helium tank has been cooled to 1.2 K by venting it to space through a porous plug that serves as the phase separator between the superfluid liquid and the boiloff helium vapor.

The CT, including the optics and secondary mirror support metering tower, were all constructed of hot isostatically pressed (HIP) beryllium in order to minimize changes in the optical performance upon cooldown from 300 to 5.5 K and to minimize the weight of the assembly while retaining stiffness. The telescope itself is kinematically mounted to the cryostat outer vacuum shell by three titanium bipod flexures that are attached to the CT bulkhead. The primary mirror assembly is kinematically attached to the CT bulkhead by three additional titanium bipod flexures. The beryllium metering tower is attached directly to the bulkhead (see Figs. 8 and 6), and the secondary mirror assembly is mounted to the metering tower by three titanium bipod flexures. During the assembly and optical testing of the CTA, the bipod flexure attachment pads were shimmed and pinned so that the final bolted CT assembly met the design error budget allowances for the tilt, decenter, and piston of the various optical and mechanical components.

The SIs are enclosed in the MIC, an aluminum enclosure that protects the SIs from contamination condensates during the initial cryogen ground fill, provides the necessary SI mechanical support attachment structure, acts a cold plate for the SIs (Fig. 9), and provides a light-tight enclosure for instrument testing before launch at near-zero thermal background levels. A two-bladed rotating photon shutter in the MIC can be opened to allow light from the telescope to enter the instrument pickoff mirrors. This shutter, which blocked incoming photons during zero-background testing, was opened during optical testing in the BRUTUS chamber and then retracted permanently just before launch so that it did not become a potential single-point failure possibility in orbit. The MIC is attached directly to the helium cryostat. Surrounding the MIC and the helium tank is the inner vapor cooled shield which is covered with MLI to improve the cryostat cryogen ground hold time. The cryostat vacuum shell is also vapor cooled. In orbit, the heat-rejecting CTA design works so well that the helium cryogen lifetime is completely determined by the SI and makeup heater dissipation and not by parasitic heat loads from the hotter spacecraft and CTA components.

2. Optical design

The HIP beryllium Spitzer CT and the details of its installation into the CTA are shown in Figs. 6 and 8. Table II summarizes the optical design parameters of the CTA's Ritchey-Chretien telescope, designed to have diffraction-limited imaging performance over a field of view of 30′ at a wavelength of 6.5 μm to fulfill the science objectives of the Spitzer mission. A telescope that is diffraction limited at 6.5 μm has an optical wave-front error of $\lambda/14$ (0.464 μm rms) and produces a star image core whose peak energy is reduced to no less than 80% compared to the ideal telescope (Strehl ratio of 0.8).[14,15]

3. Optical and thermal performance testing program

The Spitzer project concluded early in the program that an end-to-end optical and thermal performance test conducted under flightlike thermal conditions would be required to assure that the CTA would meet the level-one performance

TABLE II. Optical characteristics of the Spitzer Telescope (Ref. 40).

Optimal parameter description	value at 5.5 K
System parameters:	
Focal length	10 200 mm
Focal ratio	$f/12$
Back focal length (PM vertex to focus)	437 mm
Field of view (diameter)	32.0 arc min
Field curvature radius	140.5 mm
Wavelength coverage	3–180 μm
Aperture stop:	
Location	Edge of primary mirror
Diameter of OD obscuration	850.00 mm
Diameter of ID obscuration	320.00 mm
Linear obscuration ratio	0.3765
Primary mirror (hyperbola)	
Radius (concave)	−2040.00 mm
Conic constant	−1.003 546
Clear aperture	850.00 mm
Focal ratio	$f/1.2$
Secondary mirror (hyperbola)	
Radius (convex)	−294.343
Conic constant	−1.531 149
Clear aperture (OD)	120.00 mm
PM to SM spacing (vertex to vertex)	887.528 mm

specifications in flight. With the warm-launch design, verifying the CTA thermal performance was particularly critical, because with only 360 L of liquid helium even a small amount of excess power input would dramatically shorten the mission lifetime. The low telescope temperature requirements also gave little margin for error in the thermal design or construction. In an ideal thermal performance verification test setup, the in-orbit environment would be replicated with the CTA mounted in a vacuum test chamber shielded by the Spitzer solar panel and its shield, with solar-strength illumination impinging on it from one direction, while in the other directions the CTA would be viewing a dark 3 K background. This ideal test setup is impossible to realize in practice, so the thermal performance of the CTA was instead verified before launch by a combination of modeling and testing in a modified thermal vacuum chamber at BATC.

This daunting and crucial test, named the BRUTUS test after the huge BATC cryogenic test chamber in which it was conducted, required about 165,000 L of liquid helium in two sessions totaling 87 days. The BRUTUS test chamber is BATC's largest thermal vacuum test chamber and its interior walls are cooled to liquid nitrogen temperatures (77 K). Since the calculated equilibrium temperature of the Spitzer outer shell was predicted to be lower than 40 K, the radiative background for the thermal tests was further reduced by employing a liquid helium cooled thermal shroud that surrounded the CTA within the BRUTUS chamber. It was impossible to lower the background and parasitic powers enough to actually demonstrate that we would achieve the predicted in-flight OS temperature. The lowest heat input to the CTA achieved in BRUTUS was about 50 mW, as compared to the approximately 4 mW load recorded under actual orbital conditions. However, the test was able to validate the model that was used to predict the in-flight performance. And, as is detailed below, the actual flight performance was slightly better than the model predictions.

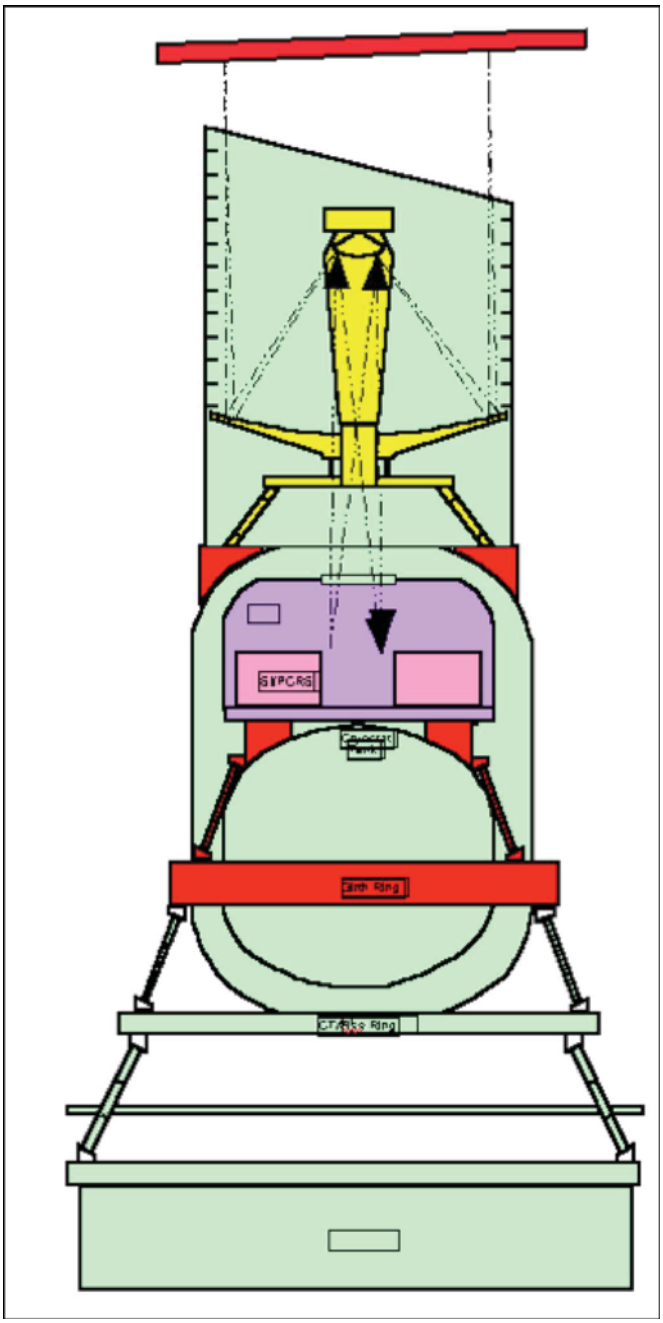

FIG. 11. Schematic view of the double pass BRUTUS autocollimation test (Ref. 18). The BRUTUS OSCAR optical flat (red) is suspended above the cryogenic telescope assembly to return an image of the point-source short-infrared glower to the focal plane of the MIC. Courtesy of J. Schwenker and Ball Aerospace.

In the BRUTUS optical tests (see Fig. 11), the light from a point source short-wavelength infrared (SWIR) glower, located in the telescope focal plane, was collimated by reflection through the CT, reflected off an optically flat mirror called OSCAR, and directed back to the IRAC, IRS, and PCRS instruments to form a returned image of the SWIR glower.

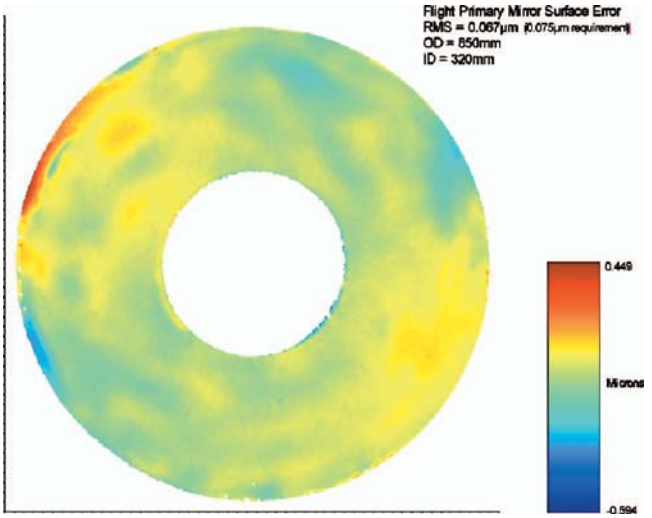

FIG. 12. (Color) Surface of the Spitzer beryllium primary mirror as measured at 10 K during the final cryogenic acceptance test. The root mean square (rms) surface error over the clear aperture was 0.067 μm. The error budget called for a maximum rms error of 0.075 μm (Ref. 40). There is no change in the figure of the mirror over its 5.5–13 K operating range. Courtesy of JPL-Caltech/NASA.

The optical testing approach taken during the fabrication of the CT leading up to BRUTUS was to test each individual component and subassembly during the assembly process. Cooling the room-temperature primary mirror to operating temperatures resulted in unacceptable optical-wave-front distortions that were corrected by polishing the complement of the cold wave-front figure onto the room-temperature primary mirror surface figure. This process is called "cryofiguring." The optics were figured warm and the $f/1.2$ concave hyperbolic primary mirror was extensively tested at ~300, 78, and 10 K using a cryogenic optics test facility at JPL. These tests involved accurately characterizing the surface figure of the primary mirror by producing an interferogram of the surface using a Zygo interferometer and two different null lenses that gave comparable results. Two cryogenic figuring cycles were conducted to remove cold temperature figure deformations in the primary mirror. Focus deformations due to gravity release in the single-arch primary mirror profile were modeled by comparing up-looking and down-looking interferometric tests of the warm mirror. The secondary mirror did not require cryofiguring to meet our level-one optical specification. It was verified using a room-temperature modified conjugate Hindle shell test performed at SVG Tinsley that showed it to have a rms surface error of 6 nm. Finite element modeling of the secondary mirror and its support structure predicted that it would meet the level-one optical performance requirements at operating temperatures. This was verified by end-to-end interferometric autocollimation cryotesting of the CT at JPL prior to the final end-to-end autocollimation testing of the integrated CTA in BRUTUS at BATC, as described below. The end-to-end optical test at JPL required a warm window in the test Dewar, but no null lens.

Figure 12 shows the 67 nm rms surface figure of the primary mirror of the CT as measured during its final cryogenic acceptance test. Figure 13 shows the assembled telescope prior to its integration into the CTA.

FIG. 13. The assembled cryogenic telescope at the Jet Propulsion Laboratory mirror laboratory. One of the titanium bipod flexures that mount the bulkhead to the cryostat is visible under the reflection of the metering tower in the primary mirror. The mechanism at the top of the metering tower was used to move the secondary mirror in piston during the in-orbit checkout focus procedure. Courtesy of NASA/JPL-Caltech.

Once assembled and verified by end-to-end interferometric tests at JPL, the CT was integrated with the SIs, MIC, and cryostat at BATC to produce the CTA. The CT and near-infrared instruments were then tested in autocollimation at operating temperatures in the BRUTUS test (see Fig. 11). The BRUTUS full aperture cold autocollimation flat (OSCAR) is a thin (aspect ratio of 18 to 1) fused-silica, flat mirror suspended by an 18-point whiffle tree. The mirror and its support were constructed by REOSC. The OSCAR cold wave-front figure was determined from multiple subaperture tests so that its focus and aberrations could be backed out of the optical tests. The primary OSCAR aberration was a repeatable and predictable "power" (focus) term associated with its development of a 3.565 km convex radius of curvature at 10 K, equivalent to an ~30 mm focus change in the $f/12$ CT focal plane (greater than the available focus mechanism travel range of ±24 mm). Thus, in its original position, the SWIR would have been out of focus for the focus range of the secondary mirror during the BRUTUS test. Fortunately, this problem was identified during piecewise testing of the OSCAR component, and a failure of the BRUTUS test that could have cost the project in excess of $100M was averted. The solution was to place the SWIR ~30 mm below the focal plane. The illumination from the SWIR glower had

to traverse a semitransparent window in the ADM, which was necessary to maintain the vacuum of the cryostat, as described in Sec. III B above. The long-wavelength cutoff of the ADM window precluded making preflight optical tests at wavelengths beyond ~5 μm. The BRUTUS optical test had two primary objectives: (1) to verify the end-to-end optical performance of the CT and the near-infrared SIs, and (2) prior to launch, to enable the project to set the CT focus at the best compromise SI focus position predicted for the zero-gravity flight environment. Single- and double-pass models of the CT point-spread function were constructed from the component and BRUTUS test data to confirm that the level-one requirements were met and for use during activities to focus the telescope during IOC.[16]

4. Focusing the CTA in orbit

The CTA was focused during IOC by using a cryogenic focus motor mechanism to move the secondary mirror. Because a failure of this mechanism could have caused a single-point failure in Spitzer's ability to meet its science objectives, the project developed a plan to bring the CTA into focus with a minimal number of discrete focus motor actuations rather than by conducting a conventional focus scan. Software tools enabling us to analyze the shapes and sizes of star images to determine the focus position of the telescope were developed by Hoffmann *et al.*[17] and tested by the Spitzer IOC Focus Integrated Products Team prior to launch (see Ref. 18). During IOC, these tools allowed us to track the telescope focus by passively imaging stars as the CTA cooled to its operating temperature. The data were used to determine the magnitude and direction of the secondary-mirror move necessary to focus the telescope. The aliveness test images and IOC focus history of Spitzer are shown in Figs. 14 and 15.[16] Satisfactory refocus was accomplished in two motor moves.[16] The improvement gained by focusing IRAC channel 1 is shown in Fig. 16.

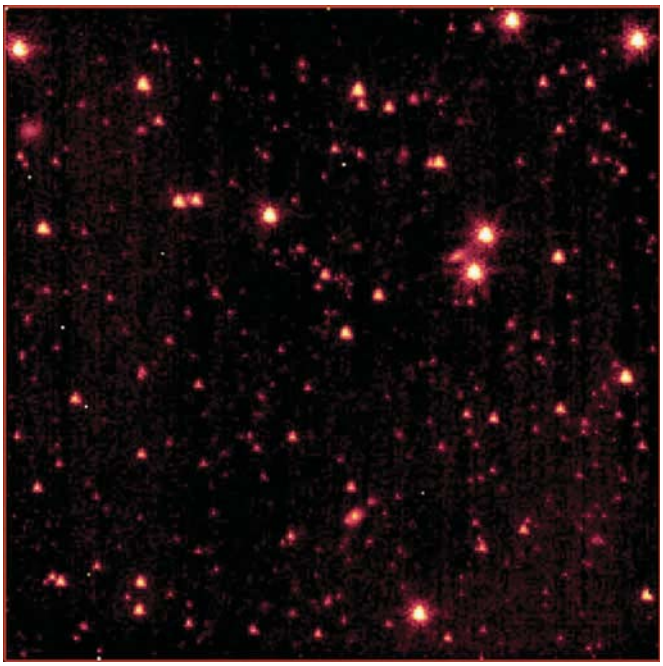

FIG. 14. The Spitzer IRAC 3.6 μm first light image, taken 7 days after orbital insertion, verified that the observatory was operating within its optical design parameters. The $5' \times 5'$ (red box) image was produced from a 100 s exposure of a low galactic latitude region in the constellation Perseus. Courtesy of NASA/JPL-Caltech.

IV. FOCAL PLANE INSTRUMENTATION

Wide field, broadband imaging from 3.6 to 160 μm is conducted with the IRAC (Ref. 19) and MIPS.[20] Low- and moderate-resolution spectroscopic capabilities are provided by the IRS,[21] which also has imaging capabilities at 15 and 24 μm using "peak-up" arrays. MIPS also provides low-resolution spectroscopy from 55 to 95 μm. The Spitzer focal plane layout is shown in Fig. 17. Table III summarizes the overall imaging, spectroscopic, and expected sensitivity capabilities of Spitzer SIs. We describe the capabilities of the individual SIs in detail in the sections that follow.

A. Infrared array camera

IRAC is a four-channel imager that uses dichroic beam splitters to enable simultaneous $5.2' \times 5.2'$ paired images in two adjacent fields of view (3.6 and 5.8 μm; 4.5 and 8.0 μm).[19] Each of the four detector arrays is 256 $\times$256 pixels in size, with a pixel size of $1.22'' \times 1.22''$. Mapping can be performed in either array or celestial coordinates using several dither patterns to subsample pixels, reject cosmic rays, and identify fast-moving proper-motion objects. IRAC observing is done using the IRAC mapping/photometry observing template that can be accessed using the SPITZER PRIDE software package.[22] IRAC can also perform high dynamic range and subarray imaging of bright sources. IRAC was built by the NASA Goddard Space Flight Center; the Smithsonian Astrophysical Observatory (SAO) has management and scientific responsibility.

IRAC was designed primarily to study the birth and evolution of normal galaxies in the early universe by means of deep, large-area surveys. Using the broad 1.6 μm emission peak in the stellar spectrum of normal galaxies, the IRAC wavelength bands permit the determination of photometric redshifts for $1 < z < 5$.[23] The IRAC sensitivity requirements were driven by the goal to achieve a signal to noise of 10 on an L_* galaxy at $z=3$ in all four wavelength bands.[24] IRAC offers the opportunity to study, for the first time, star formation processes in the early universe and yield information about the age and mass of a galaxy's stellar population. However, IRAC is a general-purpose wide-field camera that can also be used to study the structure and morphology of nearby galaxies, active galactic nuclei, and interacting galaxies, as well as the early stages of star formation and evolution in our galaxy and nearby galaxies, transiting planets, planetary nebulae, and brown dwarfs.

IRAC consists of two parts: the cryogenic assembly (CA) (Fig. 18), mounted in the MIC within the CTA, and the warm electronics assembly (WEA), mounted in the payload assembly area below the CTA. The IRAC CA contains the four IRAC infrared cameras with their associated transmission optics, filters, beam splitters, and array detectors. Also included in the CA is a transmission calibrator with its source and integrating spheres. The CA is cooled to the MIC

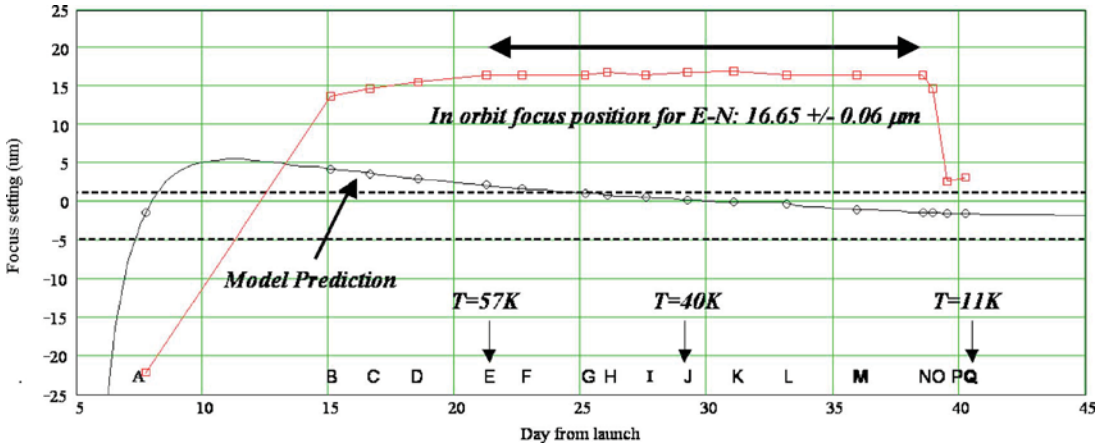

FIG. 15. Evaluation of the focus position showed that focus had stabilized at 1.8 mm above the nominal multiple instrument chamber focal plane by day 22. The secondary mirror mechanism was activated twice during the day 38–40 focus campaign to bring the optical performance within the level one specification. Reproduced courtesy of Gehrz *et al.* (Ref. 16).

base-plate temperature of 1.2 K. The CA has a mass of 11.1 kg and is 0.15 m high and 0.28 m wide at its outer edge. It consumes an average of 3.0 mW of power during nominal operation. The WEA is mounted in Bay 5 of the spacecraft, operating at near room temperature at 283 K. The WEA provides all power, data, and command interfaces to both the spacecraft and the CA. The WEA has a mass of 24.5 kg, and its dimensions are 0.4 m in length, 0.38 m in width, and 0.23 m in height. It consumes 56 W of power during normal operations.

The IRAC optical design is shown in Fig. 19. Light from the telescope enters the CA via two pickoff mirrors, which are slightly displaced and tilted to separate the incoming beam into two fields of view, with $5.2' \times 5.2'$ images on the sky and centers separated by 6.8′, leaving a gap of about 1.5′ between the fields of view. The lower mirror selects channels 1 (3.6 μm) and 3 (5.8 μm) and the upper mirror channels 2 (4.5 μm) and 4 (8.0 μm). Channels 1 and 3 contain a MgF_2–ZnS vacuum-spaced doublet lens that reimages the Spitzer focal plane onto the detectors. Channels 2 and 4 contain a ZnSe–BaF_2 doublet lens. Following each doublet is a germanium-substrate beam splitter that reflects the channel 1 or 2 beam and transmits the channel 3 or 4 beam. Germanium filters and Lyot stops follow the beam splitters. Barr Associates, Inc., Westford, Massachusetts, produced the filters; OCLI-AJDS Uniphase Co., Santa Rosa, California, the beam splitters; and Spectral Systems, Inc. Dayton, Ohio, the lenses. IRAC has two internal calibration systems: one is the transmission calibrator, to measure the optical throughput of the system, and the other consists of the flood calibrators, located near the detectors to measure the array detector responsivity and stability. Figure 20 shows the spectral responsivity profile of the four IRAC channels.

The IRAC optics produce diffraction-limited imaging, with wave-front errors less than $\lambda/20$ in each channel. The overall IRAC image quality is a combination of the IRAC optics, and the pixel size, diffraction, and the optical quality of the telescope. At the center of the array, the full widths at half maximum (FWHMs) of a point source are 1.44″, 1.43″, 1.49″, and 1.71″ for channels 1, 2, 3, and 4, respectively. The mean FWHMs of a point source over the array are 1.66″, 1.72″, 1.88″, and 1.98″.

A shutter at the entrance to the CA was built into IRAC to permit the measurement of the dark count rate of the array detectors and to permit absolute flux measurements. A mirror, mounted on the rear of the shutter, was to be used to reflect radiation from the transmission calibration source into the two optical paths to measure the system throughput. Preflight tests of the shutter mechanism revealed an anomaly, and to eliminate the possibility that the shutter might not open once closed, it has never been used during flight. Likewise the transmission calibrators also have not been used for this reason. The flood calibrators, mounted near the array detector surfaces, are used to confirm detector aliveness and relative responsivity and stability.

The IRAC detector arrays were developed by Raytheon (formerly Santa Barbara Research Corporation), Goleta, California, under contract to SAO.[25,26] Channels 1 and 2 each use an InSb array and channels 3 and 4 each use a Si:As blocked impurity band (BIB) array. The InSb arrays are operated at a temperature of 15 K and the Si:As arrays at a temperature of 6 K. To satisfy the relative photometric accuracy requirement of 2%, all the array heaters had an active feedback loop to control the temperature to less than 10 mK peak-to-peak (p-p). In actual flight, less than 5 mK p-p has been achieved. All the arrays contain 256×256, 30 μm square pixels. The multiplexer design used cryo-CMOS (complementary metal oxide semiconductor) technology.[27] The arrays for channels 1, 2, and 3 are antireflection coated with SiO; the channel 4 array is coated with ZnS. The arrays are read out using four output amplifiers. The power dissipation for each array during nominal operations is less than 1 mW. The individual array detector properties are given in Ref. 19. The arrays can be annealed by raising their temperatures to 20 to 30 K for approximately 2 min to remove hot pixels and residual images. The InSb arrays were tested and characterized at the University of Rochester[28,29] and the Si:As arrays at the NASA Ames Research Center.[30] The flight arrays were evaluated at the NASA Goddard Space Flight Center. More information on the IRAC detector char-

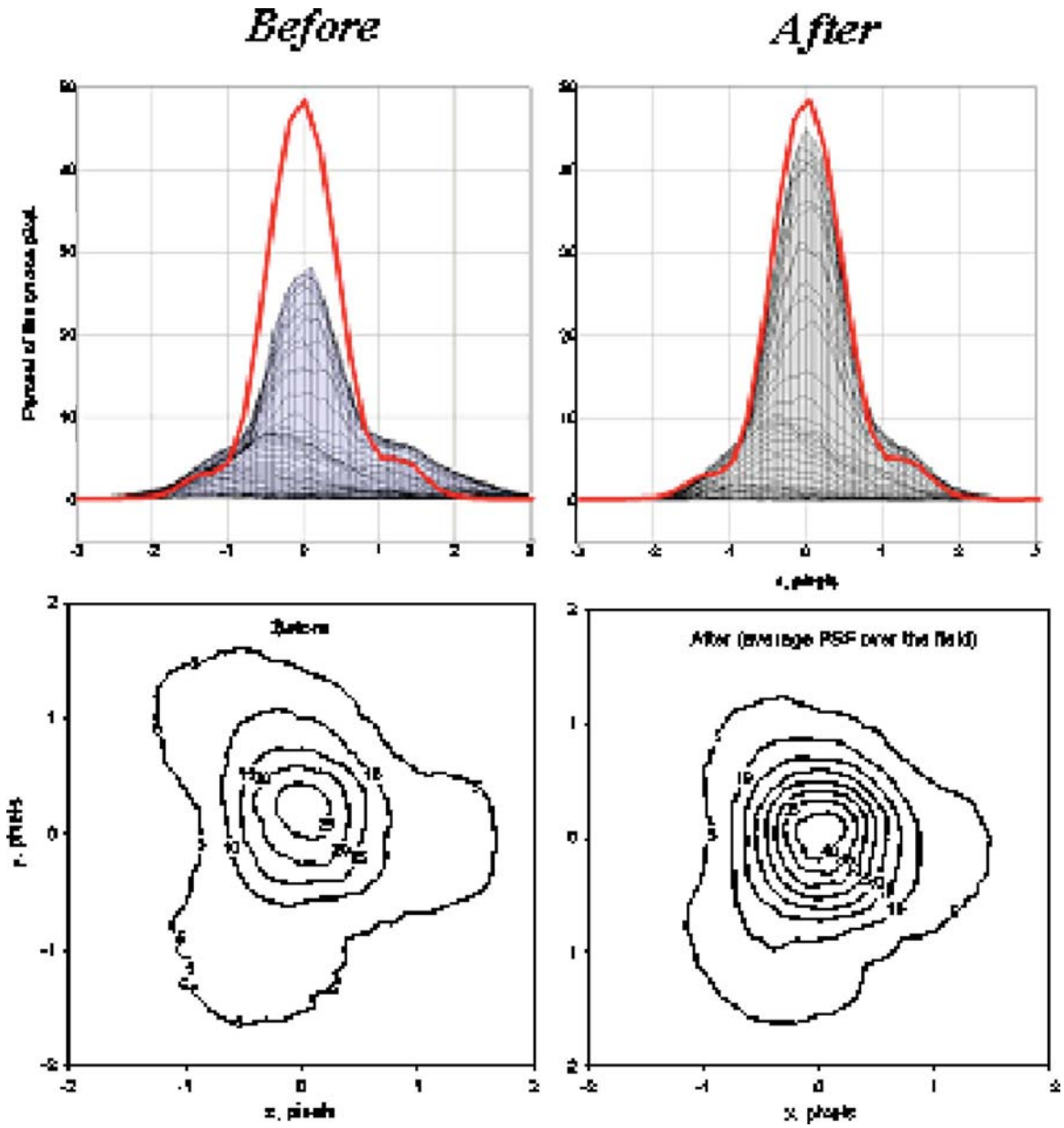

FIG. 16. The IRAC channel 1 point spread function (PSF) before and after focusing. Top panels: Solid curves are a cross section of the prelaunch optical model PSF for best focus. The solid surface is the observed in-flight PSF averaged over the field of view (FOV). Bottom panels: Isophotal contours in units of total flux collected on the central pixel. The data analysis was produced by Elliot of JPL-Caltech/NASA. Reproduced courtesy of Gehrz *et al.* (Ref. 16).

acteristics can be found in the Spitzer Observer's Manual[31] and in the IRAC Pocket Guide (Fig. 21).

IRAC has one mode of operation: stare and integrate. There are two readout modes, one using the full 256 $\times$256 pixel array, and the other using a 32$\times$32 pixel subarray that can be read out at a faster rate. The standard readout times for the full array are 2, 12, 30, 100, and 200 s, except that channel 4 uses two or four 50 s readouts instead of 100 and 200 s. The standard times for the subarray mode are 0.02, 0.1, and 0.4 s. IRAC is also used in a high dynamic range mode where a long exposure is preceded by one or more shorter exposures: 0.6, 12 s; 1.2, 30 s; 0.6, 12, 100 s; and 0.6, 12, 200 s. The arrays are operated simultaneously during flight, although each array is capable of independent operation.

The data from the IRAC detector arrays are read out using the Fowler-sampling mode[32] to reduce the effective read noise. This readout method consists of taking N nondestructive reads immediately after the reset (pedestal level) and another N destructive reads near the end of the integration time (signal level). The average of the pedestal levels is subtracted from the average of the signal levels to derive the signal. These functions are carried out in the onboard IRAC electronics to generate a signal image from each array for each integration time, which is stored and then transmitted to the ground. N can have values from 1 to 64. The value of N used depends on the integration time and has been selected to maximize the signal-to-noise ratio based on ground-based tests.

The point-source IRAC sensitivities are given in Table III, in Fig. 21, and in the Spitzer Observer's Manual.[31] For extended emission in channels 3 and 4, the calibration differs

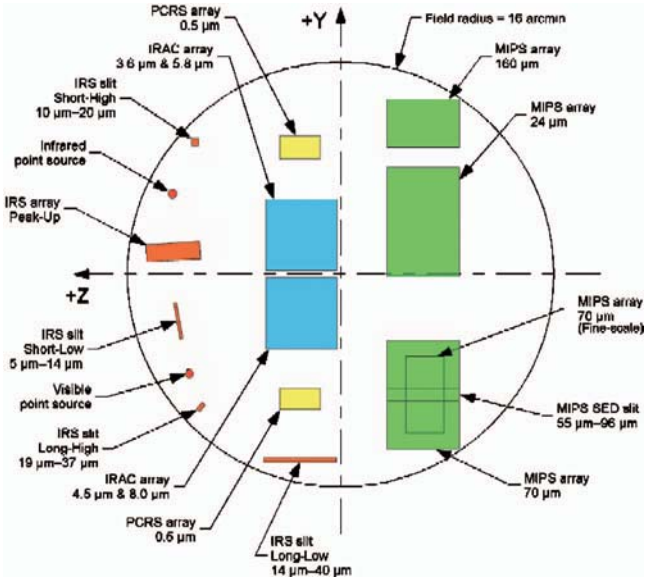

FIG. 17. (Color) Spitzer focal plane layout seen looking down from the telescope aperture showing the footprints of the science instrument apertures, the PCRS arrays, and the point sources used for ground-based prelaunch focus checks and focal plane mapping. The +Z direction points toward the Sun. The MIPS apertures appear rectangular because the scan mirror accesses an area larger than the instantaneous footprint of the array; the positions of the SED slit and fine-scale array are shown schematically. Reproduced courtesy of Werner *et al.* (Ref. 2)

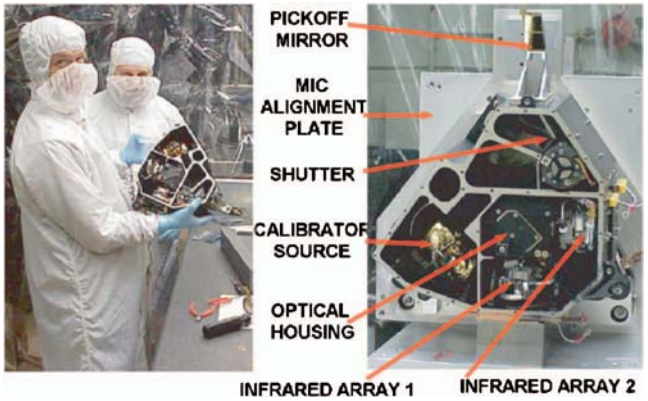

FIG. 18. (Color) The IRAC cryogenic assembly with the top cover removed to show the inner components. The MIC alignment plate was used only for testing prior to cryogenic telescope assembly integration. Arrays 1 and 2 are the channel 4 and 2 focal plane assemblies, respectively. Reproduced courtesy of Fazio *et al.* (Ref. 19).

from that of a point source. For photometry using different size apertures, the estimated correction is listed in Table 5.7 of the Spitzer Data Handbook.[33]

In flight, the absolute calibration of IRAC is carried out by observing a set of standard stars.[34,35] A wide variety of stars with a range of spectral indices and fluxes was selected and observed at a number of positions on the array and many times during the mission to monitor any changes. The zero magnitude (Vega) fluxes are 280.9, 179.7, 115.0, and 64.1 Jy for channels 1, 2, 3, and 4, respectively.[31] Reach *et al.*[36] have summarized the IRAC absolute calibration procedures and results. They found that IRAC has a stable gain on all measured time scales, making it possible to measure variability at the 2% level for carefully reduced data. The absolute calibration using stellar photospheric models scaled to ground-based photometry is accurate to 2%, but requires the application of several photometric corrections. Details of the science basic calibrated data (BCD) pipeline, identification

TABLE III. Spitzer instrumentation summary.

λ (μm)	Array type	λ/Δλ	FOV	Pixel size (arc sec)	Sensitivity[a] (5σ in 500 s)
	IRAC: infrared array camer—P.I. Glovanni Fazio, Smithsonian Astrophysical Observatory				
3.6	InSb	4.7	5.2′×5.2′	1.22	1.3 μJy
4.5	InSb	4.4	5.2′×5.2′	1.21	2.7 μJy
5.8	Si:As (IBC)	4.0	5.2′×5.2′	1.22	18 μJy
8.0	Si:As (IBC)	2.7	5.2′×5.2′	1.22	22 μJy
	MIPC: multiband imaging photometer for SIRTF—P.I. George Rieke, University of Arizona				
24	Si:As (IBC)	4	5.4′×5.4′	2.5	110 μJy
70 wide	Ga:Ga	3.5	5.25′×2.6′	9.8	7.2 mJy
70 fine	Ge:Ga	3.5	2.6′×1.3′	5.0	14.4 mJy
55–95	Ge:Ga	14–24	0.32′×3.8′	9.8	200 mJy
160	Ge:Ga (stressed)	4	0.53′×5.3′	16	24 mJy
	IRS: infrared spectrography—P.I. Jim Houck, Cornell University				
5.2–14.5	Si:As (IBC)	60–127	3.6″×5.7″	1.8	400 μJy
13–18.5 (peak-up imaging)	Si:As (IBC)	3	1′×1.2′	1.8	75 μJy
9.9–19.6	Si:As (IBC)	600	4.7″×11.3″	2.4	1.5×10^{-18} W m^{-2}
14–38	Si:Sb (IBC)	57–126	10.6″×168″	5.1	1.7 mJy
18.7–37.2	Si:Sb (IBC)	600	11.1″×22.3″	4.5	3×10^{-18} W m^{-2}

[a]Sensitivity numbers are indicative of *Spitzer* performance in low-background sky. Confusion is not included. Detailed performance estimates should be based on tools available at http://ssc.spitzer.caltech.edu/obs

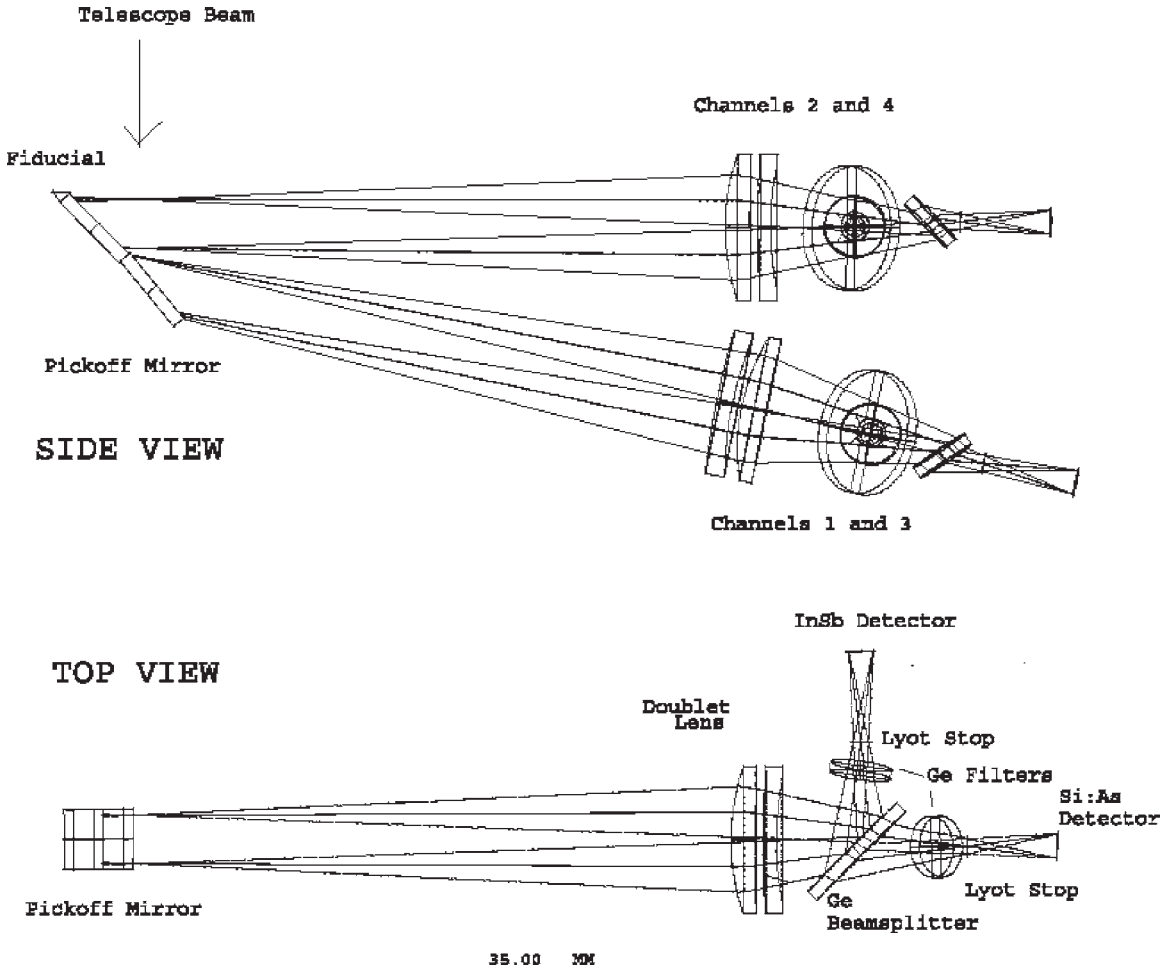

FIG. 19. Top and side elevations of the IRAC optical system. Each of the two modules uses a dichroic filter to separate the incoming light into two bands, and the filters are place near Lyot stops to ensure color uniformity over the field of view. Reproduced courtesy of Fazio *et al.* (Ref. 19).

and removal of detector artifacts and cosmic ray effects, photometry and calibration, and post-BCD data processing are available in the IRAC Data Handbook.

In flight, IRAC meets all of the science requirements that were established before launch and in many cases the performance is better than expected. IRAC remains a powerful survey instrument because of its very high sensitivity, large field of view, and four-color imaging. In channel 1, IRAC can reach the same point-source sensitivity as the W. M. Keck Interferometer at the L band (2.9–3.2 μm) in 1/100 the exposure time and does so with a far larger field of view ($5' \times 5'$ vs $40'' \times 40''$). The noise measurements in channels 3 and 4 have been shown to scale as the inverse square root of time for integration times as long as ~24 h. Channels 1 and 2 deviate from this rule in approximately 2000 s, which indicates that these channels are approaching the source completeness confusion limit.[37] However, by selecting isolated sources in channel 1 and 2 images, it has been demonstrated that IRAC can reach a limit of 0.10 μJy [26.4 magnitude (AB); 5] in 23.4 h.[38] At such depths galaxies at redshifts of 5 and 6 have been detected easily. The high photometric stability of IRAC was also demonstrated in the first detection of thermal radiation from a planet orbiting another star.[39] This and additional scientific results that are discussed in this article and previously presented in a special issue of the *Astronomical Journal* (Volume 154, 2004) are examples of IRAC's great potential for producing exciting new science with the Spitzer Space Telescope.

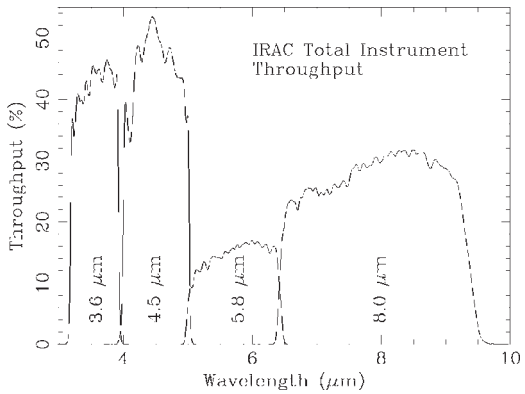

FIG. 20. IRAC optical system total throughput, including transmission of the cryogenic telescope assembly, IRAC optics, and detector quantum efficiency. Reproduced courtesy of Fazio *et al.* (Ref. 19).

B. Infrared spectrograph

IRS (Fig. 22) gives Spitzer low- and moderate-resolution spectroscopic capabilities from 5.3 to 38 μm, as summa-

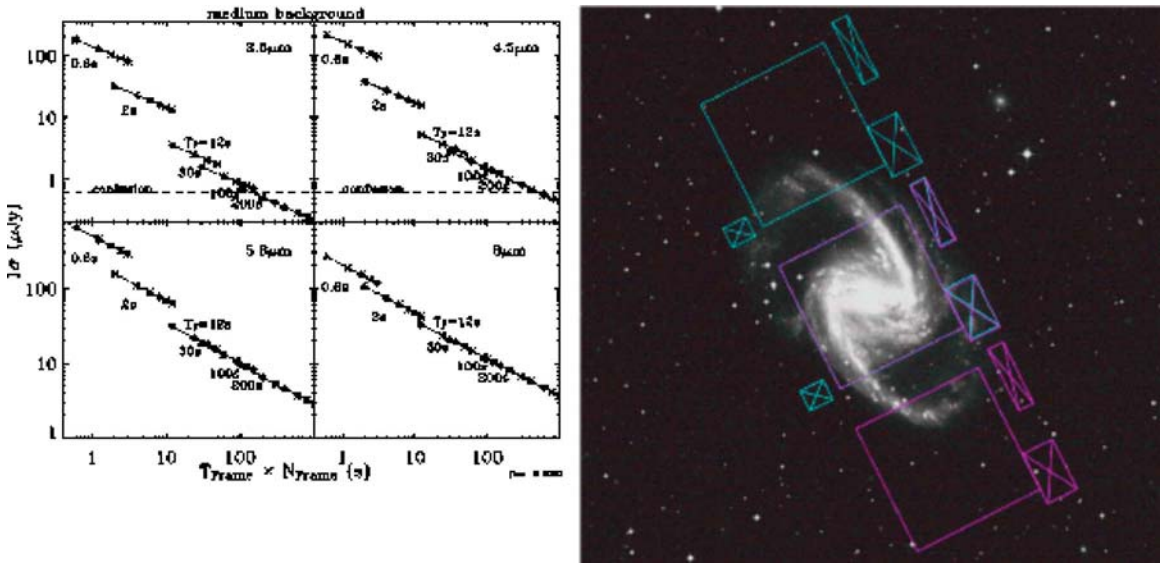

FIG. 21. The IRAC Pocket Guide, which gives details about the observing modes and on-orbit sensitivity of IRAC, can be downloaded by prospective users at http://ssc.spitzer.caltech.edu/irac/documents/pocketguide.pdf

rized in Fig. 23. Originally, IRS was envisaged as a single large instrument with many moving parts and with a much wider spectral range and resolution coverage. As part of the overall reduction in the Spitzer project's cost, the IRS instrument was redesigned according to the following axioms.

(1) Spitzer was a cost-driven mission, and the IRS development would adhere to this philosophy.
(2) Boeing Si:As and Si:Sb 128×128 BIB arrays would be used.
(3) The IRS would have an aluminum housing and aluminum optics.
(4) Only simple optics would be used:
   (a) surfaces of revolution only (off-axis optics allowed);
   (b) flat diffraction gratings (single blaze and pitch);
   (c) "bolt and go" (no adjustments).
(5) IRS would have no moving parts (no shutters or grating drives).
(6) Redundant electronics for credible single point failures.
(7) Optical efficiency of 80%.

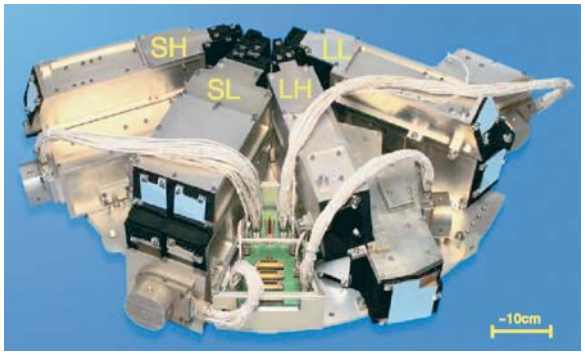

FIG. 22. (Color) The IRS modules, short-high, short-low (which includes the peak-up cameras), long-high, and long-low installed on the multiple instrument chamber test plate before integration into the cryogenic telescope assembly. The location of the spectrograph slits in the focal plane is shown in Fig. 7. Reproduced courtesy of Houck *et al.* (Ref. 21)

(8) IRS would be capable of internal health assessment.

The application of these axioms in conjunction with the Spitzer science goals mentioned earlier guided the design and testing of the IRS. The resulting design involved four autonomous spectrographs, two low-resolution spectrographs (see Fig. 24), and two high-resolution modules (see Fig. 25), each with its own optical train and detector. Each of the low-resolution spectrographs operates in both first and second orders. The order selection is made by moving the source along the length of the slit to one of the two order-selecting filters. The short-wavelength low-resolution module also has an imaging capability to aid in acquiring the science target at either 16 or 24 μm. Once the image of a peak-up source (either the science target itself or a reference star whose offset with respect to the science target is well known) is completed, the onboard software calculates its centroid and commands the pointing system to move the science target to the center of the array. A second exposure is then taken. The refined centroid is then used to command the pointing system to move the science target to the desired module and slit. The peak-up and science targets may be the same or the peak-up target can be a nearby reference star. The peak-up cameras have also been used for many photometric studies at these two wavelengths, and IRS peak up is the only way to obtain images at 16 μm with Spitzer.

Each high-resolution module has a short slit and operates as a crossed-echelle spectrograph covering ten spectral orders. There is a bandpass filter at the entrance slit. A first order grating is used as the cross dispersing element so the modules are confined to a single octave. A hot wire source is mounted near each of the arrays to provide a secondary calibration of the array response. The combination of the source and the array achieves a photometric stability in the range of $\sim2\%$.

In each module, the optical elements are mounted on the outside of a structural housing box with their optical surfaces projecting inward through openings in the housing. The op-

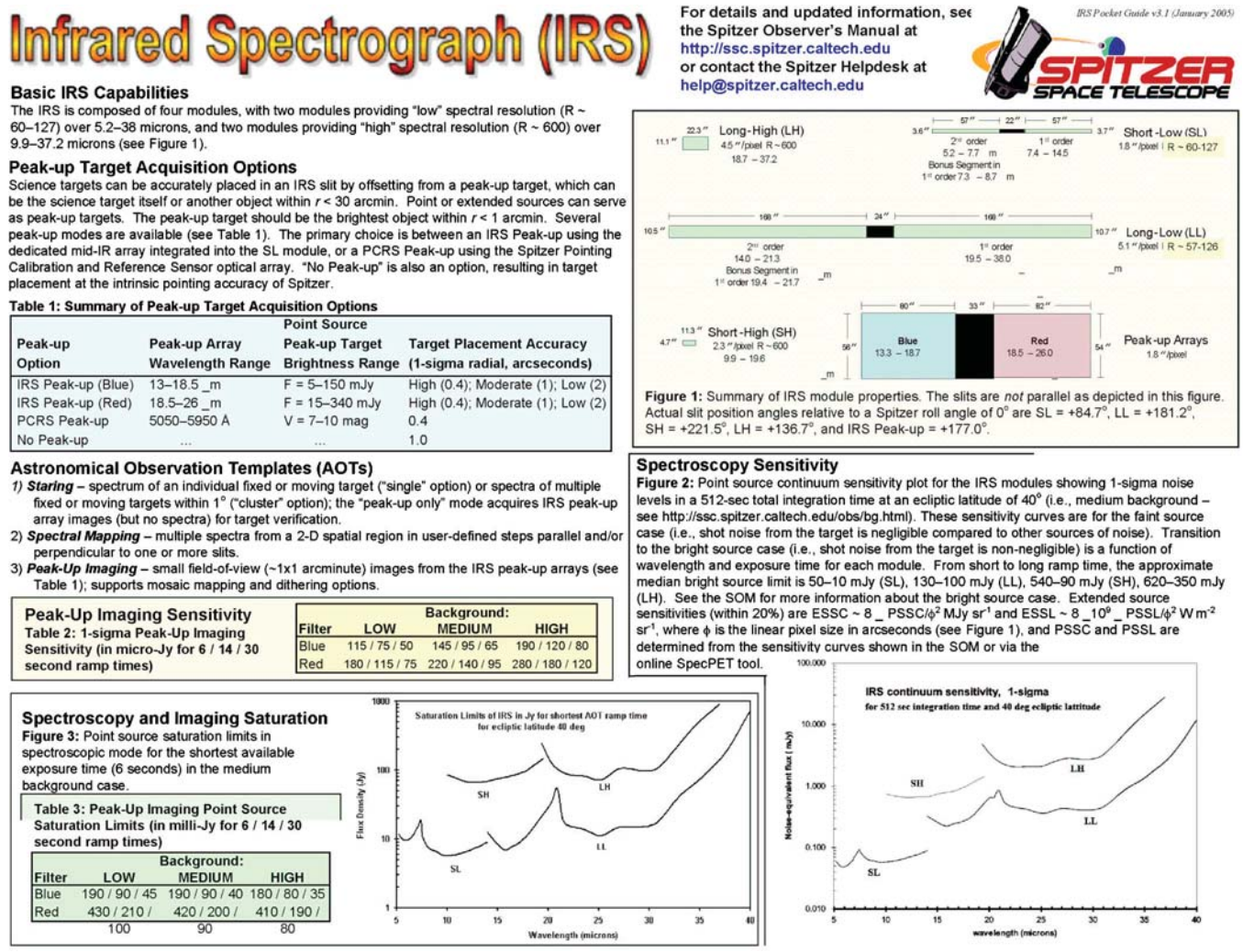

FIG. 23. The IRS Pocket Guide, which gives details about the observing modes and on-orbit sensitivity of IRS, can be downloaded by prospective users at http://ssc.spitzer.caltech.edu/irs/documents/pocketguide.pdf

tical baffles are mounted inside the box and provide much of the needed rigidity to keep the system in alignment. This approach greatly reduces the mass of the support system. The back sides of the optical elements, as well as the optical surfaces, are diamond machined. The optical elements are mounted on the housing with three mounting tabs and screws. The positions of the flat back sides of the optical elements were measured with a Zygo interferometer to assure that they were mounted at the intended angle and had not been deformed in the mounting process. The detector arrays are mounted to the housing via an interface plate that was custom machined to place the as-built location of the detector array in the focal plane of the spectrograph. Because

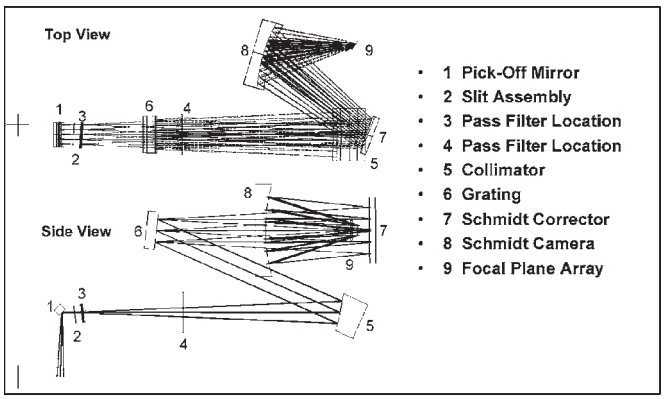

FIG. 24. Schematic view of the IRS long-low module optical components and paths (Ref. 81).

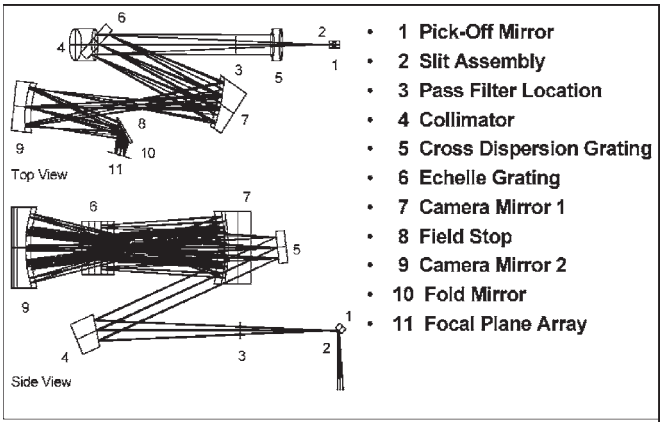

FIG. 25. Schematic view of the IRS long-high module optical components and paths (Ref. 81). An echelle grating is used to enhance the resolution.

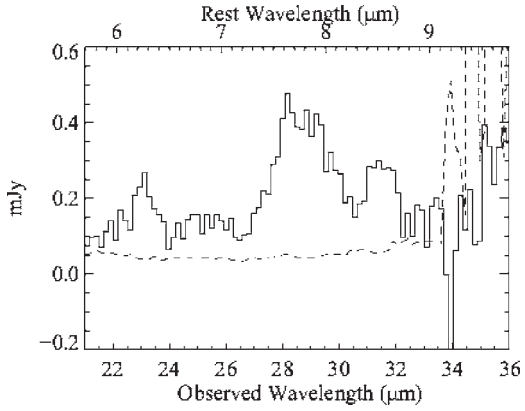

FIG. 26. A long duration (12 h) IRS long-low-1 spectrum of a $z=2.69$ Chandra soft x-ray source in the Hubble UltraDeep Field. The MIPS 24 μm flux is ~0.15 mJy. The solid line is the spectrum and the dashed line is the 1σ error. Courtesy of Teplitz *et al.* (Ref. 82).

the optics and the housings are all made from aluminum with virtually the same thermal expansion properties, the modules remain in focus from room temperature to the cryogenic operating temperature. The sides of the housing in the vicinity of the detectors are thickest (typically 10 mm) to provide shielding from solar protons and low energy cosmic rays. Another benefit of this modular design is that one or more individual modules could be in test while the others were being fabricated, assembled, and warm tested, thus reducing the complexity and duration of the test program. The final optical tests were done with all four modules mounted on the flight baseplate inside the test Dewar.

The sensitivities of the individual modules were measured using a near-room-temperature blackbody mounted outside of the module test cryostat at the relative location of the telescope's exit pupil. Stacks of neutral density filters mounted on the liquid nitrogen and liquid helium temperature radiation shields reduced the incoming signal and background light levels by factors of up to 10^6 depending on the module and its wavelength range. The spectral calibrations were determined by using a room-temperature half-meter grating spectrograph with a first order ~60 μm grating. In this way several higher orders of diffraction were observed at one time and the ratios of the wavelengths were well determined. An ammonia absorption cell was used to establish specific wavelengths to determine the absolute wavelength

MULTIBAND IMAGING PHOTOMETER FOR SPITZER (MIPS) http://ssc.spitzer.caltech.edu/mips/
Pocket Guide

Basic MIPS Capabilities:

Imaging photometry at 24, 70, and 160 μm and low resolution (R = 15 – 25) spectroscopy between 55 and 95 μm. A fine pixel scale option at 70 μm (no change required for the other two bands), combined with precise subpixel sampling dither patterns, allow data processing to achieve "super resolution" imaging. A cryogenic scan mirror mechanism provides freeze frame scan mapping, efficient dithering, and other instrument capabilities.

MIPS Instantaneous Fields of View:

24 μm	5.4×5.4 arcminutes
70 μm	5.25×2.6 or 2.6×1.3 arcminutes
160 μm	0.53×5.33 arcminutes (effective)
SED Slit	3.8×0.32 arcminutes

Basic Sensitivities (low background):
5 sigma in 500 seconds on source

24 μm	110 μJy
70 μm default	7.2 mJy
70 μm fine	14.4 mJy
SED	82/201/447 mJy @ 60/75/90 μm
160 μm	29 (40 w/ confusion) mJy

Prepared by:
William B. Latter
SSC/MIPS Instrument Support Team Lead

(v6.5, updated 31 October 05, LMR)

The MIPS Astronomical Observation Templates:

Photometry & Super Resolution
- Telescope staring mode imaging photometry

Scan Mapping
- Freeze frame mapping in all three bands with constant telescope slewing

Spectral Energy Distribution (SED)
- Low resolution (R = 15 – 25) spectroscopy over 55 to 95 μm (half power response points)

Total Power Mode
- Zero level brightness of very extended emission

The MIPS Detector Arrays:

24 μm	Si:As (IBC) 128x128 pixels; 2.55" 4.7 μm bandwidth
70 μm	Ge:Ga 32x32 pixels; 4.99" or 9.84" 19 μm bandwidth SED R = 15 – 25 (9.84" pixels)
160 μm	Stressed Ge:Ga 2x20 pixels; 16.0" 35 μm bandwidth

Saturation Limits:
Point source in 1 second (Jy); Extended source in 10 seconds (MJy/ster)

Band	Point Source	Extended
24 μm	4.1	260
70 μm (default)	23	101
70 μm (fine)	57	292
SED @ 60,75,90μm	250/290/1000	1087/1261/4350
160 μm	3	20

SSC Spitzer Science Center
SPITZER SPACE TELESCOPE

FIG. 27. The MIPS Pocket Guide, which gives details about the observing modes and on-orbit sensitivity of MIPS, can be downloaded by prospective users at http://ssc.spitzer.caltcech.edu/mips/documents/pocketguide.pdf

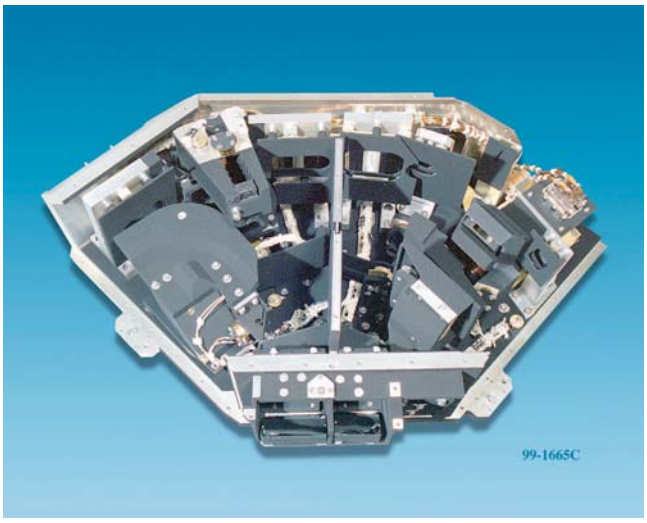

FIG. 28. (Color) The MIPS instrument prior to its integration into the multiple instrument chamber. Reproduced courtesy of Rieke *et al.* (Ref. 20).

calibration. Houck *et al.*[21] have described the details of the calibration procedures.

Once Spitzer was in-orbit the wavelength calibrations were refined using various planetary nebulae, γ Cas, and Wolf-Rayet stars. The photometric sensitivities were determined using a set of A dwarfs and K giants.

A set of common electronics was built to operate the IRS and MIPS to save costs because both instruments use the same silicon based detector types. The MIPS program supplied the front-end electronics for their germanium-based detector arrays. Figure 22 shows the four IRS modules mounted on their baseplate and bolted to the Spitzer cryostat following delivery of the IRS to the project in March 2000. The in-flight performance of the IRS is presented in Table III and is updated in the current version of the Spitzer Observer's Manual (SOM).[40] Figure 26 shows a 12 h exposure of a distant ($z\sim2.6$) galaxy using the first order of the long-wavelength low-resolution module (LL1). The rms noise is about 50 μJy. This is $\sim$1000 times smaller than the 24 μm 5σ detection limit of the IRAS mission.

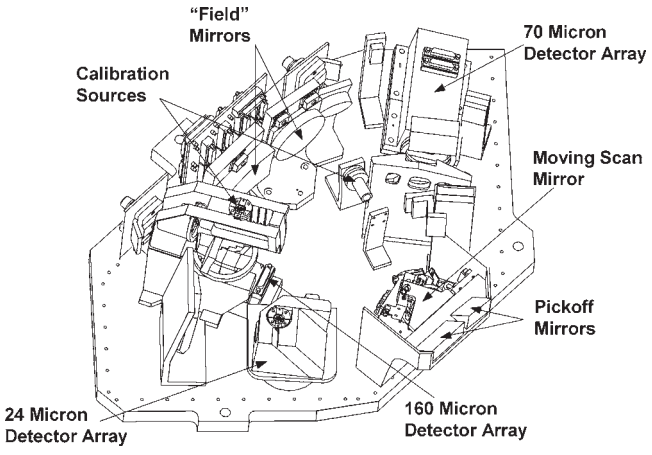

FIG. 29. Schematic drawing of the MIPS instrument showing the principal components. Reproduced courtesy of Rieke *et al.* (Ref. 20).

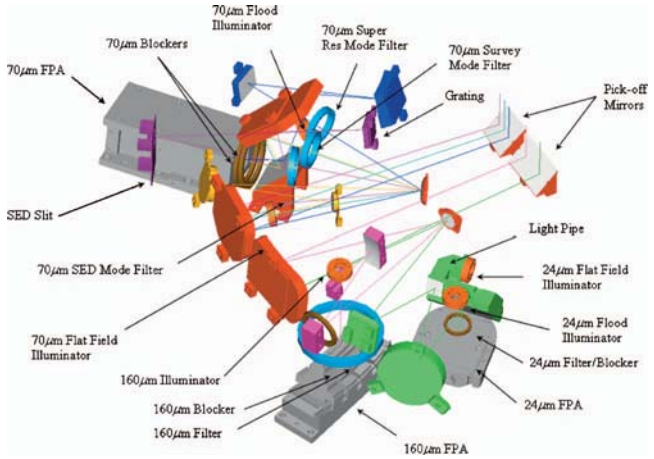

FIG. 30. (Color) Schematic diagram of the MIPS optical train. The two mirror facets attached to the cryogenic scan mirror mechanism (CSMM) feed the 70 μm optical train (normal FOV, narrow field of view and spectrometer/SED) and the 24/160 μm optical trains, respectively. The CSMM provides for chopping, one-dimensional dithering for all three arrays, and band/mode selection (Ref. 20).

C. Multiband imaging photometer for Spitzer

MIPS (Ref. 20) (Fig. 27) provides diffraction-limited imaging photometry at 24, 70, and 160 μm and low-resolution ($R=15-25$) spectroscopy between 52 and 95 μm. To achieve sub-Nyquist sampling, there is a fine pixel scale option at 70 μm (the other arrays already have Nyquist-scale pixels). With precise subpixel sampling dither patterns, data processing allows "super resolution" imaging. A cryogenic scan mirror mechanism provides freeze-frame scan mapping, efficient dithering, and other instrument capabilities. The MIPS module and its optical train are shown in Figs. 28–30, and the spectral response curves of the 24, 70, and 160 μm channels and the spectral energy distribution (SED) mode are plotted in Fig. 31. Construction of the MIPS was led by the University of Arizona, with BATC as instrument subcontractor.

The MIPS 24 μm imaging band is built around a Boeing North America 128×128 Si:As BIB detector array developed under the leadership of the IRS team. This type of detector is relatively well behaved photometrically, and its

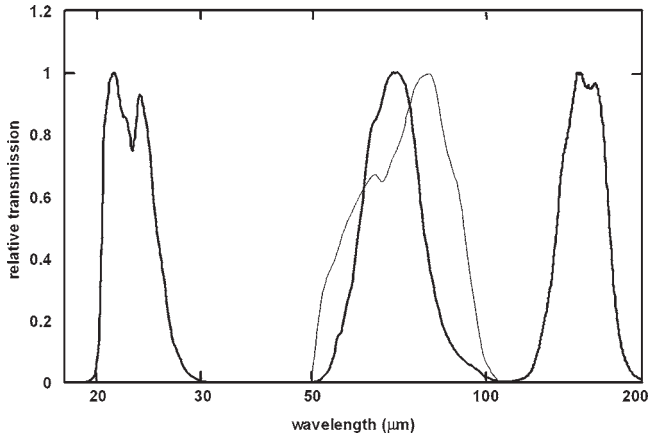

FIG. 31. MIPS spectral response curves for the 24,70, and 160 μm modules (dark lines) and the spectral energy distribution (SED) mode (light line) (Ref. 20).

properties are largely immune to the effects of cosmic radiation. These beneficial characteristics fundamentally arise from the detector architecture, in which the infrared-active layer is separated from the blocking layer so the latter can provide the high impedance required for low background performance, while the former produces the photocurrent that is sensed by the amplifier to provide an electronic signal. Many of these characteristics are made possible because the detectors are made of doped silicon, and their manufacture benefits from the technical infrastructure for manufacturing integrated circuits in this material. In addition, the intrinsic properties of silicon are critical, including its robust oxide, high stability, and ability to be doped with excellent impurity control. Thus, these detectors can be used effectively in a conventional staring mode.

The longer-wavelength bands at 70 and 160 μm must be based on germanium because there are no silicon dopants with sufficiently shallow energy levels to be useful for detecting such low-energy photons. There is no established infrastructure for high-quality germanium device manufacture. In fact, the MIPS arrays were built at the University of Arizona, using detector material provided by Lawrence Berkeley National Laboratories.[41–43] In addition, germanium does not have many of the intrinsic advantages listed for silicon. Thus, the detectors are built around a simpler technology, termed "bulk photoconductors." In such devices, contacts are put on opposite sides of a roughly cubical detector volume, and both the electrical and absorptive properties of the detector are controlled by this uniform slab of material. The intermingling of requirements on this slab results in many shortcomings in detector performance. For example, because each detector is a small capacitor with a long time constant, "dielectric relaxation" can lead to a slow component of response to a photon signal. Space charge effects within this volume and high fields near the contacts can influence the detector behavior, as can changes in compensation resulting from temporary energy states associated with cosmic radiation damage. As a result, these devices are unstable in response and have a memory of signals for many seconds or even minutes. The design of MIPS is largely dictated by the demands of the long-wavelength detectors. The scan mirror allows rapid (every ~10 s) motion of a source on the detectors so that the resulting signal is minimally affected by the slow response component. The optical train allows periodic (every ~120 s) flashing of calibration stimulators giving the data pipeline a series of signals to track the detector response. Data taking requires many independent observations so that aberrant signals can be identified and rejected from the science analysis.

The MIPS design was subject to the same guidelines for simplicity and low cost as all elements of the Spitzer program. The basic instrument layout is shown in Fig. 28. The optical bench is aluminum and the optics are diamond-turned aluminum mirrors. All the mirrors have spherical (or flat) figures. The scan mirror is the only moving part. Despite their complex appearance in Fig. 28, the optical trains are simple in concept. The pickoff mirrors receive the light in the telescope focal plane, one for 70 μm and the other for 24 and 160 μm. They relay the light to "field" mirrors at the back of the instrument that form a pupil on the scan mirror facets. The primary baffle for the instrument is around these facets. For the 70 μm arm, light leaving the scan mirror is focused by a single mirror onto the detector array at a suitable scale to provide a 5′ field of view and pixels with projected sizes of 9.8″. Tilting the scan mirror puts the light into a second optical train, where a mirror directs it onto the array at a magnified scale to provide projected pixels of 4.9″. Tilting in the opposite direction puts the light into a low-resolution spectrometer optical train. The depth of focus is so large that these three optical trains can feed the array from slightly different directions without interfering and can at the same time produce diffraction-limited images. Light from the other facet is relayed to a second focal plane after leaving the scan mirror, where it is separated into the 24 and 160 μm optical trains. Each of these trains brings the light at a suitable pixel scale onto its array (6″ for 24 μm and 18″ for 160 μm). There are no alternative scales or other options in the 24 and 160 μm optical trains. Figure 28 also shows some of the calibration stimulators used to track the long wave detector performance. Heim[44] has described the instrument in more detail.

The cryogenic scan mirror mechanism is based on a design developed for the Infrared Space Observatory (ISO) instruments[45] and provided to us by DeGraauw. It provides a single axis of motion over a throw of 14° and with a stability of better than 20″.[46] The original design was modified to reduce power dissipation and remove the possibility of local "hot" spots (i.e., warmer than 6 K) emitting and raising the background level seen by the 160 μm detectors. The linear motor windings are made of copper wire but with superconducting threads embedded within them, so the device can operate at room temperature but also operates at liquid helium temperature with essentially no motor power dissipation. The position sensors are differential impedance transformers, wound with high purity copper to minimize power dissipation.[47]

MIPS has four operating modes.[20] In "scan map" mode, the telescope is tracked at a constant rate, and the scan mirror is moved in a sawtooth wave form that freezes the motion on the detector arrays for an exposure and then jumps forward while the arrays are reset to freeze a shifted field on the array for the next exposure. For this mode, not only are spacecraft accelerations minimized, but all three arrays view the sky simultaneously. Consequently, this mode supports very efficient three-color mapping of large areas. In "photometry" mode, various combinations of scan mirror and spacecraft motions move a source image to a number of fixed points on one of the arrays. Integrations are taken at each position and the results are combined to provide an accurate measure of the source brightness. This mode is conducted one array, and hence, one band at a time. The SED mode applies only to the 70 μm array. The scan mirror is offset to put the light from the source through the spectrometer optical train and is then chopped to modulate the signal on and off the reflective spectrometer slit. The nominal spectral resolution is 2 μm/pixel, and the slit width corresponds to 2 pixels. Finally, in the "total power" mode, the scan mirror is used so a detector array alternately views the sky and a dark part of the

FIG. 32. (Color) Spitzer during installation on the rocket at Kennedy Space Flight Center. The left hand picture shows the radiative side of the observatory and the right hand picture shows the Sunward side with the observatory mounted in the nose cone of the Delta rocket. Michael Werner is shown for scale. Courtesy of NASA/JPL-Caltech.

interior of the instrument, enabling measurement of absolute sky levels. For all the modes, the observation templates are designed to provide a large number ($\sim$10) of independent measurements with the source dithered on the array. The high level of redundancy contributes to the overall reliability and accuracy of the final measurements. Because of the demands of the far-infrared arrays, the MIPS data analysis tool needs to be considered part of the instrument. The data analysis tool was developed at the University of Arizona, based on a combination of flight data and laboratory measurements of similar detector arrays. It is described by Gordon *et al.*[48,49]

The on-orbit performance of the instrument is generally in agreement with prelaunch expectations formed from the design and from testing (see Refs. 20 and 50). All the optics trains are diffraction limited. All the observing modes work well. The scan mirror moves and settles quickly (in less than a second) and is stable enough that it does not degrade the diffraction-limited imaging. The 24 μm array provides photometry with $<$1% nonrepeatability and has read noise ($\sim$40 e rms), quantum efficiency ($\sim$60% at the peak), and overall sensitivity in close agreement with prelaunch models. The 70 μm channel is three to four times less sensitive than anticipated. Much of the shortfall arises because of an unexpectedly high cosmic ray hit rate on the array (roughly 1 hit per 11 s). The hits seem to result from showering near or within the instrument, since many hits occur simultaneously on widely separated pixels. However, the photometric repeatability with this array is within 5%,[48] verifying the effectiveness of the measures taken to tame its poor behavior. The 160 μm array also suffers a loss of sensitivity due to the high cosmic ray hit rate, and its optical train lets a small amount of unwanted near-infrared light onto the array, compromising measurements of stars with Rayleigh-Jeans SEDs. Otherwise, the array operates as expected and also shows good photometric behavior. MIPS is returning unprecedented data on the fundamental properties of brown dwarfs, on debris disks (where it is the prime discovery instrument on Spitzer), on active galactic nuclei, and on the properties of star forming galaxies in the early universe, from redshifts of $z\sim3$ to the present ($z=0$).

FIG. 33. (Color) The launch of the Spitzer Space Telescope from Kennedy Space Flight Center on 2003 August 25 UT. NASA image.

V. LAUNCH, IN-ORBIT CHECKOUT, AND OPERATIONS

Figure 32 shows the spacecraft at Kennedy Space Flight Center during preparation for launch and Fig. 33 shows the Delta 7920H rocket lifting Spitzer into orbit. Spitzer was inserted into a heliocentric, Earth-trailing orbit (Fig. 1) in which it drops behind the Earth at a rate of about 0.12 AU yr^{-1}. As viewed from the Earth, the observatory executes small retrograde loops on roughly a year time scale as Spitzer comes to perihelion (Fig. 34). The result of this orbit is that Spitzer's operational pointing zone (OPZ) is a 35° annulus (see Fig. 35) that sweeps the sky twice during a "Spitzer year." The OPZ is defined by the constraint that the angle between the telescope boresight and the direction to the Sun may never be $\leqslant$82.5° or $\geqslant$120°. Objects such as the Earth, Moon, and bright planets are normally avoided to prevent degradation of observations by direct exposure or stray light. Mercury and Venus, as well as comets near perihelion passage, are precluded from the OPZ. The OPZ is also constrained by the necessity to restrict the roll angle of Spitzer to ±2° about the boresight axis to maintain optimum positioning of the Sun shade and solar panels relative to the Sun.

VI. IN-ORBIT PERFORMANCE

Spitzer and its SIs require the unique low-thermal environment of space in order to function properly; the environ-

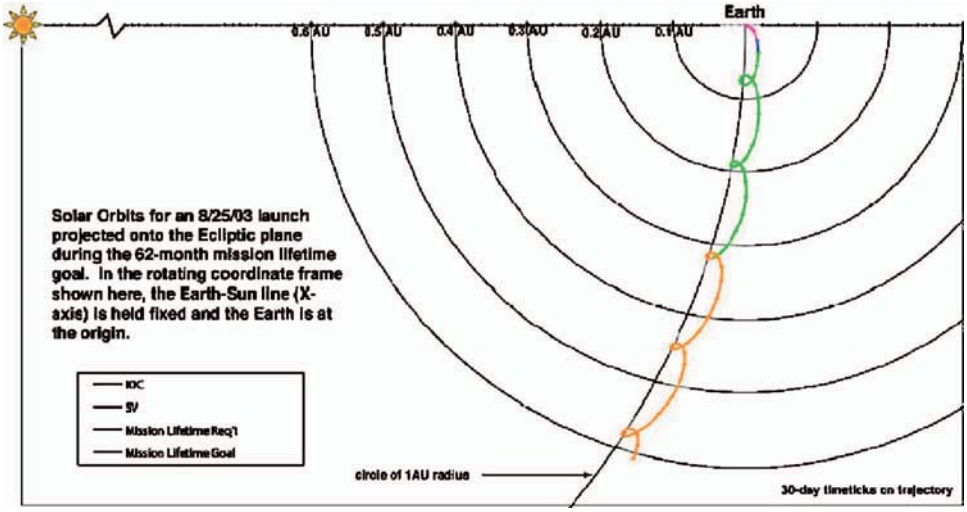

FIG. 34. (Color) Spitzer's solar orbit projected onto the ecliptic plane and viewed from the ecliptic North Pole. In the rotating frame, the Earth is at the origin and the Earth-Sun line is defined as the *X* axis. Loops and kinks in the trajectory occur at approximately one year intervals when Spitzer is at perihelion. Spitzer's orbit is also slightly inclined with respect to the ecliptic.

ment both permits the necessary radiative cooling and provides the low backgrounds to allow the SIs to achieve their high sensitivities. This environment was impossible to simulate on the ground, causing uncertainty about how well the observatory would perform in orbit. In general, the in-orbit performance of Spitzer is at least as good as or better than predicted. The principal in-orbit performance characteristics of the observatory and the SIs are described below.

A. Cryogenic lifetime

The cryogenic lifetime is the parameter most critical to the success of the Spitzer mission. Therefore, the Spitzer team has worked very hard to understand and extend this lifetime. A central parameter for the cryogenic lifetime is the CTA OS temperature, which controls the amount of parasitic heat that finds its way into the cryogen tank. Spitzer's design includes shields and coatings designed to prevent heat from either the solar panel or the spacecraft from reaching the OS and to reject by radiation from the back of the OS any heat that reaches it. This system works very well, and the OS has reached a temperature of 34 K entirely passively.

The parasitic heat load to the cryogen tank is thus only ~1 mW, considerably smaller than the instrument heat loads, which lie between 2 mW for IRS and 3 mW for IRAC. Because the telescope is cooled by the helium vapor generated by the power dissipated in the cryogen tank, the telescope temperature depends on the instrument in use. For IRAC and IRS, the resulting temperature is low enough that the telescope contributes negligible radiative background; for MIPS it is necessary to add additional power to the helium bath to drive the telescope down to the temperature of 5.6 K required for background-limited performance at 160 μm. This is done following a cryogen conservation scheme devised for Spitzer[51] making use of the facts that only one instrument is turned on at a time and that instruments are scheduled in campaigns of 1–3 weeks duration. Managing the telescope temperature in this way, together with a number of other refinements, has extended the expected cryogenic lifetime significantly. The mass of the helium remaining after launch and initial blowdown was about 43.4 kg two months after launch as measured by applying a heat pulse to the helium bath and noting the accompanying temperature rise. This measurement was repeated a year later to determine the rate of cryogen depletion; the results are consistent with mass estimates obtained by observing the CTA's response to the heat pulses that initiate the cooling of the telescope for MIPS (see Fig. 36). Our current best estimate is that the helium will be exhausted sometime between 1 April 2009 and 1 August 2009, almost six years after launch (see Fig. 37).

Following depletion of the helium, the telescope will warm up, but it will still be colder than the OS. Current estimates suggest that the temperature of the telescope and the MIC will be approximately 30 K. At this temperature, both the instrumental background and the detector dark cur-

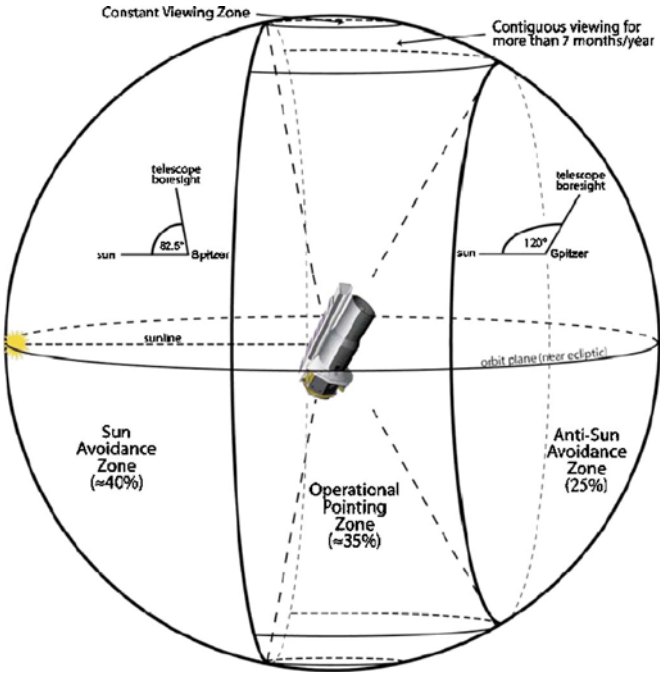

FIG. 35. The operational viewing zone annulus associated with the Spitzer solar orbit. (Ref. 40). If the telescope is pointed too close to the Sun, sunlight will fall onto the outer shield of the cryogenic telescope assembly. If the telescope is pointed too far away from the Sun, the solar panel generates insufficient electrical power. The percentages given indicate sky coverage.

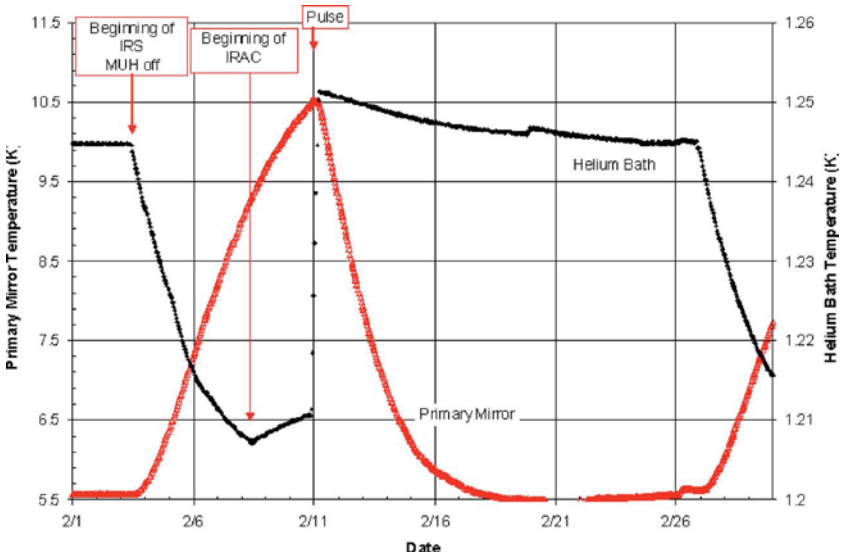

FIG. 36. Use of the makeup heater to lower telescope temperature during the MIPS campaigns. Telescope temperature (red line, left axis) and the helium bath temperature (solid blue lines, right axis) are shown. The telescope cools sharply in response to makeup heater pulses. A combined makeup heater and SI heat input to the bath of 5 mW is required to hold the cryogenic telescope at a temperature of ~5.5 K. Courtesy of Paul Finley/Ball Aerospace.

rent should be low enough for Spitzer to continue natural background-limited operations in the shortest-wavelength IRAC bands at 3.6 and 4.5 μm. Additional information on the measured on-orbit thermal and cryogenic performance of the Spitzer CTA can be found in Ref. 52.

B. In-orbit optical performance

In-orbit measurements[16] of the Spitzer telescope show that it provides diffraction-limited performance at wavelengths greater than 5.5 μm, which compares favorably with its level-one requirement of diffraction-limited performance at 6.5 μm. A focus campaign of two secondary movements was initiated once the telescope assembly had cooled to operating temperature[17] (see Fig. 15). After the completion of this campaign all of the science instruments were determined to be confocal with one another to within the depths of their focus.

C. Pointing performance

In general, the pointing performance of *Spitzer* is better than predicted prior to launch. The star tracker has proven to be very accurate, with a noise-equivalent angle of approximately 0.11″ using an average of 37 tracked stars. The cryomechanical variation in alignment over time between the star tracker mounted on the warm SCB and the cold telescope boresight has proven to be very small and easily calibrated, so that the star tracker can be used to directly point the telescope boresight to within 0.45″ (1σ radial). For offset movements less than 30′ the PCS meets the 0.4″ accuracy requirement. Once the telescope pointing has settled, it is stable to within 0.03″ (1σ radial) for times up to 600 s.

D. External torques and reaction control

Net angular momentum will build up on Spitzer from a combination of solar wind and radiation pressure and uncompensated helium venting. During the design of the observatory, care was taken to align the vector of solar radiation and wind pressure with the center of mass, and the two CTA helium vent nozzles were balanced as well as possible. This has resulted in very low momentum buildup and a low frequency (once or twice per week) of actuations of the RCS to remove angular momentum.

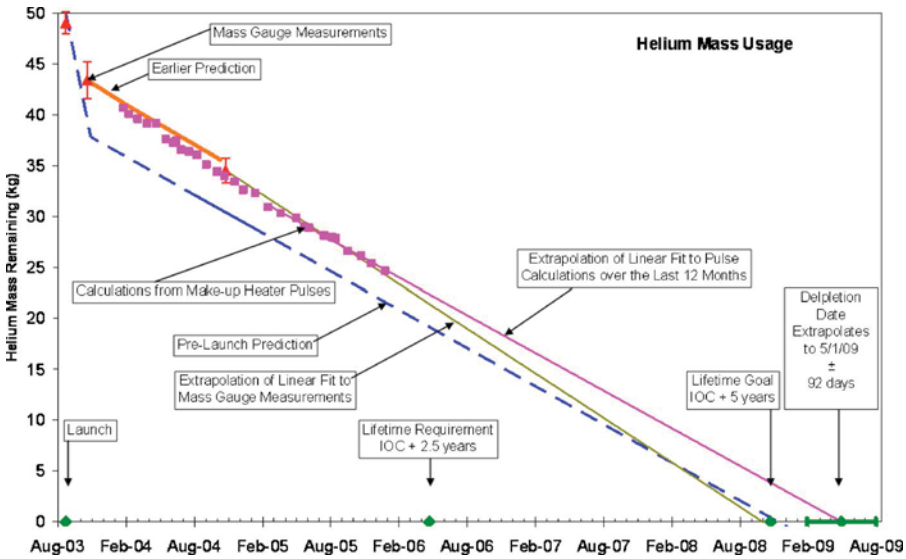

FIG. 37. Helium mass usage. The solid pink squares are mass measurements from makeup heater pulses. The solid green symbols along the x axis indicate significant milestones. The dashed line is the prelaunch predicted helium use. A linear extrapolation of recent mass measurements gives an end-of-life data of 1 June, 2009 with a 2-sigma uncertainty shown. Courtesy of Paul Finley/Ball Aerospace.

E. In-orbit operational efficiency

A number of factors allow Spitzer to achieve extremely high operational efficiency: The solar orbit has no eclipses or Earth occultations, and Spitzer has access to ~35% of the sky at any time, which facilitates efficient scheduling. The scheduling strategy of single instrument campaigns of several weeks' duration minimizes time lost due to instrument changeovers. The very high thermal-mechanical stability resulting from the combination of the solar orbit and the robust system design has allowed us to spend much less time in spacecraft/PCS calibrations than anticipated. The restriction of each instrument to at most a handful of operating modes minimizes the amount of time spent calibrating. Very little time has been lost to safe-mode events, and the DSN captures well over 98% of the stored data. As one measure of the in-orbit efficiency we have adopted a metric f, the fraction of wall clock time not spent on downlinks, spacecraft calibrations, and unscheduled gaps. In recent months, we have typically achieved $f \sim 0.9$, or 90% efficiency by this metric. Though other metrics could be defined and perhaps even preferred, Spitzer operates with remarkably high efficiency by any standard.

F. Instrument in-orbit performance

The in-orbit performance of the instruments is summarized in Table III. As stated in the footnote at the bottom of the table, more detailed information about the instrument performance can be obtained from the Spitzer Science Center (SSC) website. In terms of raw sensitivity, Spitzer provides a factor of ~10–~1000 gain over the capabilities of ground-based telescopes and previous space missions, including the European Space Agency's (ESA's) very successful ISO mission.[53] This sensitivity gain is per spatial or spectral resolution element; at most wavelengths Spitzer provides an additional ~100–~1000 gain from the large pixel count of the imaging and spectroscopic arrays. These two factors combine to enable Spitzer to carry out unprecedented investigations in the infrared, as illustrated below. For some applications, Spitzer's performance is limited by other considerations than the raw instrumental sensitivity. Foremost among these effects is noise due to source confusion that is produced by fluctuations in the number of faint sources that lie individually undetected within the beam of the telescope. Confusion noise decreases as the telescope size increases and the spatial resolution improves, but this effect limits the sensitivity achievable with the relatively small Spitzer telescope. Confusion due to unresolved galaxies starts to limit observations in IRAC bands 1 and 2 (3.6 and 4.5 μm) in about 2000 s,[37] although longer observations of isolated targets have been carried out successfully.[38] Confusion is a greater problem for the MIPS 70 and 160 μm bands because of the larger beams dictated by diffraction at these longer wavelengths.[54] However, Dole *et al.*[55] have recently succeeded, using a very clever technique that relies on stacking apparent 70 and 160 μm noise frames at the positions of known 24 μm sources, in reaching far beyond the formal confusion limit at these wavelengths and identifying the source populations responsible for most of the infrared background at these wavelengths.

Apart from the effects of confusion, the performance of Spitzer's SIs has tracked prelaunch predictions fairly well. The sensitivity at 70 and 160 μm falls somewhat below prelaunch predictions, probably due to unanticipated effects of cosmic ray secondaries, and half of the 70 μm array was lost due to a short in the cabling within the cryostat that occurred during the on-orbit cooldown. In addition, observations of bright stars at 160 μm are compromised by a short-wavelength leak that allows photons in the intrinsic Ge absorption band shortward of 2 μm to reach the detectors. On the other hand, the MIPS 24 μm array, in particular, but also the IRAC short-wavelength bands and the IRS peak-up imaging band at ~16 μm, are achieving higher than predicted sensitivity. In addition to their exquisite sensitivity, the instruments have proven to be very robust. Their reliability and the simplicity resulting from the limited number of observing modes available to each have contributed to the high on-orbit efficiency achieved by Spitzer.

VII. OPERATIONS

A brief summary of the operational characteristics of the Spitzer observatory is available to the interested user on the Spitzer Pocket Guide (see Fig. 10). Spitzer's operations are strongly influenced by its unique heliocentric orbit and by the requirement for very efficient operations. In its first year Spitzer executed ~5500 h of astronomical observations, with another ~1500 h being spent in observatory and instrument calibration observations. In the second year of operations, Spitzer executed ~6500 h of astronomical observations, with about 1200 h devoted to calibration observations. As of the writing of this article, for more than 6 months Spitzer has been executing science observations and calibrations (and the slews to celestial targets) for more than 90% of the wall clock time of the observatory. This more than meets the objective set out before launch. The time not used for science or instrument calibration observations is used for communications with the ground, spacecraft calibrations, and unavoidable gaps between observations. During nominal science operations, Spitzer collects data autonomously based on a weeklong sequence of commands transmitted to the observatory (uplinked) once per week. Spitzer stores the data in its mass memory and transmits data once or twice per day (downlinks) depending upon how much data are collected during that time period. The fact that only one science instrument can be operated at a time is a further constraint on science operations.

Operations during the initial checkout and verification of the observatory were complicated by the warm-launch architecture; the telescope was at ambient temperature at launch and cooled to the operating temperature of 5.5 K over a period of about a month and a half. In this section we describe the operational characteristics of the Spitzer observatory, the observation strategy, and the ground data flow.

A. Launch and operations during initial in-orbit checkout and scientific verification

Spitzer was launched into an Earth-trailing solar orbit from the Cape Canaveral Air Force base at 1:31:39 EDT (05:35:39.231 UTC) on 2003 August 25. The heliocentric orbit is nearly the same as that of the Earth, but viewed from the Earth, Spitzer recedes at a rate of 0.12 AU yr^{-1} (see Fig. 34).

After launch, a carefully planned series of events occurred that initially verified the spacecraft functions, and then began activating the SIs aboard Spitzer. Four days after launch, the telescope dust cover was ejected to allow the telescope to view the sky. One day later the aperture door to the MIC within the cryostat was opened by activating the ADM. These two mechanical deployments were the only activations necessary to bring the observatory into its operational configuration. The timing of these events was determined by the outgassing of the observatory to ensure that minimal contamination was deposited on the sensitive reflective and emissive observatory surfaces. It was necessary to allow the telescope system to cool before the instruments could collect useful data. The cooling of the telescope was initially achieved predominantly by radiation coupling to space; about 23 days after launch, supplemental heat was dissipated in the cryostat using the makeup heater causing additional cold helium gas from the cryostat to boil off and vent through the telescope, accelerating its cooldown. The process of Spitzer verification and telescope cooling dominated the first 40 days of the 62 day IOC period.

As the telescope cooled, the instruments were activated, beginning with the shortest wavelengths (IRAC), then the spectrometer (IRS), and ending with the longest wavelengths (MIPS). The instrument activation and characterization consumed the later half of IOC. Major activities of IOC were focusing the telescope, assessing instrument performance, determining the observatory reference frame and pointing performance, and determining the CTA's cryogenic performance and thus the projected cryogenic lifetime of the observatory. The prelaunch plans called for IOC to last 60 days. In fact, the activities of this period were completed on day 62 after launch. At that time the observatory began a 30 day period of science verification (SV) activities. During the science verification phase, the emphasis was on further characterizing instrument performance and obtaining a series of early-release observations that were intended to demonstrate to the science community and the public the power of NASA's last Great Observatory. The observatory began nominal operations on 1 December 2003, 98 days after launch. This was remarkably close to the prelaunch schedule, particularly since the observatory was in safe mode for ~7 days of the IOC/SV period. Observatory SI operations were suspended during October 28–31, 2003 as a result of the effects of the largest solar flare of the last 25 years.

B. Pointing constraints, operational pointing zone, and target visibility windows

Spitzer has two health and safety-driven constraints on where it can point at any given time, both relative to the Sun (Fig. 35). The first is that the solar panels must be oriented roughly perpendicular to the Sun (boresight no greater than 120° away from the Sun) to generate enough power to operate the observatory. The second is the Sun-avoidance zone that prevents solar radiation from traveling down the barrel of the telescope (boresight no closer than 82.5° from the Sun). As shown in Fig. 35, this limits Spitzer pointing to an annulus that occupies about 35% of the sky at any given moment. This annulus sweeps the entire sky during a year such that each region of sky near the ecliptic plane is visible for a limited period (~40 days) twice each year.

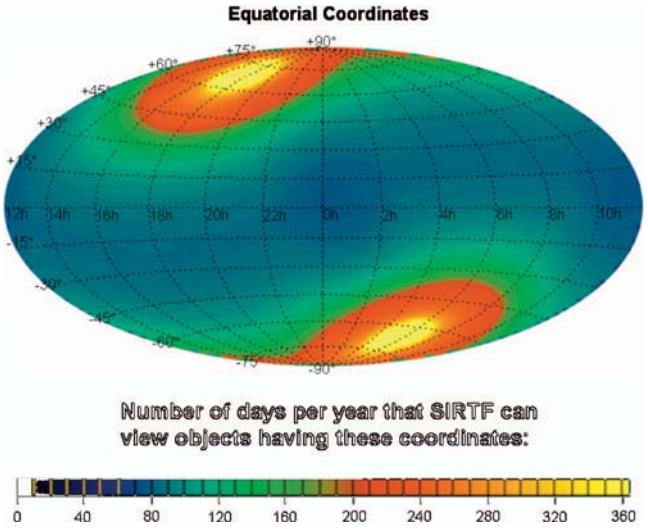

FIG. 38. (Color) Total annual days of target visibility as a function of right ascension and declination (Ref. 40). The minimum visibility window for any point on the sky is about 40 days.

Spitzer must also maintain the solar panels within 2° of perpendicular to the Sun (in the telescope roll direction). This limited freedom in roll angle is used only to stabilize the position angle of the telescope during long observations. This means that the position angle of the telescope focal plane relative to ecliptic north is fixed for a given date of observation, and objects at low ecliptic latitude have a very limited range in position angle. On the other hand, targets within about 30° of the ecliptic pole are continuously in view and have a full range of available position angles. Figure 38 shows target visibility as a function of equatorial coordinates. In addition to the hard pointing constraints, pointing at certain bright solar system objects is avoided by default. Pointing within 7° of the Earth-Moon system is avoided, as is pointing within 30′ of a list of bright objects that includes Mars, Jupiter, Saturn, Uranus, Neptune, Vesta, Ceres, Iris, and Eunomia. An observer can choose to turn off the bright object avoidance and observe, for example, the moons of Jupiter. It is up to the observer to design an observation that is robust when pointing at or close to a bright object. Bright objects whose positions are fixed on the celestial sphere are not omitted from the visibility windows.

Moving bright-object avoidance is implemented via the visibility windows assigned to each target. The visibility windows are the collection of data-time ranges during which the entire field being observed is within the OPZ. The visibility windows are trimmed to avoid periods during which the listed bright objects fall into the field. Target visibility

windows are further trimmed to produce plan windows that take into account observer-specified constraints such as refined timing or ordering requirements and also the schedule for which instrument will be operating at what time. Each continuous period of science instrument operation is called a campaign, and each campaign is typically 1–3 weeks in length.

C. Operational overview

There are two rhythms that punctuate Spitzer's routine: the one-week length of each master sequence controlling observatory operations and the 12–24 h spacing between scheduled telecommunications with the ground. During the first year of science operations, contact with the DSN was scheduled twice per day for ~1 h periods. During a contact opportunity, recorded science data and engineering telemetry are downlinked and passed to various teams for processing and analysis, commands that delete data previously received by the ground are uplinked, real-time telemetry is evaluated, any indication of a problem is assessed, and action is taken if so dictated. In addition, the uplinking of the next weeklong master sequence and its supporting command files is accomplished over one or more DSN contacts prior to the expiration of the previous master sequence. During nominal operations, the development of the command sequences is a cooperative task among the science operations team, the mission operations teams, and the observatory engineering team. The scheduling of science, science instrument engineering, and routine Spitzer engineering activities is done at the SSC as is the scheduling of which instrument is going to be operating at what time. The detailed command products for the science instrument activities and observations are also produced at the SSC, as is the master sequence that will control the observatory. The mission operations team merges the SSC products with any needed Spitzer engineering activity commands and puts the command products into a format that can be uplinked to the observatory by the DSN. All teams review the products before the mission manager grants approval to uplink the products. The 5 week process for sequence development includes an opportunity to revise the sequence after the initial review and processing in if problems are discovered.

During normal operations, stored science data are downlinked to the DSN and transferred to JPL where they go through several stages of processing. The data are delivered to the SSC as raw array data in flexible image transport system[56] (FITS) format, a standard astronomical image format.

D. *Spitzer* operations and the impact on the *Spitzer* cryogenic lifetime

Spitzer's cryogenic lifetime is determined by the rate at which the superfluid helium in the cryostat boils off. The heat dissipated into the cryostat, and hence the boiloff rate, is dominated by the SIs themselves plus any additional heat put into the cryostat by the makeup heater used to adjust the telescope temperature. This makeup heater is necessary because none of the three SIs dissipates enough power to create sufficient boiloff to keep the telescope at the low temperature required for background-limited observations by MIPS at 70 or 160 μm. During the initial part of the mission, the telescope was kept continuously at 5.6 K, the temperature required for MIPS 160 μm observations. Early in nominal science operations the Spitzer team began to allow the telescope temperature to float upward towards 10–12 K during IRS and IRAC campaigns, with a pulse of makeup heater power issued about one week in advance of each MIPS campaign to bring the telescope temperature back down to 5.6 K and a steady-state makeup heater value used to hold that temperature steady during the campaign. This innovation saves about 13 days worth of cryogen per year. Beginning around June 2006, MIPS operations will be divided into campaigns that are allowed to be at ~8.5 K and include only observations that do not require high-quality 160 μm data, and cold campaigns at 5.6 K that can include observations requiring high quality data at the longest MIPS wavelengths. This is expected to extend the cryogenic lifetime of Spitzer by 1–2 months.

E. Spitzer Science Center operations and data products

The SSC acts as the main interface between the Spitzer project and its user community: observers, archival researchers, theorists, and the astronomical community at large. The SSC handles observatory planning and scheduling, data processing and archiving, and direct observer support as well as software development activities to support all of the SSC's functions. The SSC also provides public and educational outreach on the Spitzer mission for NASA.

The SSC is charged with operating the Spitzer science mission, including gathering, organizing, and carrying out the observing program efficiently while safeguarding the observatory. The SSC is responsible for creating and securing the scientific legacy of Spitzer in the form of a uniformly and reliably reduced, calibrated, and readily accessible archive of all Spitzer science and supporting science instrument engineering data. The SSC is also responsible, during the operations phase, for providing the necessary funding to the researchers who use Spitzer. A simple way to visualize the functions performed by the SSC is to consider the flow of data beginning with proposals from the science community to utilize the Spitzer observatory, and ending with delivery of the processed data to the users. This flow is shown in Fig. 39. This section presents the details of planning and scheduling the observatory, processing and distributing the science data, and supporting proposers and observers.

1. Observatory long range planning and scheduling

Each time new observations are submitted to the SSC (see Sec. VII F for a description of the proposal process), they are incorporated into the Science Operations Database (SODB). Observations are fully described at the time of submission and are in the form of a set of parameters that can be used by software at the SSC to expand the observation into the series of commands to the Spitzer and SIs that will execute the observation. This fully described observation is called an astronomical observation request (AOR) and is the

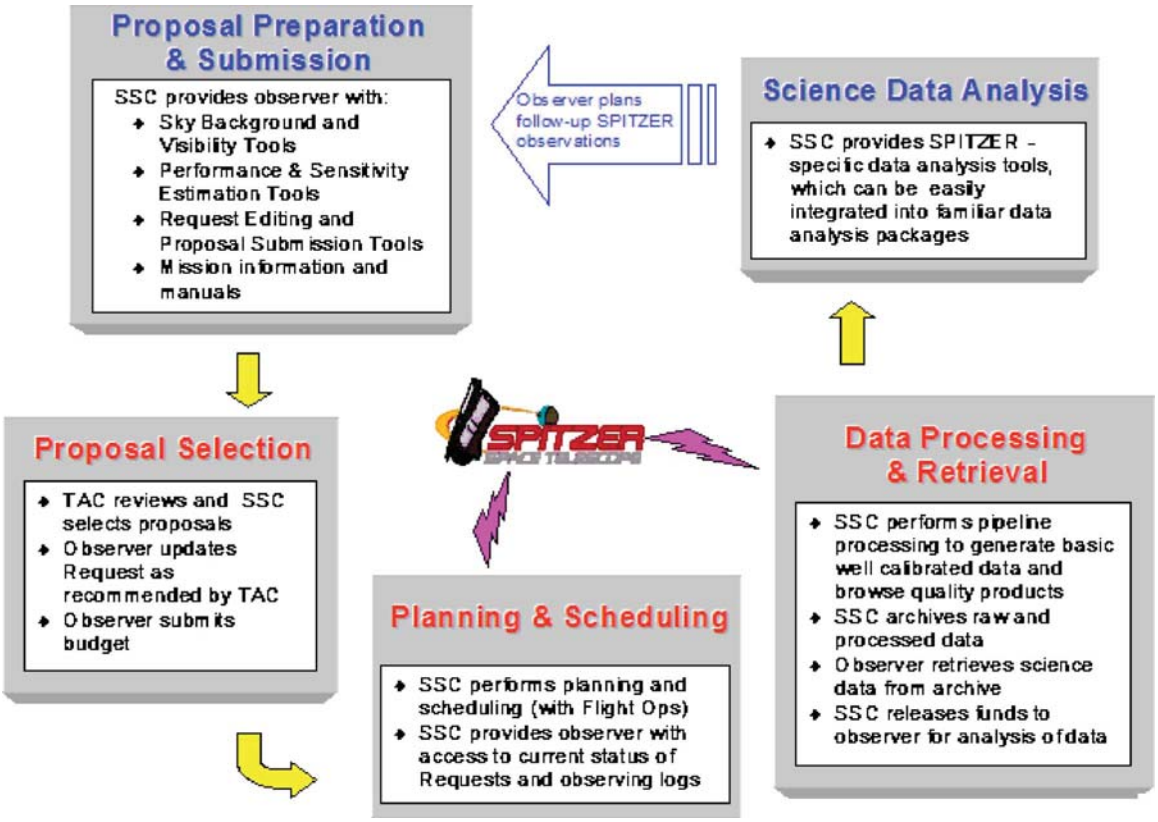

FIG. 39. Flow diagram showing community, Spitzer Science Center, and Spitzer relationships. Courtesy of SSC/Caltech.

fundamental unit used in the planning and scheduling process. The duration of each AOR is limited to allow for periodic calibration and maintenance operations. Analogs to the AOR exist for both spacecraft and SI engineering and are handled the same way by the scheduling system. Observers may introduce constraints on the AORs within their observing program; for example, a large map consisting of many AORs may need to be completed within a specified time frame so that the separate observations align properly. Because such constraints introduce substantial complexity into scheduling the observatory, they are used sparingly and only with compelling scientific justification. When the observations from each proposal cycle (approximately one year in duration) are incorporated into the SODB, the observatory planning and scheduling team, along with the observer support team, performs an analysis of the database contents and constructs a plan for when each SI will be operating during the upcoming cycle. This base line instrument campaign plan (BICP) takes into account the fraction of total observing time proposed on that instrument, the fact that longer campaigns improve cryogen conservation, the existence of large, heavily constrained observing programs, a preferred instrument operation order for cryogen conservation and the fact that some parts of the sky are only visible for 40 days at a time. The preferred ordering of instruments is IRAC:MIPS:IRS, and in the second year of science operations the campaign plan was built around a pattern of 11 days of IRAC followed by 14 days of MIPS followed by 13 days of IRS. However, the BICP is often modified prior to the schedule being built for a given week in order to accommodate unanticipated constraints.

After the BICP is built, each request in the database is assigned a plan window taking into account constraints, the campaign plan, and target visibility. The actual observing schedules are constructed for one week at a time beginning about five weeks in advance of the time the first request in that schedule begins execution on board the observatory. The scheduling process begins by identifying the pool of all available observations with windows in the target week and by collecting and scheduling the SI and spacecraft engineering activities. This process uses both manual and automated procedures. Large, heavily constrained observing programs may also be scheduled manually. The remainder of the timeline is filled in with observations honoring constraints and attempting to minimize the slew path from target to target and maximize overall observing efficiency. After an approval process, the weeklong schedule is delivered to the mission sequence team at JPL for processing, review, and possible change in response to the review process.

Spitzer must also support targets of opportunity (ToO), which are observations of astronomical phenomena that are inherently transient and occur unpredictably, such as novae or gamma ray bursts. The observatory should be able to observe such a target within 48 h of approval of the observer's request to activate the observation. In the most stressing case, the observing sequence executing onboard the observatory must be interrupted and replaced with a new sequence containing observations with all three SIs in rapid sequence. Such a high impact ToO requires 24 h operations and cannot be supported often. Spitzer successfully executed a ToO ob-

servation of a Gamma Ray Burst event on 27 May 2005, two days after the burst was discovered by NASA's SWIFT satellite.

2. Pipeline operations, data quality assessment, and archiving

The raw science data are delivered to the SSC in FITS format. The raw data files are automatically registered in the SODB and run through pipelines that produce two levels of output products. The BCDs are individual frames of data, but they are calibrated and artifacts are removed. This is considered a very robust level of processing that an observer undertaking detailed data reduction would use as the basis for that reduction. In addition, the pipeline produces higher-level products combining all the BCDs in an AOR. These products include such things as mosaics produced from a mapping AOR or extracted spectra. After initial processing, data quality analysts flag any observations that have significant problems that would interfere with scientific interpretation of the data. The data are typically processed twice prior to being made available to the observer. The first processing, to obtain a quick assessment of the quality of the data, is done with a default calibration as soon as the data arrive at the SSC. The second processing is done at the end of the instrument campaign when all the calibration observations can be analyzed and applied to the entire campaign.

After final campaign processing, the data are placed in the Spitzer data archive and the observer is notified of the availability of the data. In general, observers have proprietary access to their data for one year after the processed data are placed in the archive. In some cases, notably the Spitzer Legacy projects, data are placed in the Spitzer archive with no proprietary period and the data are available immediately to any user of the Spitzer archive (see Sec. VII E).

3. Observer support: SPOT, LEOPARD, the SSC website, and the helpdesk

The SSC devotes numerous resources to observer support. The Spitzer astronomer's web site[57] contains many tools and documents aimed at hopeful proposers and successful observers. The SSC also maintains an email helpdesk. In addition to documents and observing schedules, the SSC distributes software packages for the development and submission of proposals and observations and for access to the Spitzer archive. The Spitzer planning observations tool (SPOT) and LEOPARD, the archive interface, are distributed together as the SPITZER PRIDE package and can be downloaded from the SSC website. These tools run on Windows, Solaris, Linux, and Mac OSX and are installed locally on the user's computer. They interface with additional software and the databases at the SSC. SPOT is a very powerful tool that enables the astronomer to fill out the astronomical observation templates that produce AORs, and allows the astronomer to visualize an AOR by overlaying it on several types of all-sky survey image data or on any other image that the astronomer has locally in FITS format. SPOT also provides target visibility and position angle information for a specified date and calculates accurate estimates of the observation duration based upon detailed command expansion done on the SSC server. LEOPARD provides a basic interface to the archive and allows for searching the reserved observations catalog (ROC) prior to submitting proposals in order to avoid duplications. All observers use LEOPARD to download their own Spitzer data. Data that are not proprietary can be downloaded by anyone using LEOPARD.

F. Mission strategy

Spitzer, as the infrared component of NASA's Great Observatories, was designed to be able to address many of the most compelling and vital problems of modern astrophysics. As such, it must be operated as a facility for the entire scientific community. The vast majority of the observing time is competed via proposals for this highly prized resource for astronomical research.

1. Guaranteed time observers

As part of NASA's commitment to reward the many decades of effort necessary to execute a major science mission, the Spitzer guaranteed time observers (GTOs) were awarded 20% of the time on the observatory during the first two and a half years of the mission to execute their science programs. The teams led by the three instrument principal investigators (PIs), Giovanni Fazio of SAO/Harvard-Smithsonian Center for Astrophysics, James Houck of Cornell, and George Rieke of the University of Arizona, were each awarded 5% of the observatory science observing time for the full cryogenic lifetime of the mission. In addition, the interdisciplinary scientists and other members of the Spitzer SWG were awarded a total of 5%. After two and a half years, the SI PIs continued to be awarded 5% of the time for the remainder of the mission, and the remaining GTOs were required to join one or more SI teams.

2. Legacy programs

It was recognized in the prelaunch planning of the Spitzer science program that the short lifetime of the mission required a different approach to create a coherent scientific archive that would provide a lasting scientific legacy well after the observations ended. To achieve this objective, the Spitzer Legacy program was created. This program reserved ~3000 h of Spitzer observing time, to be executed in the first year of the mission, for large projects that had the following attributes.

(1) They must be large coherent science investigations, not reproducible by any reasonable number or combination of smaller general observer programs.
(2) They must be programs whose scientific data, upon archiving, are of general and lasting importance to the broad community.
(3) All raw and pipeline-processed data must enter the public domain immediately, thereby enabling timely and effective opportunities for follow-on observations and for archival research, with both Spitzer and with other observatories.

The selected teams were funded to execute their science projects and to deliver (though the SSC) images, catalogs, and atlases of processed Spitzer data that were in forms

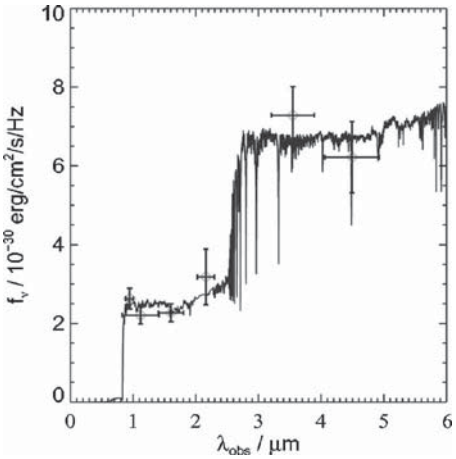

FIG. 40. Hubble Space Telescope and Spitzer observations of a galaxy at $z=5.8$. Model fit to data is a galaxy with mass ~20% that of the Milky Way which formed at $z\sim10$. This figure is adapted from Eyles *et al.* (Ref. 83).

ready for immediate use by the astronomical community. Projects were selected in 2000 from submitted proposals and are described as follows: GLIMPSE: galactic legacy infrared midplane survey extraordinaire, PI—Ed Churchwell (University of Wisconsin); C2D: from molecular cores to planet-forming disks, PI—Neal Evans II (University of Texas); FEPS: the formation and evolution of planetary systems: placing our solar system in context, PI—Michael Meyer (University of Arizona); SINGS: the spitzer infrared nearby galaxies survey—physics of the star-forming ISM and galaxy evolution, PI—Robert Kennicutt, Jr. (University of Arizona/Cambridge University); SWIRE: the Spitzer wide-area infrared extragalactic survey, PI—Carol Lonsdale (infrared processing and Analysis Center, California Institute of Technology); and GOODS: Great Observatories Origins deep survey, PI—Mark Dickinson (National Optical Astronomy Observatory).

Following the successful paradigm of the Legacy program, the Spitzer SSC has continued to select Legacy-style projects in the successive competitions for observing time that occur on an annual basis.

3. First look survey

It was recognized well before launch that the depths to which Spitzer could probe in the infrared were many orders of magnitude deeper than any prior observatory. It was decided that for the science community to make sensible use of the observatory, particularly in the first year of the mission, some guiding observations that probed the nature of the sky at the depths reachable by Spitzer should be executed on behalf of the science community. These observations, known as the first look survey, used ~100 h of observing time taken from the pool of director's discretionary time (DDT) (see below). These observations were the first to be scheduled on the observatory, and were executed in the time frame of December 2003–January 2004. The initial processed data were released in mid-January 2004 in order to support the initial general observers call for proposals. The observations, imaging at moderate depths using the IRAC and MIPS imaging instruments, covered regions of the sky to sample extragalactic, galactic, and solar system science objectives.

4. General observers and director's discretionary time

The vast majority of the available observing time on the Spitzer Space Telescope is devoted to General Observer programs. The successful projects are selected through an annual proposal solicitation process. The call for proposals is released in November, with proposals due in mid-February of the following year. The proposals are reviewed by panels, and a time allocation committee recommends the successful program to the SSC Director for selection. The proposal review is held in mid-late April of each year, with the successful projects beginning execution in June of that year.

In the first 2.5 years of normal science operation ~75% of the available time was allocated to General Observer (including the initial Legacy) projects. After the first 2.5 years, the fraction of observing time devoted to General Observer projects rose to 80%. Within this pool of observing time Spitzer executes individual investigations that follow the normal conventions for NASA Great Observatory missions, i.e., the investigator has a 1 year proprietary period for use of the calibrated, pipeline-processed data (see Sec. VII E 2). For Legacy projects (Sec. VII F 2) the proprietary period is waived.

5% of the observatory time is available for use as director's discretionary time. This pool has various uses, such as rescheduling observations that were not successfully executed through no fault of the observer (e.g., because of a solar storm, where the observatory performance is substantially degraded) and executing scientifically crucial and time critical observations that were not preapproved in the annual proposal process. In addition, the SSC Director allocates 50 h/year from the DDT pool to Spitzer fellows as part of their research program. The Spitzer first look survey was executed under the auspices of DDT.

G. User interfaces

The SPITZER PRIDE software package is available to Spitzer observers and archive users for planning observations, submitting proposals, and downloading data. The package may be downloaded at http://ssc.spitzer.caltech.edu/propkit/spot/. Versions are available for the Windows, OSX, Solaris, and Linux operating systems, and automatic updates are available for most users.

VIII. SCIENTIFIC RESULTS

Even at this early stage there are many more results in hand from Spitzer than can be discussed in this review. The initial results from the mission appeared in a dedicated special issue of the *Astrophysical Journal Supplement*.[58] Werner *et al.*[59] have prepared a review of the first two years of Spitzer galactic and solar system science to appear in Volume 44 of the *Annual Review of Astronomy and Physics*. Additional early mission Spitzer science results appear in the proceedings of the first two Spitzer science conferences, "New Views of the Cosmos"[61] and "Infrared Diagnostics of Galaxy Evolution,"[62] to appear in the Astronomical Society of the

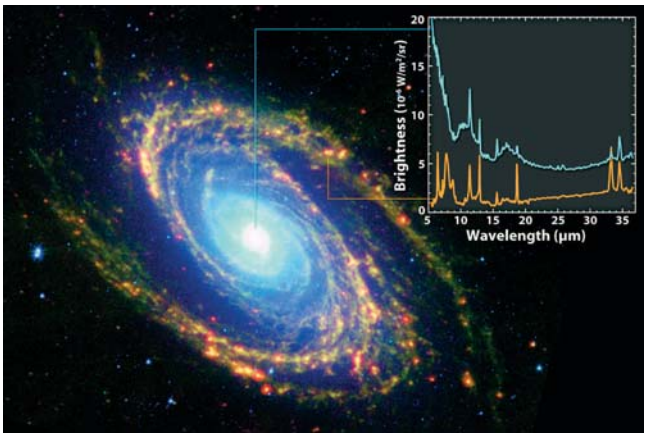

FIG. 41. (and cover). (Color) Composite mosaic image of M81 obtained with Spitzer's MIPS and IRAC cameras (blue=3.6 μm, green=8.0 μm, red=24 μm). It is evident that the bulge is dominated by the light of old stars and the disk by thermal infrared radiation from regions of star formation. Spitzer IRS spectra are shown for the nucleus (blue line) and an HII region in the disk (orange line). The spectra show prominent atomic fine-structure lines ([Ne II]12.81 μm, [Ne III]15.56 μm, [S III]18.71 μm, [S III]33.48 μm, [Si II]34.82 μm) and PAH emission features at 6.2, 7.7, 8.6, 11.3, 12.7, and 17 μm. In addition, the nuclear spectrum shows a strong stellar photospheric contribution shortward of 8 μm, and silicate emission at 10 μm. Image courtesy of NASA/JPL-Caltech/K. Gordon (University of Arizona)/S. Willner (Harvard-Smithsonian Center for Astrophysics). Spectra courtesy of R. Kennicutt and the SINGS (Ref. 69) legacy team. Graphics by Robert Hurt (JPL-Caltech).

Pacific Conference Series. The SSC maintains an archive[63] of particularly newsworthy Spitzer images, data, and scientific results that have been released for public affairs purposes. We present below a few striking examples of the type of data that Spitzer is returning to the international scientific community.

A. Extragalactic astronomy

1. The most distant galaxies in the early universe

Infrared radiation provides a natural probe of the distant and early universe, as the expansion of the universe shifts optical and even ultraviolet starlight from distant galaxies into the infrared. The sensitivity and image quality of Spitzer have permitted detection of galaxies as distant as redshift ~ 7,[60] which means that the light we observe now left the galaxy when the universe was only one-eighth of its present size and about 6% of its present age. This is illustrated in Fig. 40, which shows Hubble Space Telescope, ground-based, and (longward of 3 μm) Spitzer observations of a galaxy at redshift $z=5.8$. The break at an observed wavelength of ~ 3 μm in the model SED fit to the data lies at the position of the Balmer jump, a persistent feature seen in the spectra of nearby galaxies at a wavelength ~ 0.4 μm. The Spitzer observations establish the magnitude of the Balmer jump, which is critically important in determining the mass and age of the stellar population of the galaxy. The power of Spitzer to measure faint objects is demonstrated by the long-duration (12 h) IRS long-low-1 spectrum of a $z=2.69$ Chandra soft x-ray source in the Hubble Ultradeep Field (Fig. 26). Comparison of the spectrum with the spectra of local objects shows that the strength and width of the polycyclic aromatic hydrocarbon (PAH) features in the Chandra source are very similar to those in the local galaxies M52 and UGC 5101.

2. Active galactic nuclei

Besides stars, material falling into supermassive (a billion solar masses) black holes is the second major source of energy in the universe. These sources manifest themselves as active galactic nuclei (AGN), a category that includes quasars, radio galaxies, and a number of other types. These ob-

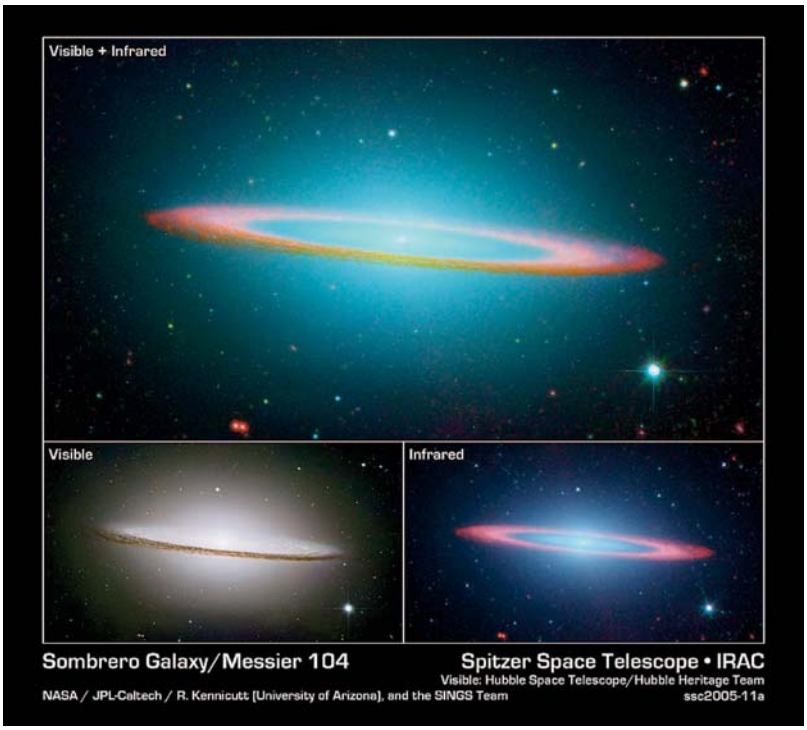

FIG. 42. (Color) Anatomy of the edge-on spiral Galaxy M104 (The Sombrero). Infrared: NASA/JPL-Caltech/R. Kennicutt (University of Arizona), and the SINGS (Ref. 69) legacy team. Visible: Hubble Space Telescope/Hubble Heritage Team.

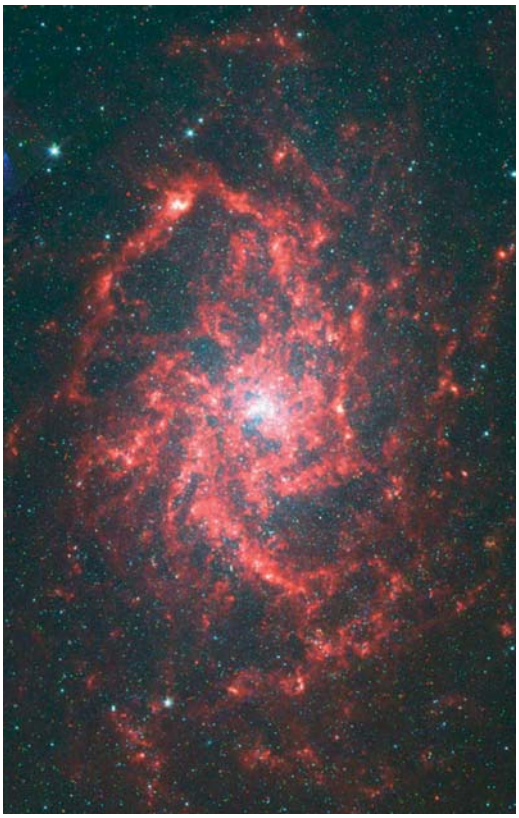

FIG. 43. (Color) Spitzer three-color image of the Sc spiral galaxy M33. Image courtesy of Polomski *et al.* (University of Minnesota) and Fazio *et al.* (SAO).

jects are thought to be intrinsically luminous x-ray sources, and deep x-ray imaging with Chandra and XMM-Newton are the most successful approaches to finding large numbers of them at high redshift. However, summing the outputs of the x-ray discoveries does not fully account for the diffuse x-ray glow of the sky, a glow that for a number of reasons is thought to arise from the totality of AGN outputs. This shortage is believed to be caused by the absorption of some of the x-ray emission by circumnuclear material surrounding the black holes. This absorption occurs preferentially at relatively low x-ray energies (a few keV), and since the imaging x-ray telescopes respond in this energy range, many AGN may have escaped detection.

Spitzer is being used to identify AGN independently of their x-ray properties. One approach is based on the unique spectral energy distributions of AGN in the mid-infrared, where hot dust surrounding the AGN can drown out the emission of stars in normal galaxies.[64–66] A second is to compare radio and infrared properties of galaxies; star forming galaxies have a restricted range of ratios of radio to infrared, significantly lower than the ratio for a subset of radio-bright AGN.[67,68] AGN candidates selected by these means include roughly twice as many objects as can be found with similar infrared and radio characteristics and also detected in the very deepest x-ray surveys.[66,68] Thus, it appears that the AGN "missing" from the x-ray surveys may be in the process of discovery with Spitzer.

3. Nearby normal galaxies

Spitzer's wide wavelength coverage, from 3.6 to 160 μm, samples radiation from a number of galactic constituents. These range from stellar atmospheres to cold dust in quiescent interstellar clouds. This scope, together with Spitzer's fundamental imaging field of view of $5' \times 5'$, well matched to the angular size of even the nearest galaxies, allows Spitzer to provide striking images that provide new insights into the distribution of stars, interstellar matter, and star formation throughout a galaxy. Images such as these, and complementary spectra, are being obtained for some 50 nearby galaxies by the SINGS (Ref. 69) legacy team. This will provide both a marvelous database for studies of nearby galaxies and invaluable ground truth for the interpretation of Spitzer's observations of the integrated light from more distant, spatially unresolved galaxies. Figures 41–43 show the anatomy of the spiral galaxies M81, M104, and M33, respectively. It is evident that star formation dominates the disk emission and that starlight dominates the central bulge.

B. The formation and evolution of stars and planetary systems

1. Star formation in dark clouds

The infrared is ideally suited for the study of star formation, a process that occurs at low temperature and within dense interstellar clouds opaque to visible and ultraviolet radiations.

Figure 44 compares a Spitzer image of the thermal emission from the dark globule IC 1396 with a Hubble Space Telescope (HST) visual image, in which it appears as a black, opaque cloud. The Spitzer image discloses numerous young stellar objects embedded in the cloud and shows the diffuse infrared glow of gas and dust that is only a few hundred degrees above absolute zero.

FIG. 44. (Color) Composite Spitzer infrared array camera image of a dark globule in IC 1396 reveals an embedded cluster of stars forming from the gas and dust. Emissions from 3.6 μm (blue), 4.5 μm (green), 5.6 μm (orange), and 8.0 μm (red) have been combined in a single image to represent different temperature regimes. Stellar objects appear blue and green. The 200–400 K gas and dust glow orange and red. The Hubble Space Telescope visual image (lower left) shows the cold, opaque cloud. Courtesy of NASA/JPL-Caltech/Reach (SSC/Caltech).

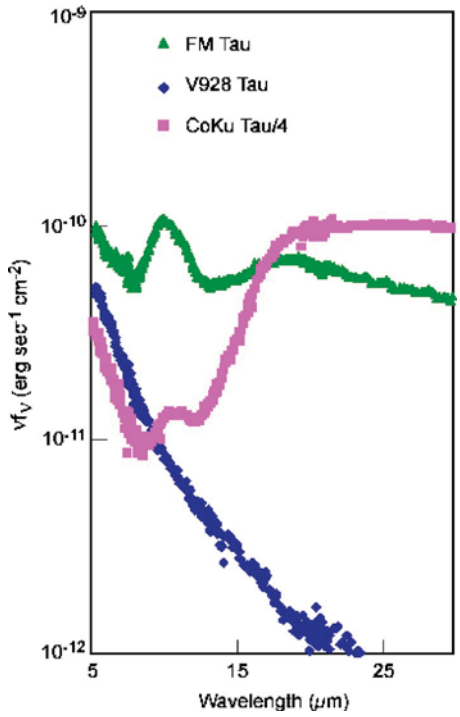

FIG. 45. IRS spectra of three young stellar objects in Taurus. CoKu Tau/4 shows a flux deficit in the 5–15 μm region, indicative of a central clearing in its circumstellar disk in comparison to that of FK Tau. V928 Tau no longer shows evidence for any circumstellar material, indicating complete dissipation of the protoplanetary disk. [Forrest *et al.* (Ref. 84) revised and reproduced by permission of the AAS.]

2. Planetary system formation

General theoretical considerations and conservation of angular momentum predicts that a collapsing protostar will shed a circumstellar disk in its equatorial plane, and we know from recent discoveries that planetary systems form frequently within such disks. Spitzer studies the process of planetary system formation by tracing the dissolution of the circumstellar disks around class II objects. The condensation of dust and gas within these disks gives rise to planets and also contributes to the disappearance of the disks. Spitzer observations of stars and clusters of differing ages suggest that the warm dust lying in the terrestrial planet zone around solar-type stars disappears within a few million years, so that terrestrial planet formation occurs quickly. Some disks, such as that around CoKu Tau 4 (Fig. 45), show an absence of warm dust, providing dramatic evidence for central clearing possibly attributable to planet formation. Figure 46 shows how IRS can identify the building blocks of life and planets in young stellar objects.

After the first million years, most of the gas has escaped from a protoplanetary disk and gas giant planets can no longer form. Terrestrial planets, in comparison, continue to grow and evolve for tens of millions of years, as planetesimals collide and either stick together or blast each other into pieces that are collected eventually into ever larger bodies. An example is the colossal collision of a Mars-sized body with the Earth about 30×10^6 years into the formation of the solar system, an event that led to the formation of the Moon. This phase of evolution can be studied very effectively with Spitzer, through detection of the debris from planetismal collisions that is heated by the central star and glows in the infrared. Figure 47 compares two such nearby systems, both at a distance of about 8 pc (25 light years) and around stars of similar mass and age. The surprising differences apparent in the Spitzer images have been interpreted in terms of a major collision occurring recently (on a geological time scale) in the Vega planetary system.[70]

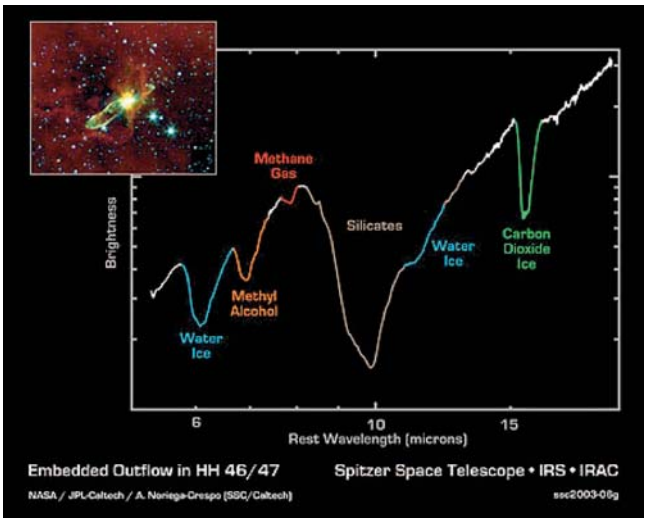

FIG. 46. (Color) IRS spectra show the building blocks of life and plants in an embedded YSO (NASA/JPL-Caltech).

3. Brown dwarfs

Objects less massive than about 8% of the Sun's mass may form by gravitational collapse but do not become dense

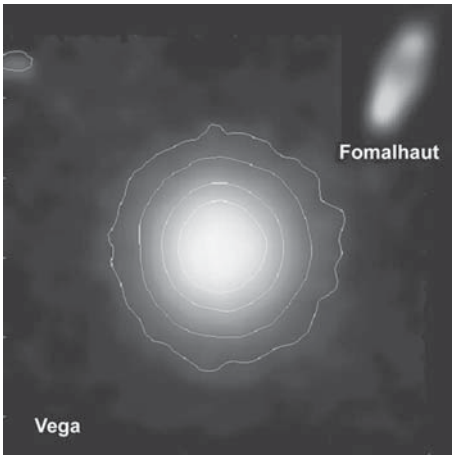

FIG. 47. Images of the debris disks around Fomalhaut (Ref. 80) and Vega (Ref. 70) at 70 μm, reproduced to the same physical scale. Both stars are about 2.5 times the mass of the Sun, at a distance of 8 pc, and about 300×10^6 years old. In neither case is the central star apparent in the image. Fomalhaut is surrounded by a nearly edge-on ring, analogous to the Kuiper belt in the solar system, about 100 AU in radius. The asymmetry in the ring is caused by its being miscentered on the star, probably due to interaction with a massive planet, so the ring segment to the lower left is raised to a higher temperature than the one to the upper right. In contrast, Vega is nearly face on, accounting for the circular symmetry of its debris system. It also appears to have a circumstellar ring of radius 80–100 AU, but the system is dominated by a bright halo that extends to nearly 1000 AU from the star. It is thought that this halo may arise from a collision within the last few million years between planetesimals, resulting in production of many small grains that are now being ejected by photon pressure.

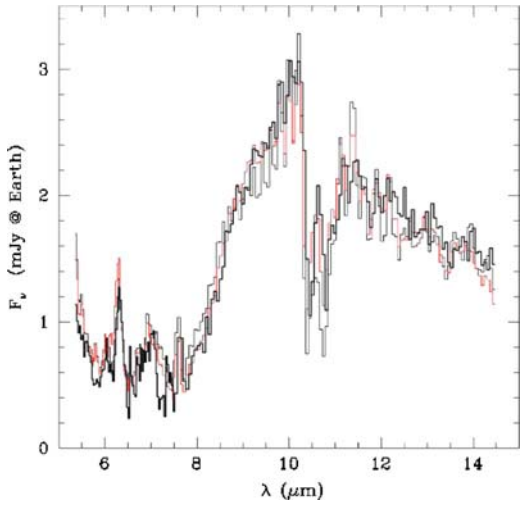

FIG. 48. The measured IRS spectrum of the T8 brown dwarf Gl570D compared with two model spectra. The observed spectrum is indicated by the heavy black line, while the model spectra correspond to models in (thin black line) and out (red line) of atmospheric chemical equilibrium. For a more detailed discussion of the chemical equilibrium implications of the IRS spectrum of G1570D, see Ref. 71.

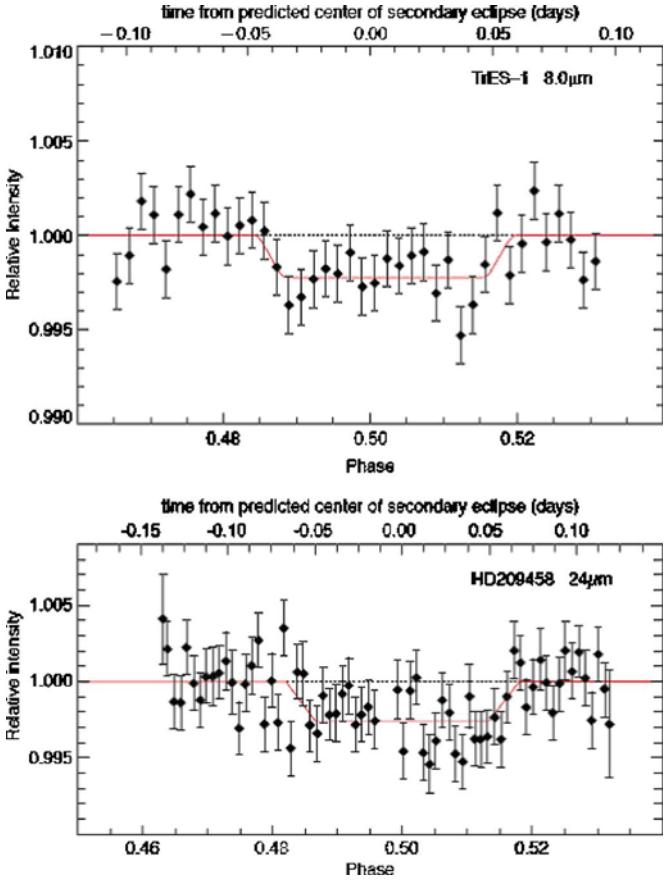

FIG. 49. Top: IRAC detection of the eclipse in the TrES-1 system [Charbonneau *et al.* (Ref. 39)]. Bottom: MIPS detection of the secondary eclipse in the HD209458 system [Deming *et al.* (Ref. 76)].

or hot enough at their centers to sustain nuclear burning. These failed stars are known as substellar objects or brown dwarfs. When they are young, they can be quite bright in the infrared as they radiate the heat generated as they collapsed (at later times, they are cooler and fainter but still detectable by Spitzer). The atmospheres of brown dwarfs can be quite complicated, with a mixture of atomic gases, molecules, and clouds of either silicates or iron condensates. With its unprecedented sensitivity, Spitzer can take mid-infrared spectra of even some of the older field brown dwarfs (Fig. 48), and has demonstrated that the atmospheres of these objects can be very dynamic with out-of-equilibrium chemistry.[71] A significant result from Spitzer's studies of disks and planetary system formation is that young brown dwarfs, even some with masses down to 10 Jupiter masses (~1.5% of the solar mass) or less,[72,73] show circumstellar disks as frequently as do more massive objects; thus isolated brown dwarfs form by collapse processes similar to those that form stars. Additionally, Apai *et al.*[74] found evidence for grain and structure evolution in disks around young brown dwarfs similar to that thought to signal the first steps toward planet formation around young stars. Because brown dwarfs are at least as common in the solar neighborhood as are stars of all other types, this raises the interesting possibility that the nearest extrasolar planets may be orbiting a brown dwarf, that itself may be thought of as a giant planet.

4. Extrasolar planets

The first confirmed extrasolar planet orbiting a solar-type star, in the 51 Pegasi system,[75] was also the first example of a "hot Jupiter" or "roaster" (a planet with a mass comparable to that of Jupiter that orbits within ~0.05 AU of its parent star). The origins of these planets and their orbits remain a puzzle; however, their temperatures (close to 1000 K) and the amount of infrared radiation they produce should make them detectable by Spitzer out to distances of 200 pc. To detect such planets, Charbonneau *et al.*[39] and Deming *et al.*[76] exploited the favorable case where the orbital inclination permits mutual eclipses of the star and the planet. The disappearance of the planet behind the star during the secondary eclipse leads to a small ($\ll 1\%$) drop in the infrared radiation from the star-planet system. As shown in Fig. 49, Deming *et al.* used MIPS to detect the secondary eclipse in the HD209458 system with an amplitude at 24 μm of $0.26 \pm 0.046\%$, while Charbonneau *et al.* used IRAC to detect the eclipse in the TrES-1 system with amplitudes of $0.066 \pm 0.013\%$ at 4.6 μm and $0.225 \pm 0.036\%$ at 8 μm. Such measurements provide unique constraints on the temperature, Bond albedo, and perhaps the composition of the planets, that in turn provide clues to how they formed. We can anticipate further results of this type from Spitzer, both from additional studies of TrES-1 and HD209458 and from exploration of additional transiting planets.

5. The evolution of massive stars

Figures 50 and 51 reveal the spatial and spectral morphologies of the Crab Nebula, a young, expanding remnant left over from a type-II supernova explosion that resulted from the core collapse of a very massive star. Massive stars synthesize all of the elements up to iron in their cores by nuclear fusion, and the rest of the 92 elements are produced by neutron captures in the supernova explosions that end their lives. These violent explosions eject enormous amounts

FIG. 50. (Color) Spitzer composite image of the Crab Nebula as seen by the Spitzer IRAC (blue=3.6 μm, green=8.0 μm) and MIPS (red=24 μm) cameras. The Crab is the expanding remnant of a supernova explosion that was recorded in 1054 AD. Courtesy of Temim, Gehrz, and Temim *et al.* (Ref. 77), University of Minnesota.

of metal-rich gas and dust into star formation regions in the interstellar medium where they are are incorporated into new stellar systems such as the solar system. Thus, remnants of recent supernova explosions contain valuable information about the chemical evolution of the universe and the origin of the materials that are the building blocks of the planets and life itself. Temim *et al.*[77] have obtained Spitzer IRAC and MIPS images (Fig. 50) and IRS spectroscopy of the Crab Nebula (Fig. 51). Their analysis suggests that there is a paucity of small dust grains in the Crab remnant compared to what might be expected based on predictions of the amount of condensible material that a supernova explosion could produce. They suggest that this finding is consistent with theoretical speculation that the shock waves produced by explosion may suppress dust formation or destroy grains after they have formed.

C. Solar system science

Comets have been termed the "Rosetta Stone" of the solar system because the building blocks of life and the planets were frozen into their nuclei 4.6×10^9 years ago during the epoch of planet formation in the primitive solar system. Samples of this primordial material were released when NASA's Deep Impact Probe smashed into the nucleus of comet Tempel on 2005 July 4. The Spitzer IRS spectrum of the ejected material (Fig. 52) showed a strong 10 μm emission feature, demonstrating that the interior of the nucleus is rich in very small silicate dust grains compared to the surface layers. Previous studies of the activity of comet nuclei had suggested that this might be the case.[78]

Figure 53 shows a MIPS image that reveals the faint thermal emission from the sand-and gravel-sized particles that produce November Taurid meteor showers when the Earth crosses the orbit of comet P/Encke.[79] The coma, tail, and antitail emissions from comet Schwassmann-Wachmann 1 are shown in Fig. 54.[85]

IX. DISCUSSION

Planning for Spitzer began more than 30 years prior to its eventual launch. A strong thread of technical development and innovation links the decades, and we are fortunate that

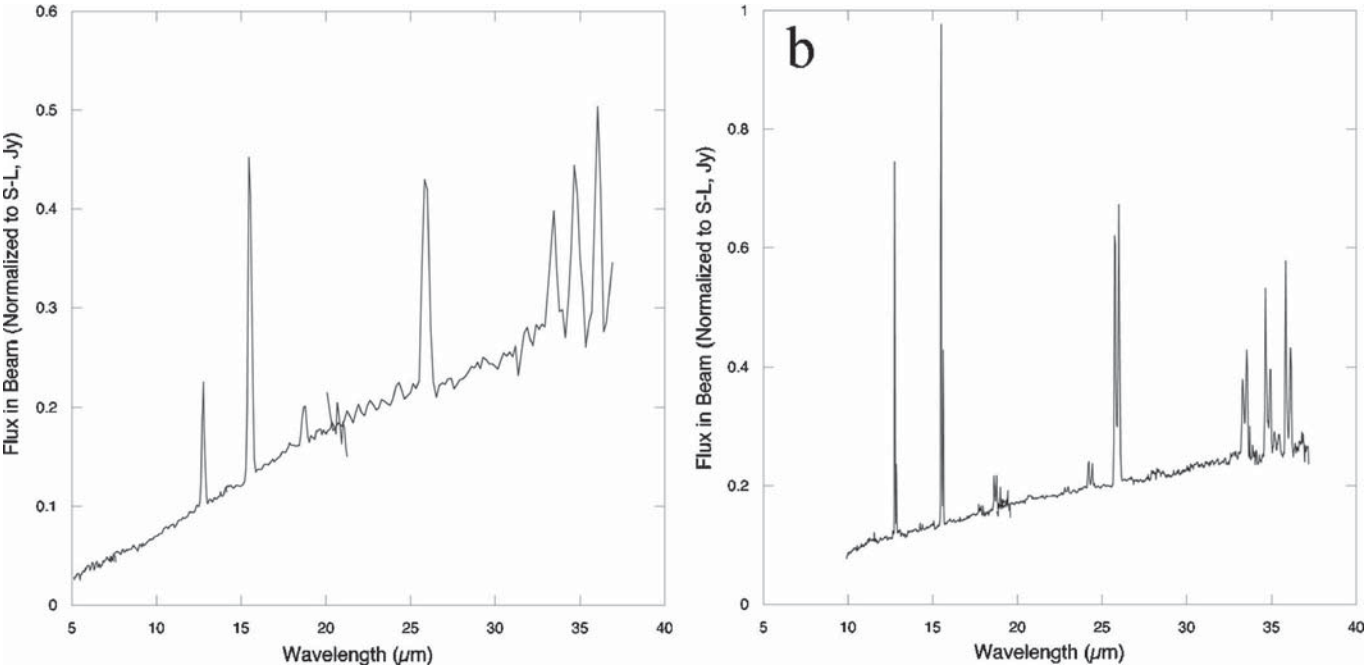

FIG. 51. IRS IRS Lo-RES (a) and Hi-RES (b) spectra of a filament in the Crab Nebula Supernova remnant showing a rich mix of lines from elements ejected in the explosion. The strongest are [Ne II]12.8 μm, [Ne III]15.6 μm, [S III]18.7 μm, [Fe III]22.9 μm, [Ne V]24.3 μm, [O IV]25.9 μm, [S III]33.5 μm, [Si II]34.8 μm, [Fe II]35.3 μm, and [Ne III]36.0 μm. The 2400 km s^{-1} line splitting in the Hi-RES spectrum is caused by Doppler shifts due to the expansion of the ejecta. Reproduced courtesy of Temim *et al.* (Ref. 77).

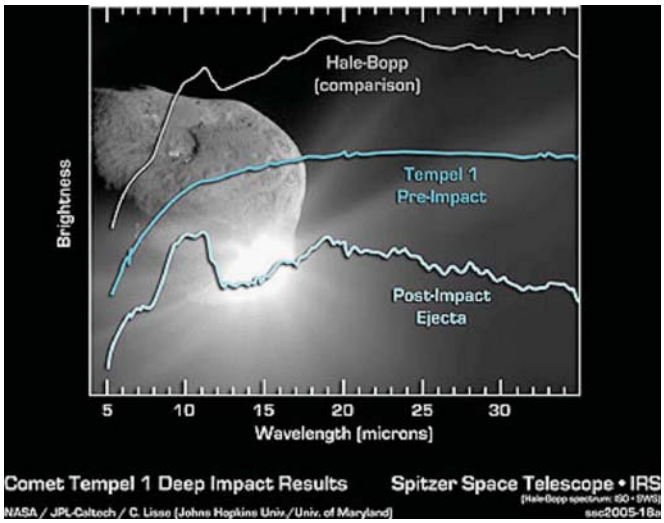

FIG. 52. Spitzer IRS infrared spectrum of the dust ejected during NASA's Deep Impact mission to comet Tempel 1 showing the strong 10 μm emission feature produced by small silicate grains. Previous to this experiment, the strongest cometary 10 μm emission feature (relative to the continuum) had been observed in Comet Hale-Bopp. Courtesy of NASA/JPL-Caltech/Lisse (Johns Hopkins University/University of Maryland).

NASA had the foresight and ability to continue to invest in these areas even as external events prevented the mission itself from gaining traction for many years. Consequently, the Spitzer observatory now operating in Earth-trailing orbit incorporates key new technologies in optics, detectors, cryogenic and thermal design, and operations that are both central to Spitzer's success and essential components of the planning for future infrared missions. Thus Spitzer is a great success not only scientifically, but also technically, because the innovative design, development, and test and integration approaches demonstrated by our robust and efficient observatory will be carried on in the future. The technical and scientific triumphs of Spitzer set the stage for follow-on infrared missions being developed or planned by NASA, ESA, and the Japanese Space Agency. The most ambitious of these, the Japanese SPICA mission and the NASA/ESA/CSA James Webb Space Telescope, will launch in the next decade. Between now and then we will see the initial results from satellite and airborne telescopes probing the infrared band with a range of pointed- and survey-mode observations. Together, these missions promise to provide the astronomical community with continuous access to the infrared spectral band to extend the remarkable exploration begun by Spitzer, just as Spitzer itself builds on the predecessor IRAS and ISO missions.

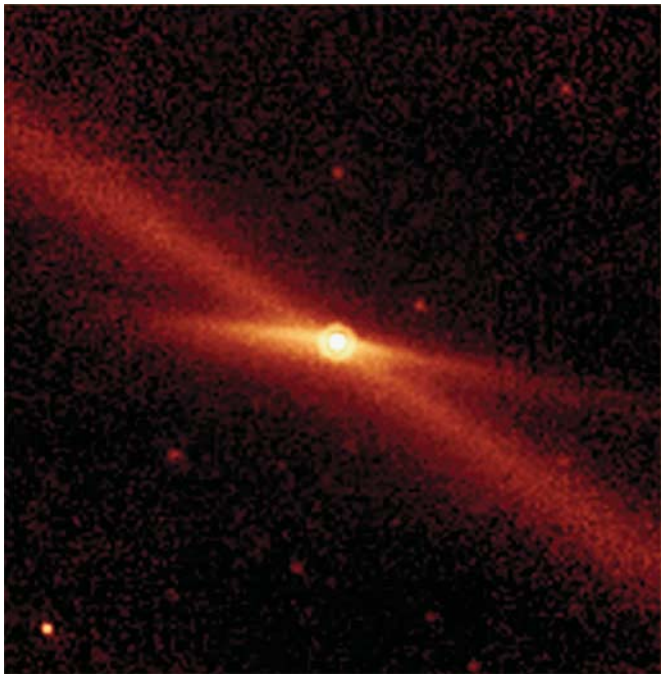

FIG. 53. Comet Encke and the debris trail (long diagonal line) that follows the path of Encke's orbit. Twin jets of fine dust particles, activated by insolation, spread horizontally from the comet at an angle to the orbit. The debris trail, made of larger sand- and gravellike debris that spread around the orbit due to Poynting-Robertson drag, produces the October Taurid meteor shower as the Earth crosses Encke's orbit. Image courtesy of NASA/JPL-Caltech/Kelley (University of Minnesota), and Reach and Kelley (2006) (Ref. 79).

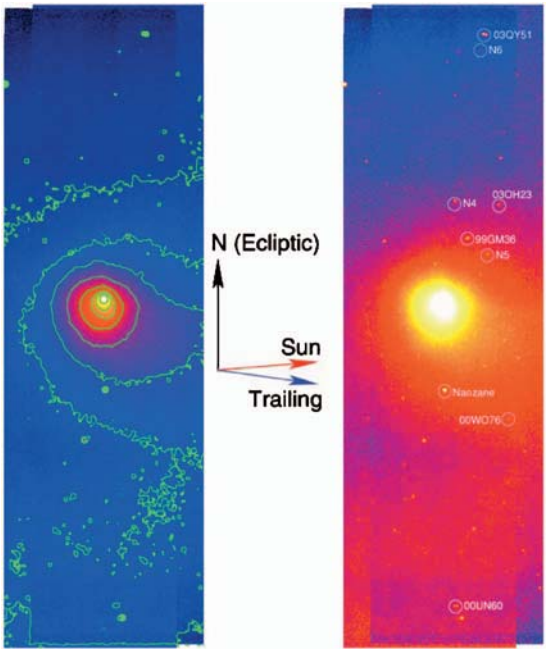

FIG. 54. (Color) MIPS 24 μm image of comet 29/P Schwassmann-Wachmann 1 showing the structure of the coma and debris trail. Nine asteroids are visible in the image, three of them newly discovered. Image reproduced by permission of Stansberry *et al.* (Ref. 85).

GLOSSARY OF ACRYNOMS

ac	=	alternating current
ADM	=	aperture door mechanism
AGN	=	active galactic nuclei
AOR	=	astronomical observation request
AU	=	astronomical Unit
BATC	=	Ball Aerospace Technologies Corporation
BCD	=	basic calibrated data
BIB	=	blocked impurity band
BICP	=	base line instrument campaign plan
BRUTUS	=	the name of a large cryogenic thermal vacuum test chamber at BATC
CDH	=	control and data handling
CA	=	cryogenic assembly

C2D = From molecular cores to planet-forming disks
CMOS = complementary metal oxide semiconductor
CSA = Canadian Space Agency
CTA = cryogenic telescope assembly
CT = cryogenic telescope
dc = direct current
DDT = director's discretionary time
DSN = deep space network
EDT = eastern daylight time
ESA = European Space Agency
FEPS = the formation and evolution of planetary systems
FITS = flexible image transport system
FWHM = full width at half maximum
GLIMPSE = galactic legacy infrared midplane survey extraordinaire
GO = General Observer
GOODS = Great Observatories Origins deep survey
GTO = guaranteed time observer
HEO = high Earth orbit
HIP = hot isostatically pressed
IOC = in-orbit checkout
IPT = integrated product team
IRAC = infrared array camera
IRAS = infrared astronomical satellite
IRS = infrared spectrograph
ISO = infrared space observatory
JPL = Jet Propulsion Laboratory
LEO = low Earth orbit
LMMS = Lockheed Martin Missiles and Space
MIC = multiple instrument chamber
MIPS = multiband imaging photometer for SIRTF
MLI = multilayer insulation
NASA = National Aeronautics and Space Administration
OPZ = operational pointing zone
OS = outer shell
OSCAR = optical System cryogenic alignment reference
PCS = pointing control system
PAH = polycyclic aromatic hydrocarbon
PCRS = pointing calibration and reference sensor
PI = principle investigator
p-i-n = *p* type, Intrinsic, *n* type
RAD = rapid application development
RCS = reaction control system
REOSC = the French firm that fabricated OSCAR
rf = radio frequency
rms = root mean square
ROC = reserved observations catalog
SAO = Smithsonian Astrophysical Observatory
SCB = spacecraft bus
SED = spectral energy distribution
SI = science instrument
SINGS = the Spitzer infrared nearby galaxies survey
SIRTF = Space Infrared Telescope Facility
SODB = Spitzer Observational Database
SOM = Spitzer Observer's Manual
SPOT = Spitzer planning observations tool
SSC = Spitzer Science Center
SV = science verification
SVG = Silicon Valley Group
SWG = Science Working Group
SWIRE = the Spitzer wide-area infrared extragalactic survey
SWIFT = A NASA Gamma Ray Burst Observatory
SWIR = short wavelength infrared
ToO = target of opportunity
UTC = coordinated universal time
WEA = warm electronic assembly

ACKNOWLEDGMENTS

Literally hundreds of people made important contributions to the design and success of the Spitzer mission. A complete list of the participants is presented in Ref. 2. The authors thank D. Dale and J. D. Smith for providing the spectra of M81 for the cover figure (Fig. 41) on behalf of the SINGS legacy team. Portions of the research described here were carried out at the Jet Propulsion Laboratory (JPL), California Institute of Technology (Caltech) under contract with the National Aeronautics and Space Administration (NASA). The Spitzer Space Telescope is operated by JPL under NASA Contract No. 1407. R.D.G. was supported by NASA through Contract Nos. 1256406 and 1215746 issued by JPL/Caltech to the University of Minnesota. Reference herein to any specific commercial product, process, or service by trade name, trademark, or manufacturer, or otherwise does not constitute or imply its endorsement by the United States Government or JPL/Caltech.

[1] Formerly Space Infrared Telescope Facility (SIRTF).
[2] M. W. Werner *et al.*, Astrophys. J., Suppl. Ser. **154**, 1 (2004).
[3] M. G. Hauser and E. Dwek, Annu. Rev. Astron. Astrophys. **39**, 249 (2001).
[4] J. N. Bahcall *et al.*, *The Decade of Discovery in Astronomy and Astrophysics* (National Academy, Washington, DC, 1991).
[5] M. W. Werner, ASP Conf. Ser. (in press).
[6] G. H. Rieke, *The Last of the Great Observatories: Spitzer and the Era of Faster, Better, Cheaper at NASA* (The University of Arizona Press, Tucson, AZ, 2006).
[7] P. T. Finley, R. A. Hopkins, and R. B. Schweickart, Proc. SPIE **5487**, 26 (2004).
[8] A. K. Mainzer, E. T. Young, T. P. Greene, N. Acu, T. H. Jamieson, H. Mora, S. Sarfati, and R. W. van Bezooijen, Proc. SPIE **3356**, 1095 (1998).
[9] http://www.spitzer.caltech.edu/Media/releases/ssc2004-03/index.shtml
[10] http://www.spitzer.caltech.edu/Media/releases/ssc2003-05/release.shtml
[11] A. K. Mainzer and E. T. Young, Proc. SPIE **5487**, 93 (2004).
[12] E. Hog *et al.*, Astron. Astrophys. **355**, 27 (2000).
[13] R. van Bezooijen, L. Degen, and H. Nichandros, Proc. SPIE **5487**, 253 (2004).
[14] K. Strehl, Z. Instrumentenkd. **22**, 213 (1902).
[15] M. Born and E. Wolf, *Principles of Optics*, 2nd ed. (Pergamon, Oxford, 1964), p. 441.
[16] R. D. Gehrz *et al.*, Proc. SPIE **5487**, 166 (2004).
[17] W. F. Hoffmann, J. L. Hora, J. E. Mentzell, C. T. Marx, and P. R. Eisenhardt, Proc. SPIE **4850**, 428 (2003).
[18] R. D. Gehrz and E. A. Romana, Proc. SPIE **4850**, 62 (2003).
[19] G. G. Fazio *et al.*, Astrophys. J., Suppl. Ser. **154**, 10 (2004).
[20] G. H. Rieke *et al.*, Astrophys. J., Suppl. Ser. **154**, 25 (2004).
[21] J. R. Houck *et al.*, Astrophys. J., Suppl. Ser. **154**, 18 (2004).
[22] http://ssc.spitzer.caltech.edu/propkit/spot/
[23] E. L. Wright, P. Eisenhardt, and G. Fazio, Bull. Am. Astron. Soc. **26**, 893 (1994).
[24] C. Simpson and P. Eisenhardt, Publ. Astron. Soc. Pac. **111**, 691 (1999).
[25] G. G. Fazio *et al.*, Proc. SPIE **3354**, 1024 (1998).
[26] A. D. Estrada *et al.*, Proc. SPIE **3354**, 99 (1998).

[27] J. Wu, W. J. Forrest, J. L. Pipher, N. Lum, and A. Hoffman, Rev. Sci. Instrum. **68**, 3566 (1997).
[28] J. L. Pipher *et al.*, Proc. SPIE **4131**, 7 (2000).
[29] R. G. Benson, W. J. Forrest, J. L. Pipher, W. J. Glaccum, and S. L. Solomon, Proc. SPIE **4131**, 171 (2000).
[30] R. E. McMurray *et al.*, Proc. SPIE **4131**, 62 (2000).
[31] http://ssc.spitzer.caltech.edu/documents/som/irac60.pdf
[32] A. M. Fowler and I. Gatley, Astrophys. J. Lett. **353**, L33 (1990).
[33] http://ssc.spitzer.caltech.edu/irac/dh/iracdatahandbook3.0.pdf
[34] S. T. Megeath, M. Cohen, J. Stauffer, J. L. Hora, G. Fazio, P. Berlind, and M. Calkins, in *The Calibration Legacy of the ISO Mission*, edited by L. Metcalfe, A. Salama, S. B. Peschke, and M. F. Kessler (ESA Publications, Noordwijk, 2003), p. 165.
[35] M. Cohen, S. T. Megeath, P. L. Hammersley, F. Martin-Luis, and J. Stauffer, Astron. J. **125**, 2645 (2003).
[36] W. T. Reach *et al.*, Publ. Astron. Soc. Pac. **117**, 978 (2005).
[37] G. G. Fazio *et al.*, Astrophys. J., Suppl. Ser. **154**, 39 (2004).
[38] H. Yan *et al.*, Astrophys. J. **634**, 109 (2005).
[39] D. Charbonneau *et al.*, Astrophys. J. **626**, 523 (2005).
[40] http://ssc.spitzer.caltech.edu/documents/SOM/start50.pdf
[41] R. Schnurr, C. L. Thompson, J. T. Davis, J. W. Beeman, J. Cadien, E. T. Young, E. Haller, and G. H. Rieke, Proc. SPIE **3354**, 322 (1998).
[42] E. T. Young *et al.*, Proc. SPIE **3354**, 57 (1998).
[43] E. T. Young *et al.*, Proc. SPIE **5883**, 156 (2005).
[44] G. B. Heim, Proc. SPIE **3356**, 985 (1998).
[45] J. W. G. Aalders, K. J. Wildeman, G. R. Ploeger, and Z. N. van der Meij, Cryogenics **29**, 550 (1989).
[46] R. M. Warden and G. B. Heim, *Proceedings of the 32nd Aerospace Mechanisms Symposium*, edited by S. W. Walker and E. A. Boesiger, NASA CP-1998–207191 (Government Printing Office, Washington, 1998).
[47] C. H. Downey, J. R. Houck, M. J. Kubitschek, and R. W. Tarde, Cryogenics **31**, 1030 (1991).
[48] K. D. Gordon *et al.*, Proc. SPIE **5487**, 177 (2004).
[49] K. D. Gordon *et al.*, Publ. Astron. Soc. Pac. **117**, 503 (2005).
[50] G. H. Rieke *et al.*, Proc. SPIE **5487**, 50 (2004).
[51] C. R. Lawrence and P. T. Finley, Proc. SPIE **5487**, 124 (2004).
[52] P. T. Finley, R. L. Oonk, and R. B. Schweickart, Proc. SPIE **4850**, 72 (2003).
[53] http://www.iso.vilspa.esa.es/
[54] H. Dole *et al.*, Astrophys. J., Suppl. Ser. **154**, 93 (2004).
[55] H. Dole *et al.*, Astron. Astrophys. **451**, 417 (2006).
[56] D. C. Wells, E. W. Greisen, and R. H. Harten, Astron. Astrophys., Suppl. Ser. **44**, 363 (1981).
[57] http://www.ssc.spitzer.caltech.edu
[58] First Observations with the Spitzer Space Telescope, Astrophys. J., Suppl. Ser. **154** (2004).
[59] M. Werner, G. Fazio, G. Rieke, T. Roellig, and D. M. Watson, Annu. Rev. Astron. Astrophys. 44, 269–321 (2006).
[60] E. Egami *et al.*, Astrophys. J. **618**, L5 (2005).
[61] http://ssc.spitzer.caltech.edu/mtgs/newviews/
[62] http://ssc.spitzer.caltech.edu/mtgs/irevolve/
[63] http://www.spitzer.caltech.edu/Media/index.shtml
[64] M. Lacy *et al.*, Astrophys. J., Suppl. Ser. **154**, 166 (2004).
[65] D. Stern *et al.*, Astrophys. J. **631**, 163 (2005).
[66] A. Alonso-Herrero *et al.*, Astrophys. J. **640**, 167 (2006).
[67] A. Martinez-Sansigre, S. Rawlings, M. Lacy, D. Fadda, F. R. Marleau, C. Simpson, C. J. Willott, and M. J. Jarvis, Nature (London) **436**, 666 (2005).
[68] J. L. Donley, G. H. Rieke, J. R. Rigby, and P. G. Perez-Gonzalez, Astrophys. J. **634**, 169 (2005).
[69] R. Kennicutt *et al.*, Publ. Astron. Soc. Pac. **115**, 928 (2003).
[70] K. Y. L. Su, Astrophys. J. **628**, 487 (2005).
[71] D. Saumon, M. S. Marley, M. C. Cushing, S. K. Leggett, T. L. Roellig, K. Lodders, and R. S. Freedman, Astrophys. J. **647**, 552 (2006).
[72] K. L. Luhman, L. Adame, P. D'Alessio, N. Calvet, L. Hartmann, S. T. Megeath, and G. G. Fazio, Astrophys. J. Lett. **635**, L93 (2005).
[73] K. L. Luhman, P. D'Alessio, N. Calvet, L. L. Allen, L. Hartmann, S. T. Megeath, P. C. Myers, and G. G. Fazio, Astrophys. J. Lett. **620**, L51 (2005).
[74] D. Apai, I. Pascucci, J. Bouwman, A. Natta, T. Henning, and C. P. Dullemond, Science **310**, 834 (2005).
[75] M. Mayor and D. Queloz, Nature (London) **378**, 355 (1995).
[76] D. Deming, S. Seager, L. J. Richardson, and J. Harrington, Nature (London) **434**, 740 (2005).
[77] T. Temim *et al.*, Astrophys. J. **132**, 161 (2006).
[78] R. D. Gehrz, C. H. Johnson, S. D. Magnuson, E. P. Ney, Icarus **113**, 129 (1995).
[79] M. S. Kelley *et al.*, Astrophys. J. **651**, 1256 (2006).
[80] K. R. Stapelfeldt *et al.*, Astrophys. J. **154**, 458 (2004).
[81] http://ssc.spitzer.caltech.edu/documents/SOM/irs60.pdf
[82] H. Teplitz *et al.*, private communication (2007).
[83] L. P. Eyles, A. J. Bunker, E. R. Stanway, M. Lacy, R. S. Ellis, and M. Doherty, Mon. Not. R. Astron. Soc. **364**, 443 (2005).
[84] W. J. Forrest *et al.*, Astrophys. J., Suppl. Ser. **154**, 443 (2004).
[85] J. A. Stansberry *et al.*, Astrophys. J., Suppl. Ser. **154**, 463 (2004).